

Hannes Allmaier

**Electron correlations in half-metallic
ferromagnets and other transition metal
compounds**

DISSERTATION

zur Erlangung des akademischen Grades
Doktor/in der technischen Wissenschaften /
Doktor/in der Naturwissenschaften

Doktoratsstudium der technischen Wissenschaften
Technische Physik /
Doktoratsstudium der Naturwissenschaften
Technische Physik



Technische Universität Graz

Betreuer:
Univ.-Prof. Dr.rer.nat. Enrico Arrigoni
Institut für theoretische Physik - Computational Physics

Graz, Feber 2010

Deutsche Fassung:
Beschluss der Curricula-Kommission für Bachelor-, Master- und Diplomstudien vom 10.11.2008
Genehmigung des Senates am 1.12.2008

EIDESSTATTLICHE ERKLÄRUNG

Ich erkläre an Eides statt, dass ich die vorliegende Arbeit selbstständig verfasst, andere als die angegebenen Quellen/Hilfsmittel nicht benutzt, und die den benutzten Quellen wörtlich und inhaltlich entnommene Stellen als solche kenntlich gemacht habe.

Graz, am

.....
(Unterschrift)

Englische Fassung:

STATUTORY DECLARATION

I declare that I have authored this thesis independently, that I have not used other than the declared sources / resources, and that I have explicitly marked all material which has been quoted either literally or by content from the used sources.

.....
date

.....
(signature)

Abstract

It is the aim of this thesis to investigate electron correlation effects present in materials that consist of transition-metals. In such systems localized electrons dominate the physics around the Fermi-energy. These localized electrons experience strong correlations due to the fact that they are located in partially filled d -shells that do not allow efficient screening of the Coulomb-repulsion.

To study these correlated systems, we employ the newly developed LDA+VCA approach; this new method is a combination of the NMTO-technique, an ab-initio method used to derive model parameters, with a powerful method for strongly correlated electrons, namely the Variational Cluster Approach (VCA). This combined approach employs an extended Hubbard-model and uses its single-particle parameters to describe the real-world compounds of interest; to calculate these from first principles a density functional technique is utilized. The crucial advantage of this method is that the solver, the Variational Cluster Approach, allows to treat short ranged (non-local) correlations exactly by using exact diagonalization, while keeping long-ranged correlations on a mean-field level.

Within this thesis, the LDA+VCA approach is applied to a variety of systems. Among others, we present work on a very interesting material, namely TiN, that is close to a Mott-transition; from our results we explain the presence of its pseudo gap found in experiment. Further, special emphasis is given to half-metallic ferromagnets. These are materials which have a peculiar band-structure: they are conductors for one spin-direction and insulators (or semiconductors) for the other spin direction. These materials lie at heart of the recently developing new branch of electronics where not only charge, but also spin is manipulated: spintronics. A number of important materials predicted to have this property are studied in detail in this work. Notably, our results show for these materials the presence of so-called non-quasiparticle states that appear above the Fermi-energy and help to explain spin depolarization that is found for many materials in experiment.

As half-metallic ferromagnets are known to be sensitive to surfaces and interfaces, we present also work on interfaces in multilayered heterostructures. As the LDA+VCA approach is due to required numerical effort not optimally suited for materials with large unit cells, another state-of-the-art method for strongly correlated systems is used, namely the LDA+DMFT method. While this method allows to study large systems, this advantage comes at the expense of neglecting non-local correlations.

Summarizing, the outline of this thesis is as follows: in chapter 1 a short introduction into transition-metals in general and into spintronics in particular is given. Chapter 2 introduces the LDA+VCA approach in detail. In chapter 3 the work carried out in the framework of this PhD-thesis using this and other approaches is presented. Chapter 4 summarizes the results of this thesis.

Kurzfassung

Es ist der Zweck dieser Doktorarbeit, elektronische Korrelationen in Festkörpern zu untersuchen. Konkret werden Festkörper betrachtet, die u.a. aus Übergangsmetallen aufgebaut sind. Bei solchen Materialien werden die Eigenschaften der Bandstruktur nahe der Fermi-Kante von Elektronen dominiert, die sich in nur teilweise gefüllten d -Orbitalen befinden. Solche d -Elektronen lassen sich nicht vollständig als Elektronengas beschreiben, da ihre Wellenfunktionen nur wenig überlappen und die Elektronen daher relativ stark lokalisiert sind. Dadurch kann die wechselseitige Coulomb-Abstoßung der Elektronen nur schwach abgeschirmt werden und die Grösse dieser Wechselwirkung wird vergleichbar mit der kinetischen Energie der Elektronen.

Um solche stark korrelierten Systeme zu beschreiben, verwenden wir eine neue Methode, die LDA+VCA Näherung. Die LDA+VCA Methode ist eine Kombination der NMTO-Technik - eine ab-initio Methode mittels derer Modell-Parameter errechnet werden - mit einer leistungsfähigen Näherung für stark korrelierte Systeme, der Variationellen Cluster Methode (variational cluster approach, VCA). In der LDA+VCA wird ein erweitertes Hubbard-Modell verwendet, dessen Einteilchenoperatoren, die zur Beschreibung reeller Materialien verwendet werden, mittels Dichtefunktionaltheorie ab-initio berechnet werden. Dieses Hubbard-Modell wird dann mit Hilfe der VCA-Näherung gelöst. Der besondere Vorteil der VCA ist es kurzreichweitige (nicht lokale) Wechselwirkungen exakt zu behandeln, und dabei langreichweitige Wechselwirkungen auf Molekularfeld (mean field) Niveau zu beschreiben.

In dieser Dissertation wird diese Methode auf eine Reihe von sehr unterschiedlichen Materialien angewandt; unter anderem präsentieren wir Ergebnisse für TiN, ein Material, das sich nahe einem Mott Metall-Isolator Übergang befindet und erklären anhand der Ergebnisse, warum dieses Material experimentell einen Pseudogap in der Zustandsdichte aufweist.

Der weitere Schwerpunkt dieser Arbeit liegt bei halbmetallischen Ferromagneten. Diese Bezeichnung umfasst eine Klasse von Materialien, die eine Besonderheit in ihrer Bandstruktur aufweisen: sie zeigen metallisches Verhalten für Elektronen einer Spin-Richtung und isolierendes Verhalten für die andere Spin-Richtung. Diese speziellen Materialien bilden einen Grundstein für einen neuen Zweig der Elektronik, in dem nicht nur die Ladung, sondern auch der Spin der Ladungsträger manipuliert wird: Spintronik. Ergebnisse für eine Zahl von wichtigen Materialien dieser Klasse werden präsentiert. Im Besonderen zeigen unsere Ergebnisse das Auftreten so genannter Nicht-Quasiteilchen Zustände, die nahe der Fermi-Energie auftreten und damit bedeutend die Spin-Polarisierung dieser Materialien reduzieren.

Nachdem die Eigenschaften halbmetallischer Ferromagnete generell empfindlich auf Oberflächen und Grenzflächen reagieren, werden in der Folge auch Ergebnisse zu Grenzflächen in geschichteten Heterostrukturen präsentiert. Wegen der damit verbundenen großen Elementarzelle ist die LDA+VCA Methode aufgrund des benötigten numerischen Aufwand dafür nicht optimal geeignet und eine andere, ebenfalls sehr

leistungsfähige Methode wird angewandt, die so-genannte LDA+DMFT Methode. Mit dieser Methodes ist es allerdings nicht möglich, nicht-lokale Wechselwirkungen zu untersuchen.

Kurz zusammengefasst, diese Dissertation ist folgend gegliedert: Kapitel 1 gibt eine kurze Einführung zu Übergangsmetallen im Allgemeinen und Spintronik im Speziellen. Kapitel 2 gibt einen Überblick über die LDA+VCA Methode. Im Kapitel 3 werden Ergebnisse zu verschiedenen Materialien, die mit dieser und anderen Methoden erhalten wurden, präsentiert. Eine Zusammenfassung der Ergebnisse in Kapitel 4 schließt diese Arbeit ab.



Contents

	Page
1 Introduction	17
1.1 Spintronics	18
1.2 Reasons for the necessity to go beyond the LDA	19
1.2.1 Methods for strongly correlated systems	20
2 The LDA+VCA-approach to correlated systems	21
2.1 The Hubbard-model	22
2.2 Ab-initio construction of the single particle part of the Hamiltonian	24
2.2.1 The N th order muffin-tin-orbitals scheme (NMTO)	25
2.3 The Coulomb-interaction part of the Hamiltonian	27
2.3.1 Derivation	27
2.3.2 Interaction-part of the Hamiltonian	30
2.3.3 Double counting correction (DCC)	34
2.4 Variational Cluster Approach	37
2.4.1 Cluster Perturbation Theory	38
2.4.2 Self-energy functional approach	39
3 Correlation effects in real world materials	43
3.1 Half-metallicity in CrO_2	45
3.1.1 Introduction	45
3.1.2 Electronic structure	45
3.1.3 Model and realistic parameters for the Coulomb interaction	47
3.1.4 Results - Density of states	48
3.1.5 Comparison to other theoretical results and to experimental data	50
3.1.6 Conclusion	55
3.2 The prototype half-metallic ferromagnet: NiMnSb	56
3.2.1 Introduction	56
3.2.2 Electronic structure calculations for NiMnSb	57
3.2.3 Ab-initio construction of the model Hamiltonian	58
3.2.4 Results - Density of states	59
3.2.5 Spectral properties	63
3.2.6 Local and non-local self-energies	64
3.2.7 Low-energy spin polarization and comparison with experiments	69

3.2.8	Summary	71
3.3	Half-metallicity at interfaces: (CrAs)/(GaAs)-superlattices	73
3.3.1	Introduction	73
3.3.2	Electronic structure of CrAs	73
3.3.3	Geometry of multilayers	74
3.3.4	Method - the LDA+DMFT scheme	77
3.3.5	Results	78
3.3.6	Summary	89
3.4	Almost a Mott-Hubbard insulator - TiN	91
3.4.1	Introduction	91
3.4.2	Electronic structure calculations for TiN	92
3.4.3	Model and realistic parameters for the Coulomb interaction	94
3.4.4	Results - Density of states	97
3.4.5	Spectral properties	103
3.4.6	Self-energy	103
3.4.7	Effective mass	104
3.4.8	Summary	106
4	Summary	109
4.1	Outlook	111
A	Acknowledgment	113
B	List of publications	115
C	The Löwdin-downfolding technique	117
D	Finite size effects	119
E	NiMnSb-results for Mn-<i>d</i> basis	123
E.1	Ab-initio Hamiltonian	123
E.2	Results	125
E.3	Conclusion	128
F	Different double counting schemes for NiMnSb - fully localized limit-DCC	131
	Bibliography	133

List of Figures

Figure	Page
1.1 MRAM memory uses the electron spin to store information.	17
1.2 Principle of a spin field-effect transistor.	18
1.3 Periodic table of elements; the transition metals form the block shown in red; as the main quantum number increases from top to bottom, the 3 <i>d</i> -elements form the first row (high-lightened in green), picture courtesy of www.webelements.com	19
2.1 The two basic processes in the Hubbard-model: the arrows denote the hopping of the electron (shown as dot) between lattice sites (shown as center of the potential well), the red wiggle the scattering due to Coulomb-interaction. Picture courtesy of K. Held [1]	22
2.2 Plot of the Cr- <i>t</i> _{2<i>g</i>} bands of CrO ₂ (see also chapter 3.1) obtained from downfolding within NMTO in comparison to the full band structure obtained from LDA [2]. <i>E</i> _{<i>i</i>} (with <i>i</i> = 1, 2, 3) denote the used energy expansion points (values in eV).	26
2.3 Scheme of the Coulomb-interactions present in the Hamiltonian schematically shown for the <i>t</i> _{2<i>g</i>} -orbitals; interaction between two electrons of different spin in the same orbital is denoted by $U = U_{iiii}$, the interaction of electrons with different spins between different orbitals is denoted as $U' = U_{ijij}$, whereas Hund's rule leads to a reduced interaction $U' - J$ of electrons with parallel spins in different orbitals. . .	31
2.4 Additional interaction processes present in the Hamiltonian schematically shown for the <i>t</i> _{2<i>g</i>} -orbitals; on the left a pair-flip is depicted and on the right a spin-flip process. Empty and filled arrows denote the two electrons before and after the flip-process, respectively. For the <i>t</i> _{2<i>g</i>} -orbitals the coefficient of these processes, the Hund's rule coupling constant $J = J_{ijij}$, is independent of the indices of the involved orbitals. 31	31
2.5 Illustration of the real-space distribution of the Mn- <i>d</i> -orbitals in NiMnSb; blue and red denote different phases.	32

2.6	The lattice in this two dimensional example is divided into clusters (denoted as squares); the individual clusters are addressed by vectors \mathbf{R} and \mathbf{R}' . As generally the cluster consists of more than one lattice site (shown as black dots), additional indices are used to denote sites and orbitals within the cluster.	38
3.1	Rutile structure of CrO_2 : Cr1 (green) and Cr2 (orange) denote nonequivalent Cr-atoms (see text). Each Cr-atom is octahedrally coordinated by oxygen atoms (purple). x_i, y_i, z_i denote the local coordinate system used within NMTO.	46
3.2	Real space distribution of the $\text{Cr}(t_{2g})$ Wannier-orbitals: Cr1 is shown in green, Cr2 in orange, oxygen in purple. The upper panel shows the orbitals for Cr1, the lower for Cr2.	47
3.3	The reference system (atoms connected by dashed lines) used in the variational calculation; red and blue denote the unequal Cr-atoms Cr1 and Cr2, respectively. The solid line shows the tetragonal unit cell.	49
3.4	$\text{Cr}(t_{2g})$ orbital-resolved density of states in the ferromagnetic state, calculated within the LDA+VCA approach for $U=3\text{eV}$, and $J=0.9\text{eV}$, using the eight site cluster shown in Fig. 3.3.	50
3.5	Density of states calculated for CrO_2 using LSDA+U for $U=3\text{eV}$, and $J=0.9\text{eV}$. Total DOS is shown as black line, blue denotes $\text{Cr}(d)$ states and in addition O- p states are shown in red.	51
3.6	DOS for CrO_2 obtained from LSDA (blue line) and from LDA+DMFT for $T = 100\text{K}$ (red line) and for $T = 200\text{K}$ (green line). The LSDA-result is considered the zero temperature limit for the LDA+DMFT calculations [P1]. The inset shows in detail the region close to Fermi-energy.	52
3.7	Comparison of the results obtained from LDA+VCA (solid black line) with ultraviolet photoemission (green line, decorated with circles) and data from O(1s) x-ray absorption measurements performed on the conduction band of CrO_2 (blue line, decorated with stars). The inset shows non-spin polarized data from Bremsstrahlung isochromat spectroscopy (red line, decorated with diamonds) in comparison to the results from LDA+VCA (black, solid line). For the inset, the LDA+VCA density of states of both spin orientations is added to yield non-spin polarized results.	53

-
- 3.8 Energy dependence of the spin polarization $P(E)$, as defined in Eq. 3.1, found in x-ray absorption experiments (shown as red decorated, solid line, concerning exact position of the Fermi-energy see also text) in comparison to results from different theoretical calculations: LSDA (black), LDA+DMFT (green), LDA+VCA (blue) . A Gaussian broadening of 0.4 eV (corresponding to the experimental resolution) has been added to the theoretical results. 54
- 3.9 The conventional unit cell for the semi-Heusler NiMnSb compound: *Sb* (large, blue spheres) and *Mn* (medium, green spheres) sit on the same faces of the large cube (shown with thin, solid lines), *Ni* (small, yellow spheres) forms a separate (small) cube drawn using dashed lines. In addition, the atoms belonging to the reference system of the VCA calculation are connected by a thick solid line. *Sb* orbitals are downfolded and, therefore, not included directly in the model calculation. 58
- 3.10 Density of states for NiMnSb obtained from LDA+VCA (red, solid line) for values of the average Coulomb and exchange parameters $U = 2\text{eV}$ and $\bar{J} = 0.65\text{eV}$ for both Mn and Ni atoms. in comparison to results obtained from LSDA (black, dashed line). 60
- 3.11 Density of states for the minority spin channel of NiMnSb using $U = 2$ and $\bar{J} = 0.65\text{eV}$, calculated for different values of the chemical potential. The NQP-states (marked with an arrow) stay pinned at the Fermi-energy independently of the chosen value of the chemical potential. The dashed line shows the reference result for the correct occupation of 14 electrons per unitcell. 61
- 3.12 Majority spin LDA+VCA spectral-function of NiMnSb (black/white density plot) along the conventional path in the BZ. $\mathbf{W}(0.5, 1, 0)$, to $\mathbf{L}(0.5, 0.5, 0.5)$ through $\mathbf{\Gamma}(0, 0, 0)$, $\mathbf{X}(0, 1, 0)$, $\mathbf{K}(0, 0.75, 0.75)$ points and ending at $\mathbf{\Gamma}(0, 0, 0)$. The LSDA bands (red, thin solid lines) are shown for comparison. Parameters are as in Fig. 3.10. 64
- 3.13 Minority-spin LDA+VCA spectral function of NiMnSb (black/white density plot) along the same BZ path as in Fig. 3.12. The LSDA bands (red, thin solid lines) are shown for comparison. Parameters are as in Fig. 3.10. 65
- 3.14 Spin resolved self-energies for *Mn* and *Ni* sites obtained as a sum of orbital-diagonal contribution, at the crossing point $\mathbf{k} = (0.5, 0.7, 0.3)$. The strong *Mn-d* spin splitting is due to the significant difference between majority and minority spin self energies, while the lack of magnetic moment on *Ni* is a consequence of similar spin resolved selfenergies. 66
- 3.15 Imaginary part of the local and orbital-diagonal self-energy (left column). The right column shows the nearest-neighbor parts of $\text{Im}\Sigma$ 68

3.16	Energy-dependent polarization obtained from LSDA and LDA+VCA in comparison with data from spin-polarized photoemission [3] (data used with kind permission from the authors).	69
3.17	The supercells for the $(\text{CrAs})_n/(\text{GaAs})_n$ compounds. <i>Cr</i> (green), <i>As</i> (blue) and <i>Ga</i> (red). On the top left, $n = 1$ the cell is repeated three times along z . On the top right, $n = 2$, the cell is repeated twice, while on the bottom left and right, the $(\text{CrAs})_3/(\text{GaAs})_3$ and $(\text{CrAs})_5/(\text{GaAs})_5$, respectively, is presented. For $(\text{CrAs})_5/(\text{GaAs})_5$ the individual Cr-layers are marked in agreement with section 3.3.5. . . .	76
3.18	Overview of the total density of states of LSDA and LDA+DMFT for $(\text{CrAs})_n/(\text{GaAs})_n$ for $n = 1, 2, 3, 5$	79
3.19	Comparison of the total density of states of LSDA and LDA+DMFT for $(\text{CrAs})_n/(\text{GaAs})_n$ for $n = 1, 2$; the results from LSDA are shown as solid black line, the results from DMFT as broken red line.	81
3.20	Comparison of the total density of states of LSDA and LDA+DMFT for $(\text{CrAs})_n/(\text{GaAs})_n$ for $n = 3, 5$; the results from LSDA are shown as solid black line, the results from DMFT as broken red line. In the upper plot the inset shows the LSDA-results around the gap with a reduced broadening of 0.004eV.	82
3.21	Density of states from LSDA (top) and from DMFT (bottom) for the Cr- <i>d</i> -orbitals of $(\text{CrAs})_5/(\text{GaAs})_5$ in comparison to the density of states from DMFT for the Cr- <i>d</i> states in bulk CrAs with the same lattice constant.	84
3.22	Density of states calculated with LSDA (left) and DMFT (right) for $(\text{CrAs})_1/(\text{GaAs})_1$ using different lattice constants: black denotes the lattice constant obtained from an optimized spin GGA-calculation [4] ($a_0 = 5.75\text{\AA}$), results shown in red use GaAs-lattice constant found in experiment ($a_0 = 5.65\text{\AA}$).	87
3.23	Density of states calculated with LSDA (left) and DMFT (right) for $(\text{CrAs})_3/(\text{GaAs})_3$ using different lattice constants: black denotes the lattice constant obtained from an optimized spin GGA-calculation [4] ($a_0 = 5.75\text{\AA}$), results shown in red use GaAs-lattice constant found in experiment ($a_0 = 5.65\text{\AA}$).	88
3.24	Energy-dependent polarization obtained from LSDA (top) and LDA+DMFT (bottom) for $(\text{CrAs})_n/(\text{GaAs})_n$ for $n = 1, 2, 3, 5$	90
3.25	Octahedral environment formed by the Ti-atoms (large, red spheres) around the N atom (small, blue sphere). The unit cell is represented by the black lines; the subset of Ti-atoms connected by dashed lines shows the cluster geometry that was used as reference system for the LDA+VCA-calculation (see text).	92

3.26	Orbital-resolved density of states for TiN obtained by LDA and LDA+U. The upper (lower) panel shows the Ti- t_{2g} (e_g) contribution. The upper panel also displays the N- p density of states and the experimental XPS spectrum [5] (Experimental data reproduced with kind permission of the authors).	94
3.27	Band structure of TiN calculated for a path in the Brillouin zone (BZ) going from the L -point (0.5, 0.5, 0.5) trough the Γ (0, 0, 0), X (0, 1, 0), W (0.5, 1, 0), L (0.5, 0.5, 0.5), K (0, 0.75, 0.75) points and ending at the Γ point (0, 0, 0). The bands shown as dashed/green lines are obtained from the LDA calculation for the complete orbital basis set. The NMTO bands (full/red line) are obtained after downfolding to the Ti- $3d(t_{2g})$ orbitals.	95
3.28	TiN density of states calculated with LDA+VCA for different values of the Coulomb-interaction parameter U and for the Hund's rule coupling $J = 1.3$	99
3.29	TiN density of states calculated within LDA+VCA for $U = 8.5\text{eV}$ and $J = 1.3$ compared with measured XPS [5] and K-ELNES [6] spectra (Experimental data reproduced with kind permission from the authors).	100
3.30	Density of states for TiN calculated with a reference system consisting of four sites: shown in black are the results from the full calculation and depicted as red, dashed line the result for the atomic limit at the same value of the chemical potential. For this choice of the reference system the hopping terms included in the full calculation mainly broaden the peaks caused by onsite energies and interaction terms.	101
3.31	Density of states from a six sites calculation with onsite-, correlation-terms and the largest hopping terms treated only within the CPT approximation (black solid line); in comparison the result from a full calculation for the four sites reference system is shown as red dashed line.	102
3.32	Spectral-function of TiN for $U = 8.5$ and $J = 1.3$ shown as density plot for the same path in the BZ as in Fig. 3.27. The bands obtained from downfolding (dashed, green lines) are shown as reference.	104
3.33	Real (top) and imaginary part (bottom) of the self-energy calculated for the same parameters and along the same BZ path as for the spectralfunction in Fig. 3.32. As real and imaginary part of the self-energy are not independent from each other as described by the Kramers-Kronig relations, we use the plot of the real part (top) to give an overview over a large energy range (identical to the density of states plot in Fig. 3.28) and the plot of the imaginary part (bottom) for a smaller energy range to show the region around the Fermi-energy in more detail.	105

D.1	The tetragonal CrO_2 -lattice showing the various cluster geometries employed as reference system: yellow and orange denote the two different Chromium-sites; the red lines denote the four sites cluster (located in the (110)-plane), extended by the green lines to six sites and doubled to eight sites by the blue lines.	120
D.2	Finite size effects: the most notable changes that occur by enlarging the reference system can be seen in the minority spin channel; here height and shape of the density of states is affected. In contrast to what one would expect there is more similarity between the results from the four and eight sites cluster than between the results from the six and eight sites cluster.	121
E.1	Reference system used for the LDA+VCA calculation; the red line denotes the used cluster. Note that due to the downfolding procedure only the Mn -sub lattice is considered.	125
E.2	LDA+VCA-results for NiMnSb using the Mn- d NMTO-basis set; a reduced Coulomb-interaction was used (see text): $U=0.75\text{eV}$, $J=0.9\text{eV}$.126	
E.3	Density of states for NiMnSb using Dynamical Mean field Theory (LDA+DMFT)[7]; $U= 3.0\text{eV}$, $J= 0.9\text{eV}$ were used for the Mn - d states. DOS obtained from LSDA is plotted for comparison.	127
E.4	Mn only Density of states obtained from DMFT[7]; $U= 3.0\text{eV}$, $J= 0.9\text{eV}$ were used. DOS obtained from LSDA is plotted for comparison. 128	
F.1	Density of states for NiMnSb within LDA+VCA (using the FLL-DCC) for a Coulomb-interaction $U = 2$ and Hund's rule coupling $\bar{J} = 0.6$ (shown as red, solid line) in comparison to results obtained from LSDA (black, dashed line).	132

List of Tables

Table	Page
2.1 Values of interaction terms $U_{ijij}n_{i\sigma}n_{j-\sigma}$ for an average Coulomb-interaction of $\bar{U} = F^0 = 1.1\text{eV}$ (with $F^2 = 6.7$, $F^4 = 4.2$), that yield an in-orbital interaction of $U = U_{iiii} = 2\text{eV}$ and an average $\bar{J} = 0.78\text{eV}$ (see text), all values in eV.	33
2.2 Values of interaction terms $U_{ijij}n_{i\sigma}n_{j\sigma}$ for an average Coulomb-interaction of $\bar{U} = F^0 = 1.1\text{eV}$ (with $F^2 = 6.7$, $F^4 = 4.2$), that yield an in-orbital interaction of $U = U_{iiii} = 2\text{eV}$ and an average $\bar{J} = 0.78\text{eV}$ (see text), all values in eV.	33

Chapter 1

Introduction

The theoretical understanding and description of interacting many-particle systems remains one of the great challenges in condensed matter physics. In the rather recent past, the discovery of high-temperature superconductors and heavy fermion compounds prompted an intense activity in the field of strongly-correlated systems. More recently, the discovery of peculiar properties in the two dimensional compound graphene and the high temperature superconductivity in non-cuprate materials, namely the iron pnictides, poses new challenges. In the field of spin-selective magnetism, to which a considerable part of this thesis is devoted, the discovery of the giant magnetoresistance by Peter Grünberg and Albert Fert earned the Nobel price in 2007. Despite it is a rather recent discovery, devices utilizing the GMR-effect - mostly hard-discs - are already in wide-spread use in consumer-devices and this is a good example showing how the industry can benefit from fundamental research. Further developments in this field lead to a variety of devices with new properties; another such example for a device already utilizing the electron spin is MRAM, see Fig. 1.1.

This is a new memory technology that stores information using parallel or antiparallel spin configurations. This has the advantage in comparison to conventional, charge based, memory that the information is retained even if the power is turned off¹.

Many of these exciting new materials consist of transition metals. While modern solid-state physics is able to explain physical properties of numerous materials, it is much harder to do so for materials with open d - and f -shells, like it is the case in transition metals. The reason for this is that electrons in these materials are localized, occupy narrow orbitals and experience strong Coulomb repulsion. For these strongly correlated systems, the strength of interactions between particles is comparable to or even larger than their kinetic energy. This is the reason why any theory that

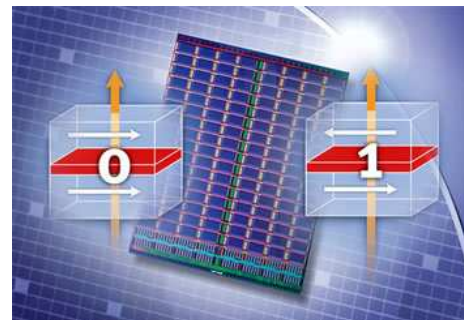


Figure 1.1: MRAM memory uses the electron spin to store information.

¹Picture courtesy of Lawrence Berkeley National Laboratory.

builds on a perturbative approach around the non-interacting limit is not suitable to describe these systems. The influence of an electron on the other is too pronounced for them to be treated independently.

Such strong electron interactions are at the origin of a variety of interesting properties, as small changes influence the system profoundly. Pressure, doping, also temperature can lead to a rich phase diagram with sometimes exotic ordering phenomena.

While all this makes the physics of these materials rather exciting, it makes it also hard to study theoretically their properties and simplifications have to be introduced to be able to study certain aspects.

1.1 Spintronics

Spintronics aims at revolutionizing electronic components by manipulating not only charge, as conventional electronics do, but also by utilizing the electron spin. While spin valves and spin filters are more of interest with respect to possible quantum computers, a spin field-effect transistor would enter the consumer market very quickly. Transistors are mostly used as the electronic equivalent of a mechanical switch and are present in nearly every electronic device, be it as complex as a computer with a CPU built up from billions of individual transistors to something as common as watches or a kitchen stove.

Indeed, there exists a theoretical proposal for a spin field-effect transistor² published by Datta and Das [8, 9] utilizing half-metallic ferromagnets as essential ingredient.

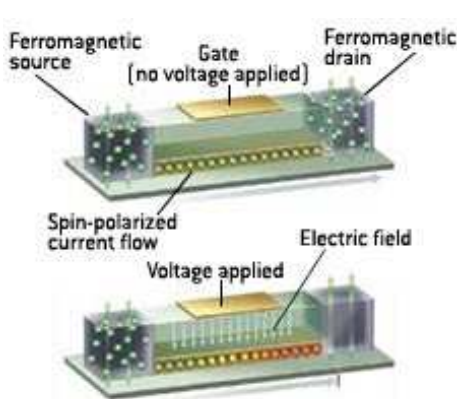


Figure 1.2: Principle of a spin field-effect transistor.

The way to this device is difficult, as the realization of half-metallic materials and the consequent assembly of such a complex device poses new and many problems.

Many half-metallic materials have been predicted from band-theory, but do not show these properties in experiment. In this thesis, theoretical investigations for a few of these materials show that electron correlations, which go beyond the LSDA, introduce states in the half metallic gap and change the properties of the material.

In addition, many half-metallic compounds are sensitive to impurities and lattice defects. Surfaces and interfaces also play a crucial role for the properties of many half-metallic ferromagnets and work on this aspect is also presented in this thesis.

²Picture courtesy of University of Delaware

1.2 Reasons for the necessity to go beyond the LDA

Density functional theory [10, 11] as formulated by W. Kohn and L. J. Sham around 1965 is still one of the most powerful and most widely used approaches to treat interacting many-body systems. During the last decades there has been an incredible progress to make this method robust, accurate and fast. Developments range from full potential basis sets that are highly accurate, to pseudopotential and muffin-tin potential methods that are fast. Other developments also include Green's function methods well suited to describe disordered systems [12].

Density functional theory has been very successful to reproduce experimental data for a wide range of materials. Despite its mean field character, the LDA-approximation is able to reproduce ground state properties of chemical elements that are characterized by orbitals with a localized nature like $4d$ and $5d$ -transition metals.

(3d) Transition metals

1 H																	2 He
3 Li	4 Be											5 B	6 C	7 N	8 O	9 F	10 Ne
11 Na	12 Mg											13 Al	14 Si	15 P	16 S	17 Cl	18 Ar
19 K	20 Ca	21 Sc	22 Ti	23 V	24 Cr	25 Mn	26 Fe	27 Co	28 Ni	29 Cu	30 Zn	31 Ga	32 Ge	33 As	34 Se	35 Br	36 Kr
37 Rb	38 Sr	39 Y	40 Zr	41 Nb	42 Mo	43 Tc	44 Ru	45 Rh	46 Pd	47 Ag	48 Cd	49 In	50 Sn	51 Sb	52 Te	53 I	54 Xe
55 Cs	56 Ba	71 Lu	72 Hf	73 Ta	74 W	75 Re	76 Os	77 Ir	78 Pt	79 Au	80 Hg	81 Tl	82 Pb	83 Bi	84 Po	85 At	86 Rn
87 Fr	88 Ra	103 Lr	104 Rf	105 Db	106 Sg	107 Bh	108 Hs	109 Mt	110 Ds	111 Rg	112 Cn	113 Uut	114 Uuq	115 Uup	116 Uuh	117 Uus	118 Uuo

Figure 1.3: Periodic table of elements; the transition metals form the block shown in red; as the main quantum number increases from top to bottom, the $3d$ -elements form the first row (high-lightened in green), picture courtesy of www.webelements.com

Despite all these successes there are materials where the LSDA turns out to be not well suited, with pure iron being a spectacular example. For elemental Fe LSDA predicts incorrect lowest energy crystal and magnetic structure (non magnetic and antiferromagnetic ordering with fcc unit cell are predicted to be lower in total energy than the experimentally found ferromagnetic bcc structure [13]). While a different approximation for the exchange and correlation energy, namely GGA, is able to give

better results [14], both GGA and LSDA give quite generally not so good results for the $3d$ -transition metals where local correlation effects are particularly strong due to inefficient screening (see also Fig. 1.3).

1.2.1 Methods for strongly correlated systems

The new LDA+VCA approach was developed to overcome these problems by treating local correlations exactly while long range order is still kept on a mean field-level. Of course the LDA+VCA approach is not the only method tailored to strongly correlated systems and therefore it is instructive to discuss its place among other methods.

A related approach to the many body problem is the LDA+DMFT method [15, 16] in which the correlation problem is mapped to a self-consistent single impurity problem. This method becomes exact in the limit of infinite coordination and is purely local, in other words, this method employs a self-energy that only depends on energy and orbital index. Consequently, it cannot be used to investigate non-local correlation effects as they are present in e.g. NiMnSb and TiN. While cluster extensions for the DMFT exist, they presently suffer from impractical numerical effort that limits their application to temperatures far above room temperature [17].

Yet another approach is to use quantum monte carlo (QMC) methods to solve the Hubbard-Hamiltonian directly; while this method is numerically exact in principle, it suffers in many cases for occupations away from half-filling from the infamous fermion-sign problem that poses severe numerical problems and limits in this cases its application practically to high temperatures and to small systems.

An entirely different approach to the many body problem are renormalization methods, like the density matrix renormalization group method (DMRG). While these allow to study large systems with very high precision, they are mainly used to study one-dimensional systems as their extension to higher dimensions poses difficulties.

In comparison to these methods the LDA+VCA approach does not suffer from these limitations. On the other hand, the main limitation of the LDA+VCA approach comes from the use of exact diagonalization which is a numerically intensive method. The exponential increase of the Hilbert-space with system size and occupation sets the practical limits of the cluster size and the number of orbitals per site that can be studied. Extending the LDA+VCA approach to finite temperatures further increases the required numerical effort.

In the next chapters, this new method is discussed in detail. Within the framework of this PhD thesis the LDA+VCA approach was applied for the first time to a number of very different systems with partially occupied $3d$ shells and these works are presented in the following chapters.

Chapter 2

The LDA+VCA-approach to correlated systems

Materials with partially filled d -shells constitute a challenge for solid state theory; the origin of this challenge comes from the fact that the electrons in these systems occupy narrow orbitals. Electrons in such orbitals are already on a technical level not well described by mean-field methods that use plane waves to describe the spatially extended character of the wave function like it is found in the homogeneous electron gas. While the choice of a less suitable basis to describe the electron wave-function may only reduce numerical efficiency and may also be circumvented with more sophisticated basis sets, electrons in narrow orbitals have a property that has far reaching implications; the Coulomb-repulsion between these electrons is only poorly screened. As a consequence electron-electron interaction causes effects that are of comparable magnitude to their kinetic energy. In these so-called strongly correlated systems, the local Coulomb-interaction is in competition with the non-local mean-field caused by the ions and other electrons.

Models that are more appropriate to describe such electrons that are strongly localized and experience strong interaction are the so-called 'tight-binding' models. One of the most prominent tight-binding models is the Hubbard-model [18, 19, 20, 21], where explicitly a Coulomb-repulsion between electrons on the same atom is taken into account. Despite dating back to 1963 and despite its apparent simplicity, it is still one of the most widely used and sophisticated models to describe electron correlations in d -shell systems.

The used tight-binding model is within LDA+VCA, however, only part of a bigger picture. To model real-world compounds one has to calculate realistic parameters, ideally derived ab-initio, to enter the used model. Further, one has to employ an efficient solver, as performing exact diagonalization is practically possible only for small systems.

The LDA+VCA-approach presented in the following is a new approach that was applied for the first time to a number of systems where electron correlations play a crucial role in describing low energy physics.

2.1 The Hubbard-model

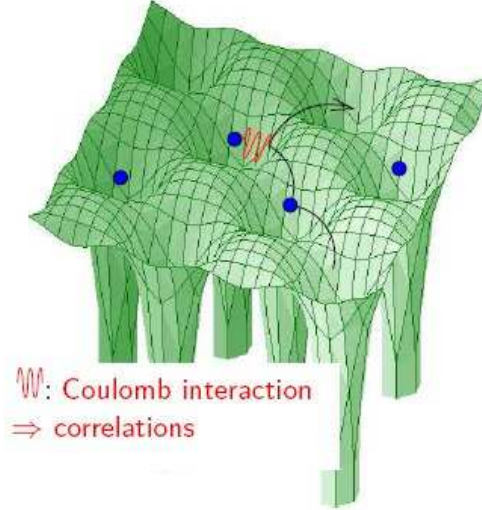


Figure 2.1: The two basic processes in the Hubbard-model: the arrows denote the hopping of the electron (shown as dot) between lattice sites (shown as center of the potential well), the red wiggle the scattering due to Coulomb-interaction. Picture courtesy of K. Held [1]

J. Hubbard proposed a simple model that contains the minimum processes to yield both band-like and localized behavior in suitable limits. The large number of energy levels of each ion is reduced to a single localized orbital level, which can have four possible states: empty or occupied by one electron of either spin or completely occupied with two electrons of opposite spin-directions. While considering only a single orbital may appear to be a very crude approximation, low energy and low-temperature properties may be still well described by such a model as in many materials only a small number of bands cross Fermi-energy [22] and influence low-energy excitations.

The Hubbard-model consists essentially of two processes which are in competition with each other (see Fig. 2.1). One process is hopping, whereby electrons delocalize by propagating between orbitals on different atomic sites,

$$H_0 = \sum_{\mathbf{R}_j, \mathbf{R}_i, \sigma} t^{\mathbf{R}_j - \mathbf{R}_i} c_{\mathbf{R}_j \sigma}^\dagger c_{\mathbf{R}_i \sigma}, \quad (2.1)$$

with

$$t^{\mathbf{R}_j-\mathbf{R}_i} = \int d\mathbf{r} \phi_i^*(\mathbf{r}) \left\{ -\frac{\hbar^2}{2m_e} \Delta + \underbrace{\sum_l \frac{-e^2}{4\pi\epsilon_0} \frac{Z_l}{|\mathbf{r}-\mathbf{R}_l|}}_{\equiv V_{\text{ion}}(\mathbf{r})} \right\} \phi_j(\mathbf{r}), \quad (2.2)$$

where $t^{\mathbf{R}_j-\mathbf{R}_i}$ denotes the hopping amplitude of an electron propagating from the orbital at point \mathbf{R}_i (denoted as atomic Wannier-orbital $\phi_i = \phi(\mathbf{r}-\mathbf{R}_i)$) to the orbital at point \mathbf{R}_j . $c_{\mathbf{R}\sigma}$ ($c_{\mathbf{R}\sigma}^\dagger$) are the usual fermionic annihilation (creation) operators acting on an electron with spin σ . $V_{\text{ion}}(\mathbf{r})$ is the attractive Coulomb-interaction caused by the lattice ions which have the charge $Z_l e$ and are located at \mathbf{R}_l . ϵ_0 and \hbar are the vacuum dielectric and Planck's constant, respectively.

The hopping amplitude $t^{\mathbf{R}_j-\mathbf{R}_i}$ is a degree of freedom in the Hubbard-model and has to be chosen by physical arguments. In the presented LDA+VCA approach these parameters are calculated ab-initio for the material in question and this will be discussed in more detail in chapter 2.2.

Quite generally, hopping lowers the energy of the system as delocalization of the electrons reduces the effective interaction between them and leads to an effective screening of the Coulomb-repulsion. As can be shown [23], consideration of only the hopping process leads to a conventional band structure and to one-electron Bloch-levels in which the electrons are distributed among the whole lattice.

The opposing force working against delocalization is Coulomb-interaction; it can be written in general form as

$$\frac{1}{2} \sum_{ijmn\mathbf{R}\sigma\sigma'} U_{ijmn} c_{i\mathbf{R}\sigma}^\dagger c_{j\mathbf{R}\sigma'}^\dagger c_{n\mathbf{R}\sigma} c_{m\mathbf{R}\sigma'} \quad (2.3)$$

with

$$U_{ijmn} = \int d\mathbf{r} \int d\mathbf{r}' \phi_i^*(\mathbf{r}) \phi_j(\mathbf{r}) \underbrace{\frac{1}{4\pi\epsilon_0} \frac{e^2}{|\mathbf{r}-\mathbf{r}'|}}_{V_{ee}(\mathbf{r}-\mathbf{r}')} \phi_m^*(\mathbf{r}') \phi_n(\mathbf{r}'). \quad (2.4)$$

In this form, two electrons are initially located at atomic positions \mathbf{R}_k and \mathbf{R}_l and scatter due to Coulomb-repulsion $V_{ee}(\mathbf{r}-\mathbf{r}')$ into positions located at \mathbf{R}_m and \mathbf{R}_n . The four orbitals in these so-called four center integrals can be located at four different sites, which makes the integrals difficult to carry out. As these four center terms are usually small [24], they are generally neglected and only certain terms are considered. Hubbard approximated Eq. (2.4) by retaining only the largest Coulomb-terms, namely the terms describing purely local interaction between two electrons on the same atom $\mathbf{R}_k = \mathbf{R}_l = \mathbf{R}_m = \mathbf{R}_n$,

$$U_{kkkk} = \int d\mathbf{r} \int d\mathbf{r}' V_{ee}(\mathbf{r}-\mathbf{r}') |\phi_k(\mathbf{r})|^2 |\phi_k(\mathbf{r}')|^2. \quad (2.5)$$

As the Pauli-principle does not allow electrons to be in exactly the same state, they must be in different spin configurations as the simplest form of the Hubbard-model considers only a single orbital on each atom. The Coulomb-repulsion favors localization and the formation of local moments as it reduces the possibility of a second electron (with opposite spin) in the same orbital.

The important parameter in the single-band Hubbard-model is the Coulomb-repulsion expressed in the energy scale of the hopping, U/t . Depending on the filling n one can distinguish different cases, e.g. $n = 0$ and $n = 2$ give a band insulator. At half-filling, $n = 1$, it is believed that the Coulomb-repulsion U induces a metal-insulator transition at a critical value U_c/t .

With the two mechanisms, hopping and Coulomb-repulsion, the model is able to give metallic behavior for $t \gg U$ and insulating behavior for $U \gg t$ alike. Already this apparently simple description is sufficient to describe metals and insulators alike and the transition between them.

In the following sections 2.2 and 2.3, the Hubbard-model presented here is extended to a more general form describing multiatomic and multiorbital systems as that is needed for a more realistic treatment of electrons in real compounds. Further, it will be outlined in detail how realistic hopping parameters can be calculated ab-initio for the compounds in question.

2.2 Ab-initio construction of the single particle part of the Hamiltonian

In Eq. (2.1) the single particle part of the Hubbard-Hamiltonian was defined for a single band. This equation is now extended to a multiatomic and multiorbital form,

$$H_0 = \sum_{\mathbf{R}_j, \mathbf{R}_i, \sigma} \sum_{\{A, B, m', m\}} t_{m', m}^{B-A, \mathbf{R}_j - \mathbf{R}_i} c_{B\mathbf{R}_j m' \sigma}^\dagger c_{A\mathbf{R}_i m \sigma}, \quad (2.6)$$

where $t_{m', m}^{B-A, \mathbf{R}_j - \mathbf{R}_i}$ denotes the hopping amplitude for an electron propagating from orbital m of atom A at point \mathbf{R}_i to orbital m' of atom B at point \mathbf{R}_j . Within the LDA+VCA approach, the coefficients $t_{m', m}^{B-A, \mathbf{R}_j - \mathbf{R}_i}$ are given by the material and depend largely on crystal and orbital symmetries, as well as the corresponding overlaps of the wave functions in real space.

To calculate these parameters we use a combination of a powerful downfolding technique with density functional theory, called NMTO. The method was developed by O. K. Andersen [25, 26] and allows to downfold the full basis set onto a reduced, chosen, basis. This method fulfills the requirement that the bands calculated with the reduced basis set agree with the corresponding parts of the band structure obtained from a full calculation with the complete basis set. From the bands obtained from

the reduced basis set the hopping amplitudes are calculated in a last step by Fourier-transformation.

2.2.1 The N th order muffin-tin-orbitals scheme (NMTO)

By using the Stuttgart NMTO-band program¹, it is possible to calculate the hopping amplitudes with density functional theory for the material of interest. This is done by calculating the $t_{m',m}^{B-A,\mathbf{R}_j-\mathbf{R}_i}$ as expectation value of the DFT-Hamiltonian calculated for the two atomic Wannier orbitals, ϕ_{Aim} and $\phi_{Bjm'}$, respectively,

$$t_{m',m}^{B-A,\mathbf{R}_j-\mathbf{R}_i} = \int d\mathbf{r} \phi_{Bjm'}^*(\mathbf{r}) \left[-\frac{\hbar^2 \Delta}{2m_e} + V_{\text{ion}}(\mathbf{r}) + \int d\mathbf{r}' \rho(\mathbf{r}') V_{ee}(\mathbf{r}-\mathbf{r}') + \frac{\delta E_{xc}(\rho(\mathbf{r}))}{\delta \rho(\mathbf{r})} \right] \phi_{Aim}(\mathbf{r}), \quad (2.7)$$

where in comparison to the previous definition in Eq. (2.1) now also the electron-electron interaction V_{ee} and the exchange-correlation energy δE_{xc} is taken into account. While this expression is exact in principle, the last term, δE_{xc} , is unknown and has to be approximated. Within the LDA+VCA approach, the local density approximation (LDA) was used to calculate the exchange-correlation energy.

In order to calculate these parameters, we employ the N th order muffin-tin-orbitals (NMTO) method [25, 26]. We use this scheme to generate truly minimal² basis sets in combination with a downfolding technique (the principle of Löwdin-downfolding is sketched in Appendix C). This minimal basis forms a localized basis set with specific orbital characters, like e.g. d -orbitals. Within NMTO there are no restrictions for the choice of the reduced basis; it is not only possible to downfold to the full d -manifold, but also to a subset of it like the t_{2g} -orbitals or even to a single orbital.

Practical choice of the reduced basis Within the LDA+VCA approach, the reduced basis set is chosen by physical arguments specifically for the material in question. Usually, one uses the band structure obtained from LDA to determine which orbitals are close to or even cross the Fermi-energy and are therefore important for low-energy properties. As the numerical effort of VCA grows exponentially with the number of orbitals in the basis, it is generally of major interest to keep the basis as small as possible. Consequently, while it is clear that for transition metals the d -orbitals are close to the Fermi-energy, one tries to reduce the basis further. Whether this can be achieved, depends on a number of factors like the filling of the d -orbitals. However, as discussed in the corresponding chapters, it was possible to reduce the basis to the

¹The Stuttgart NMTO-band program (version 47.7) of Ole Krogh Andersen and Tanusri Saha-Dasgupta, Max-Planck-Institut für Festkörperforschung, Heisenbergstrasse 1, D-70569 Stuttgart

²A truly minimal basis set needs only the same number of basis functions as there are bands to describe.

t_{2g} -orbitals for CrO_2 (see chapter 3.1) and also for TiN (see chapter 3.4), while for NiMnSb even the full $Mn-d$ manifold was not sufficient (see chapter 3.2). The basis to which one downfolds is usually chosen by its distance to the Fermi-energy. For many systems this approach works very well, but there are exceptions, especially in compounds with more than one atom with partially filled d -orbitals. An example is the case of NiMnSb, where both Ni and Mn have partially filled d -shells near the Fermi-energy. As the $Ni-d$ states are lying deeper in energy than the $Mn-d$ states, it is tempting to focus on only the $Mn-d$ states. However, as also the $Ni-d$ states are correlated, the Coulomb-interaction has to be considered in these orbitals as well. The Hubbard- U causes a significant splitting of the $Ni-d$ onsite energies. In combination with the fact that the $Ni-d$ states are nearly completely filled, it follows that some of these $Ni-d$ states are even closer to Fermi-energy than the $Mn-d$ -states and play therefore a significant role.

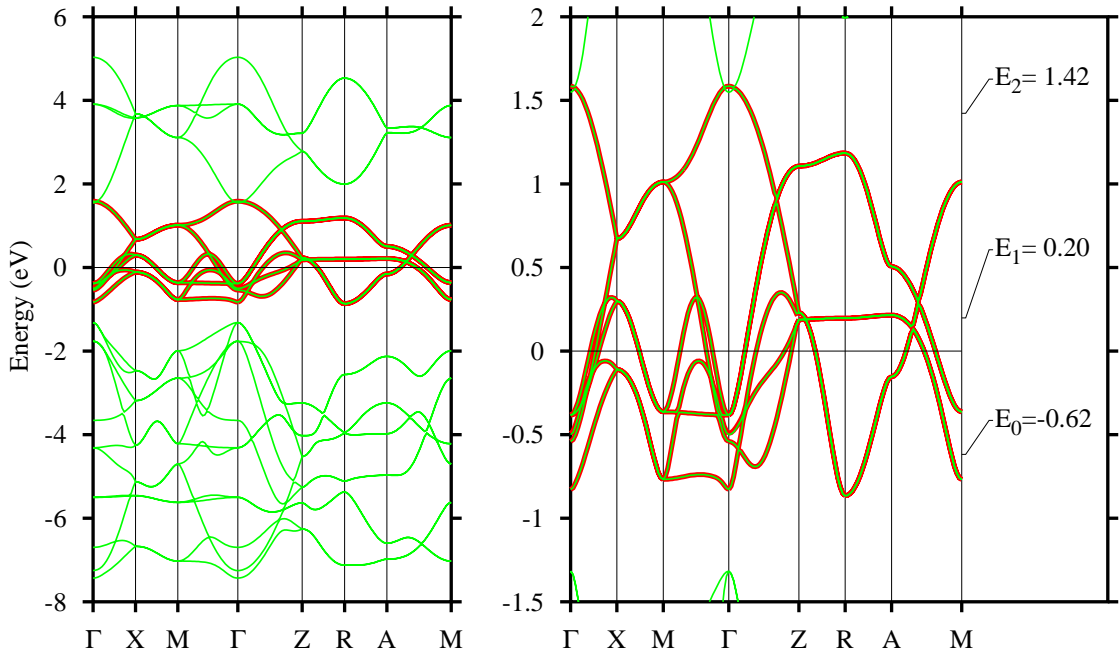


Figure 2.2: Plot of the $\text{Cr-}t_{2g}$ bands of CrO_2 (see also chapter 3.1) obtained from downfolding within NMTO in comparison to the full band structure obtained from LDA [2]. E_i (with $i = 1, 2, 3$) denote the used energy expansion points (values in eV).

After choosing the basis, the NMTO downfolded bands are obtained by expanding around a (usually) small number of energy points E_i . The choice of the number and

magnitude of the E_i 's is done in a trial and error fashion, as there is no analytical prescription for this task. In a step by step procedure a number of E_i 's is introduced and initially roughly equally distantly distributed within the energy range that is spanned by the bands of interest. Further, from experience it is known that band crossings need an E_i in their close vicinity. After this initial choice, the bands are calculated within NMTO and exhibit at first in general rough deviations from the bands obtained from a full basis set calculation. The form of the deviations range from bands that are constantly shifted in energy to severe distortions that are located at band crossings or at energies where hybridization with other bands is significant. By optimizing the number and magnitude of the E_i 's it is usually possible to get near perfect agreement to the bands obtained from a full basis set calculation. An example for the agreement of the downfolded bands with the full band structure is shown in Fig. 2.2. In case of isolated bands the reduced basis set is able to reproduce the bands from the full calculation even to arbitrary precision [26] provided one has a sufficiently dense energy mesh.

In this way, the non-interacting part of the effective Hamiltonian is confined to the chosen set of orbitals and, as a consequence, to a reduced energy window, usually chosen to be around Fermi-energy.

In a last step, Fourier-transformation of the orthonormalized NMTO Hamiltonian, $\tilde{H}^{\text{LDA}}(\mathbf{k})$, yields conveniently on-site energies and hopping integrals,

$$\langle \phi_{B\mathbf{R}'m'} | H^{\text{LDA}}(\mathbf{r}) - \varepsilon_F | \phi_{A\mathbf{R}m} \rangle \equiv t_{m',m}^{B-A,\mathbf{R}'-\mathbf{R}}, \quad (2.8)$$

in a Wannier representation, where the NMTO Wannier functions $|\phi_{A\mathbf{R}m}\rangle$ are orthonormal.

2.3 The Coulomb-interaction part of the Hamiltonian

When studying correlation effects in compounds, the interaction part of the Hamiltonian plays an important role. It shall include as many relevant processes as possible while still has to be solvable. While for single orbital systems only a single onsite interaction term can be introduced, the situation becomes progressively more complex with increasing number of orbitals. In this chapter a derivation of a full spin-invariant interaction Hamiltonian is discussed and it is shown by how much it becomes simpler just by neglecting two e_g -orbitals.

2.3.1 Derivation

The basic interaction part of the Hubbard-model was already discussed in chapter 2.1. To describe real compounds it is necessary to go beyond a single orbital per atom. However, the second basic approximation of the Hubbard-model, namely that the interaction is purely localized at the atom, is still used. To describe electron-electron

interaction in multiorbital systems it is necessary to consider not only Coulomb-interaction that is present between all electrons on the same atom, but also the Hund's rule coupling that lowers the Coulomb-repulsion between electrons of the same spin direction. In this section only the derivation of the Coulomb-interaction for multiorbital systems is outlined for simplicity. The more general derivation including the reduction of the Coulomb-interaction between two electrons of parallel spin due to Hund's rule coupling, J_{ijmn} , is similar.

To describe d -shell systems, we consider in the following the full d -manifold, that is five orbitals per atom. In case only a subset of orbitals is necessary to describe a material, only the corresponding terms are projected out of the full interaction part of the Hamiltonian. For the derivation we follow [27]; starting point is again Eq. (2.4),

$$U_{ijmn} = \frac{1}{4\pi\epsilon_0} \int d\mathbf{r} \int d\mathbf{r}' \phi_i^*(\mathbf{r}) \phi_j(\mathbf{r}) \frac{e^2}{|\mathbf{r} - \mathbf{r}'|} \phi_m^*(\mathbf{r}') \phi_n(\mathbf{r}') \quad (2.9)$$

$$U_{ijmn} := \langle \phi_i \phi_j | V_{ee} | \phi_m \phi_n \rangle,$$

with

$$V_{ee}(\mathbf{r}, \mathbf{r}') := \frac{1}{4\pi\epsilon_0} \frac{e^2}{|\mathbf{r} - \mathbf{r}'|} \quad (2.10)$$

where the indices $i, j, m, n = (1 - 5)$ now denote different d -orbitals centered at the same atom.

Rewriting V_{ee} in spherical coordinates (r, θ, ϕ) gives

$$V_{ee} = \frac{1}{4\pi\epsilon_0} \frac{e^2}{|\mathbf{r} - \mathbf{r}'|} = \frac{e^2}{\sqrt{r_1^2 + r_2^2 - 2r_1 r_2 \cos \omega}}, \quad (2.11)$$

where ω is the angle between r_1 and r_2 ,

$$\cos(\omega) = \cos(\theta_1) \cos(\theta_2) + \sin(\theta_1) \sin(\theta_2) \cos(\phi_1 - \phi_2). \quad (2.12)$$

For $r_1 \neq r_2$ we denote $r_<$, $r_>$ for the smaller or larger of r_1 and r_2 , respectively. Expanding above expression into a power series in $r_</r_>$ gives

$$V_{ee} = \frac{1}{4\pi\epsilon_0} \frac{e^2}{r_>} \left(1 + \frac{r_<^2}{r_>^2} - 2\frac{r_<}{r_>} \cos \omega\right)^{-1/2}$$

$$= \frac{1}{4\pi\epsilon_0} \frac{e^2}{r_>} \sum_{k=0}^{\infty} \frac{r_<^k}{r_>^k} P_k(\cos \omega), \quad (2.13)$$

where the $P_k(\cos \omega)$ are Legendre-polynomials. Using the spherical harmonic addition theorem,

$$P_l(\cos \omega) = \frac{4\pi}{2l+1} \sum_{m=-l}^{+l} Y_{lm}(\theta_1, \phi_1) Y_{lm}^*(\theta_2, \phi_2), \quad (2.14)$$

together with (2.13) and separating into a radial and angular part, we obtain

$$U_{ijmn} = \sum_{k=0}^{2l} a_k(i, j, m, n) F^k. \quad (2.15)$$

The newly introduced abbreviations are the Slater-integrals F^k

$$F^k = \frac{1}{4\pi\epsilon_0} \int r_1^2 dr_1 \int r_2^2 dr_2 (e^2 r_{<}^k / r_{>}^{k+1}) R_{3d}(r_1)^2 R_{3d}(r_2)^2 \quad (2.16)$$

(with R_{3d} being the radial part of the wave function) and their coefficients [28]

$$a_k(i, j, m, n) = \frac{4\pi}{2k+1} \sum_{q=-k}^k \langle Y_{li} | Y_{kq} | Y_{lj} \rangle \langle Y_{lm} | Y_{kq}^* | Y_{ln} \rangle. \quad (2.17)$$

The Y_{lm} (l is the angular quantum number of the interacting orbitals, for d -orbitals $l = 2$) denote spherical harmonics and these terms can be calculated using Clebsch-Gordon coefficients (or Gaunt numbers, see Appendix in [29]).

The following relations show how the Slater-integrals are related to the interaction-terms; if one defines an orbitally averaged Coulomb-interaction \bar{U} and Hund's rule exchange coupling \bar{J} ,

$$\begin{aligned} \bar{U} &= \frac{1}{(2l+1)^2} \sum_{ij} U_{ijij} \\ \bar{J} &= \frac{1}{(2l+1)^2} \sum_{ij} J_{ijij}, \end{aligned} \quad (2.18)$$

one can show by using properties of the Clebsch-Gordon coefficients that following sum-rules apply [29]

$$\begin{aligned} \bar{U} &= F^0 \\ \bar{J} &= (F^2 + F^4)/14. \end{aligned} \quad (2.19)$$

F_0 represents the isotropic part of the Coulomb-interaction and is equal to the average Coulomb-interaction \bar{U} , whereas intra-atomic exchange and the anisotropic Coulomb-interaction is caused by Slater-integrals F^2 and F^4 [22].

The interaction is now expressed in terms of Slater integrals; however in practice one often prefers a different form that allows to define a certain interaction $U = U_{iiii}$ and then calculate the appropriate values of the Slater-integrals needed, in order to calculate the full U -matrix. In case of the d -electrons ($l = 2$) only the Slater-integrals F^0 , F^2 and F^4 are required. To simplify things further, one can very well approximate the ratio F^4/F^2 for the $3d$ -electrons with the constant 0.625 [30, 31]. If

one focuses on the t_{2g} -orbital subset only, one can derive following relations between U_{iii} , U_{ijij} and the Slater-integrals F^k (Table II on page 1128 in [22]³)

$$\begin{aligned}
 U^{t2g} &= U_{iii}^{t2g} = F^0 + \frac{4}{49}F^2 + \frac{36}{441}F^4 \\
 U^{t2g,'} &= U_{ijij}^{t2g} = F^0 - \frac{2}{49}F^2 - \frac{4}{441}F^4 \\
 J^{t2g} &= \frac{3}{49}F^2 + \frac{20}{441}F^4
 \end{aligned} \tag{2.20}$$

which has the property

$$\begin{aligned}
 U^{t2g} - U^{t2g,'} &= \left\{ \left(\frac{4}{49} + \frac{36 \times 0.625}{441} \right) + \left(\frac{2}{49} + \frac{4 \times 0.625}{441} \right) \right\} F^2 \\
 &= 2J^{t2g}.
 \end{aligned} \tag{2.21}$$

Using these relations it is easy to calculate the Slater-integrals that give a certain Coulomb-interaction.

2.3.2 Interaction-part of the Hamiltonian

Within this section we want to discuss the terms of the interaction part of the Hamiltonian in more detail and from a more physical point of view. In the basic version of the Hubbard-model with only a single orbital per atom it is sufficient to state only a single interaction term U to describe the Coulomb-interaction in this system. The Coulomb-interaction of a multiorbital system is on one hand much more complicated as it considers also the Coulomb-repulsion between electrons located in different orbitals and on the other hand becomes in addition orbital dependent due to the different spatial overlaps of the involved orbitals.

full d -orbitals

To describe multiatomic systems, the interacting part of the Hamiltonian for the full d -manifold of atom A is equivalent to Eq. (2.3) with an additional atom index,

$$H_I = \frac{1}{2} \sum_{\mathbf{R}, A, \sigma, \sigma'} \sum_{i, j, m, n} U_{ijmn}^A c_{\mathbf{R}i\sigma}^\dagger c_{\mathbf{R}j\sigma'}^\dagger c_{\mathbf{R}n\sigma'} c_{\mathbf{R}m\sigma}. \tag{2.22}$$

To gain insight into the processes and their magnitudes we consider in the following the case of a monoatomic basis, $U_{ijij} \equiv U_{ijij}^A$, with an in-orbital interaction $U =$

³There is a mistake in this table: the relations for u' and j are not correct; instead of $u' = F_0 - F_2 - 4F_4$ and $j = 5/2F_2 + 45/2F_4$ it should mean correctly $u' = F_0 - 2F_2 - 4F_4$ and $j = 3F_2 + 20F_4$

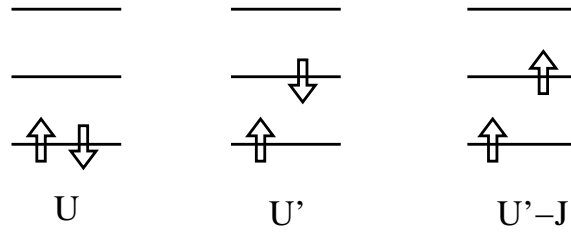


Figure 2.3: Scheme of the Coulomb-interactions present in the Hamiltonian schematically shown for the t_{2g} -orbitals; interaction between two electrons of different spin in the same orbital is denoted by $U = U_{iii}$, the interaction of electrons with different spins between different orbitals is denoted as $U' = U_{ijij}$, whereas Hund's rule leads to a reduced interaction $U' - J$ of electrons with parallel spins in different orbitals.

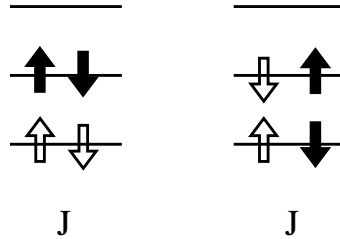


Figure 2.4: Additional interaction processes present in the Hamiltonian schematically shown for the t_{2g} -orbitals; on the left a pair-flip is depicted and on the right a spin-flip process. Empty and filled arrows denote the two electrons before and after the flip-process, respectively. For the t_{2g} -orbitals the coefficient of these processes, the Hund's rule coupling constant $J = J_{ijij}$, is independent of the indices of the involved orbitals.

$U_{iii} = 2\text{eV}$ and an orbitally averaged Hund's rule coupling $\bar{J} = 0.78\text{eV}$. While the in-orbital interaction takes the same value for all orbitals, the situation for the inter-orbital interactions $U' = U_{ijij}$ is much different. For this case different values depending on the orbitals involved are obtained, as the matrix depicted as Table 2.1 shows; the values for U' range in this example from as low as 0.62eV to more than twice that, 1.335eV .

The precise value of U' depends on the spatial overlap between the involved orbitals, as an example the spatial distribution of the individual Mn- d orbitals is shown as Fig. 2.5; so is the value 0.62eV the consequence of the small spatial overlap between the $(t_{2g})d_{xy}$ - and the $(e_g)d_{3z^2-1}$ -orbital and the largest value of 1.335eV occurs between the well overlapping $(t_{2g})d_{xy}$ and $(e_g)d_{x^2-y^2}$ -orbitals. The same is true for the Hund's rule coupling constant J_{ijij} , which takes the same value only for the t_{2g} -

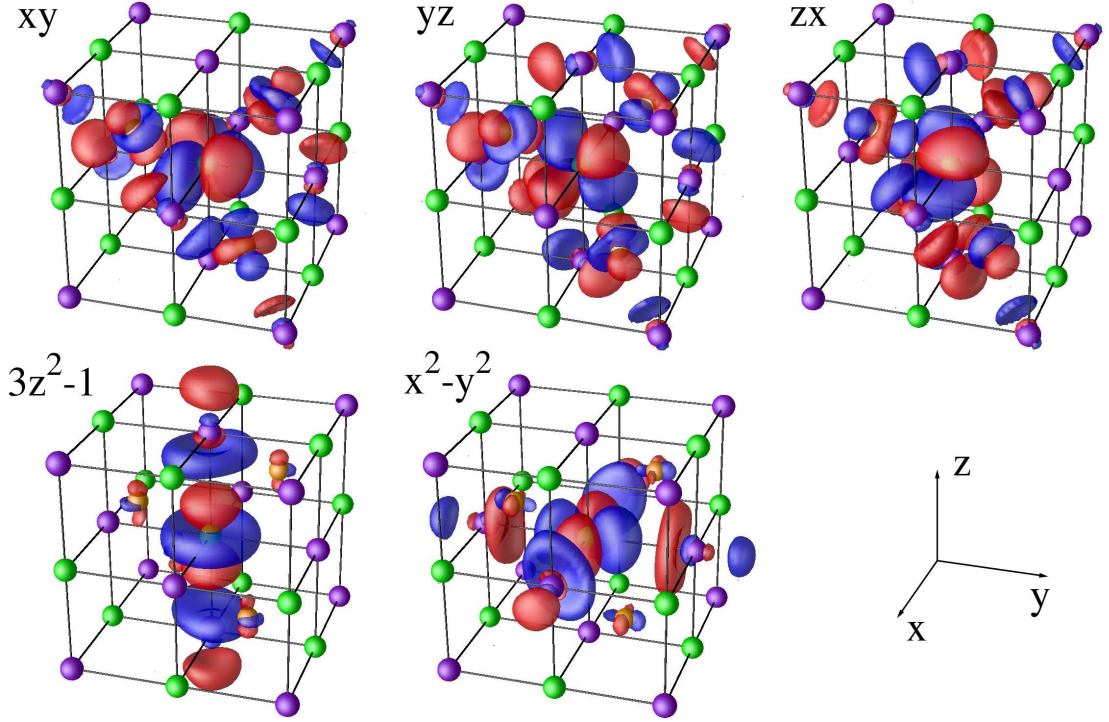


Figure 2.5: Illustration of the real-space distribution of the Mn- d -orbitals in NiMnSb; blue and red denote different phases.

subset. Consequently, the interaction between electrons with same spin in different orbitals, $U'' = U' - J$, depends on the indices of the involved orbitals and its values are listed in Table 2.2 for the same particular values of the Slater-parameters.

Furthermore, the full U -matrix contains also a number of terms that do not have the exact form of a density-density interaction; these terms have the general form $c_{i\sigma}^\dagger c_{j-\sigma}^\dagger c_{k\sigma} c_{l-\sigma}$ and represent flip and correlated hopping terms. So-called Spin- and pair-flip terms are of the form $c_{j\sigma}^\dagger c_{i-\sigma}^\dagger c_{i\sigma} c_{j-\sigma}$ and $c_{i\sigma}^\dagger c_{j-\sigma}^\dagger c_{i\sigma} c_{j-\sigma}$, respectively. These terms describe the simultaneous transition of both involved electrons between orbitals on the same atom, see Fig. 2.4.

Table 2.1: Values of interaction terms $U_{ijij}n_{i\sigma}n_{j-\sigma}$ for an average Coulomb-interaction of $\bar{U} = F^0 = 1.1\text{eV}$ (with $F^2 = 6.7$, $F^4 = 4.2$), that yield an in-orbital interaction of $U = U_{iiii} = 2\text{eV}$ and an average $\bar{J} = 0.78\text{eV}$ (see text), all values in eV.

	d_{xy}	d_{yz}	d_{xz}	d_{3z^2-1}	$d_{x^2-y^2}$
d_{xy}	2	0.8	0.8	0.62	1.335
d_{yz}	0.8	2	0.8	1.16	0.8
d_{xz}	0.8	0.8	2	1.16	0.8
d_{3z^2-1}	0.62	1.16	1.16	2	0.62
$d_{x^2-y^2}$	1.335	0.8	0.8	0.62	2

Table 2.2: Values of interaction terms $U_{ijij}n_{i\sigma}n_{j\sigma}$ for an average Coulomb-interaction of $\bar{U} = F^0 = 1.1\text{eV}$ (with $F^2 = 6.7$, $F^4 = 4.2$), that yield an in-orbital interaction of $U = U_{iiii} = 2\text{eV}$ and an average $\bar{J} = 0.78\text{eV}$ (see text), all values in eV.

	d_{xy}	d_{yz}	d_{xz}	d_{3z^2-1}	$d_{x^2-y^2}$
d_{xy}	-	0.2	0.2	-0.07	1.00
d_{yz}	0.2	-	0.2	0.74	0.20
d_{xz}	0.2	0.2	-	0.74	0.20
d_{3z^2-1}	-0.07	0.74	0.74	-	-0.07
$d_{x^2-y^2}$	1.00	0.20	0.20	-0.07	-

Another interesting process denote the so-called correlated hopping terms. They represent a form of conditional hopping between orbitals on the same site requiring an electron of opposite spin to be also located at the same site. This process becomes especially clear for the special case of $c_{i\sigma}^\dagger c_{j-\sigma}^\dagger c_{k\sigma} c_{j-\sigma}$, which can be rewritten into $n_{j-\sigma} c_{i\sigma}^\dagger c_{k\sigma}$. For d -orbitals this special case allows hopping between the two e_g -orbitals in the case that either the $(t_{2g})d_{yz}$ or $(t_{2g})d_{xz}$ is occupied with an electron of opposite spin,

$$\begin{aligned}
 & 0.15n_{d_{yz}-\sigma} c_{d_{3z^2-1}\sigma}^\dagger c_{d_{x^2-y^2}\sigma} \\
 & -0.15n_{d_{xz}-\sigma} c_{d_{3z^2-1}\sigma}^\dagger c_{d_{x^2-y^2}\sigma}
 \end{aligned} \tag{2.23}$$

(the coefficients are again given for an interaction of $U = 2\text{eV}$, $\bar{J} = 0.78\text{eV}$) and vanishes if both d_{yz} and d_{xz} are occupied.

$d(t_{2g})$ -orbitals

Things simplify substantially if one is allowed to reduce the orbitals of interest to the $d(t_{2g})$ -subfold only. As it can be already seen from above tabular, the interaction terms between t_{2g} -orbitals do not depend on the interacting orbitals, in other words the terms have always the same magnitude. Further, correlated hopping terms do not occur as these involve e_g -orbitals. Indeed it is possible to find simple relations between the interaction terms in this case. One finds following interaction-Hamiltonian

$$\begin{aligned}
 H_I &= \sum_{\mathbf{R},m} U n_{\mathbf{R}m\uparrow} n_{\mathbf{R}m\downarrow} \\
 &+ \sum_{\mathbf{R},m < m',\sigma,\sigma'} (U' - J\delta_{\sigma,\sigma'}) n_{\mathbf{R}m\sigma} n_{\mathbf{R}m'\sigma'} \\
 &+ \sum_{\mathbf{R},m < m'} J c_{\mathbf{R}m'\uparrow}^\dagger c_{\mathbf{R}m\downarrow}^\dagger c_{\mathbf{R}m'\downarrow} c_{\mathbf{R}m\uparrow} + \text{h.c.} \\
 &+ \sum_{\mathbf{R},m < m'} J c_{\mathbf{R}m'\uparrow}^\dagger c_{\mathbf{R}m'\downarrow}^\dagger c_{\mathbf{R}m\downarrow} c_{\mathbf{R}m\uparrow} + \text{h.c.}
 \end{aligned} \tag{2.24}$$

with following simple relations for the values of the Coulomb-interactions

$$\begin{aligned}
 J_{ijij} &= J \\
 U_{iiii} &= U
 \end{aligned} \tag{2.25}$$

for electrons with antiparallel spins, see Eq. (2.21) $U' = U_{ijij} = U - 2J$

for electrons with parallel spins the interaction is $U' - J = U - 3J$

It is interesting to note that these terms form a subset of the interacting Hamiltonian for the full d -orbitals as shown in 2.3.2. For the full case it is necessary to specify an orbitally averaged Hund's rule coupling, \bar{J} , as it is orbital-dependent. This dependence does not exist for the t_{2g} -subset. For the same values as discussed in the full d -case, $U = 2\text{eV}$ and $\bar{J} = 0.78\text{eV}$, the Hund's rule coupling acting on the t_{2g} -orbitals has the value $J = 0.6\text{eV}$, while $U = 2\text{eV}$ still applies.

2.3.3 Double counting correction (DCC)

The onsite-energies obtained from NMTO together with the effective hopping parameters already contain correlations on the LDA-level. Since we employ a multi-orbital Hubbard-model with explicit Coulomb-interactions, we need to correct this double counting of terms.

The LDA incorporates two correlation processes: a Hartree or mean-field interaction and a non-local Fock-like interaction. A simple correction of the onsite energies

can only correct the mean-field (Hartree) interaction and is not able to account for non-local Fock-like interactions. Consequently, only this process is corrected in the following.

As to how to properly correct this double counting of terms the situation is not at all completely clear; there exist alternative approaches in the literature and we will present our derived mean-field DCC and an alternative approach, Anisimov's DCC.

Mean-field double counting correction

We derive the mean-field DCC by calculating the contribution of the mean-field correlations to the onsite-energies to be consequently able to subtract them from the onsite-energy.

This happens as follows: the orbital occupation $n_{\mathbf{R}m\sigma}$, (i denotes site, σ spin and m orbital indices) can be written as the sum of the average, mean-field, occupation $\langle n_{m\sigma} \rangle$ and its fluctuation $\delta n_{\mathbf{R}m\sigma}$,

$$n_{\mathbf{R}m\sigma} = \langle n_{m\sigma} \rangle + \delta n_{\mathbf{R}m\sigma}. \quad (2.26)$$

Inserting this expression into the expression for the Coulomb interaction $U = U_{mmmm}$,

$$U \sum_{\mathbf{R},m} n_{\mathbf{R}m\uparrow} n_{\mathbf{R}m\downarrow}, \quad (2.27)$$

gives

$$U \sum_{\mathbf{R},m} n_{\mathbf{R}m\uparrow} n_{\mathbf{R}m\downarrow} \cong U \sum_{\mathbf{R},m} (\langle n_{m\downarrow} \rangle \delta n_{\mathbf{R}m\uparrow} + \langle n_{m\uparrow} \rangle \delta n_{\mathbf{R}m\downarrow}). \quad (2.28)$$

and additional products of $\langle \dots \rangle$, which we neglect as they give only a constant contribution, and additional products of $\delta \dots$, which we also discard as these are not taken into account in LDA. With the same arguments we approximate

$$\langle n_{m\downarrow} \rangle \delta n_{\mathbf{R}m\uparrow} \cong \langle n_{m\downarrow} \rangle n_{\mathbf{R}m\uparrow}. \quad (2.29)$$

The result is the Hartree-like term

$$U \sum_{\mathbf{R},m} \langle n_{m\uparrow} \rangle n_{\mathbf{R}m\downarrow}, \quad (2.30)$$

which contributes to the onsite energy

$$\sum_{\mathbf{R},m} \epsilon_m n_{\mathbf{R}m\sigma}. \quad (2.31)$$

Therefore we correct the onsite-energy ϵ_m of orbital m obtained from NMTO by using

$$\epsilon'_m = \epsilon_m - U \langle n_{m\sigma} \rangle \quad (2.32)$$

together with the occupation $n_{m\sigma}$ calculated within the LDA. As the LDA-scheme does not depend on spin, we have to use $n_{m\sigma} = \frac{1}{2}n_m$ which gives finally

$$\epsilon'_m = \epsilon_m - \frac{1}{2}U\langle n_m \rangle. \quad (2.33)$$

This calculation considered only the in-orbital Coulomb-interaction. In this specific case this expression yields only a shift which can also be absorbed in the physical chemical potential. Consequently, the double counting correction is not relevant in this case.

The derivation of the full double counting correction involving also the interaction between different orbitals is very similar to the one outlined and gives the following,

$$\epsilon'_m = \epsilon_m - \frac{1}{2} \left\{ U_{mmmm} \langle n_m \rangle - \sum_{m', m' \neq m} (U_{mm'mm'} + U'_{mm'mm'}) \langle n_{m'} \rangle \right\} \quad (2.34)$$

where

$$U'_{mm'mm'} = U_{mm'mm'} - J_{mm'mm'}. \quad (2.35)$$

In the literature this scheme is termed “around-mean-field” double counting correction [29, 32].

It is worthwhile to mention that the double counting correction is not necessary in the case of a reduced set of orbitals with the same spatial symmetries; in other words, if one considers only orbitals of the same symmetry, like for example the t_{2g} -orbitals in a cubic lattice, the occupations of these orbitals calculated within density functional theory do not differ from each other and consequently give the same correction to the onsite-energies. This common shift can, however, be absorbed in the chemical potential and is, therefore, irrelevant.

Furthermore, in the general case of a multi-orbital, but still monoatomic basis, this correction is more important but its influence is also often limited as differences in orbital occupation may be rather small and produce only a large, common global offset - which can be again absorbed into the chemical potential - with small individual deviations.

However, in the case of multiple different atoms in the basis, the correction can be quite substantial due to the large differences in atomic occupation that usually occur. In the case of NiMnSb for example, the Ni -states are about 1eV deeper in energy than the Mn -states. Consequently, Ni -states are nearly completely filled and as these large occupations enter the double counting correction, the Ni -onsite energies are shifted to even deeper lying energies (splitting between Ni and Mn about 3eV after correction).

Anisimov's double counting correction

Anisimov [31, 32] proposes another prescription for the double counting correction which gives the correct behavior in the fully localized limit (FLL). This is given by the following expressions

$$\epsilon'_m = \epsilon_m - U_{mmmm}(\langle n_m \rangle - \frac{1}{2}) - \sum_{m', m' \neq m} (U_{mm'mm'} + U'_{mm'mm'}) (\langle n_{m'} \rangle - \frac{1}{2}) \quad (2.36)$$

where again

$$U'_{mm'mm'} = U_{mm'mm'} - J_{mm'mm'}. \quad (2.37)$$

Both double counting corrections give the same changes to the onsite energies in the case of half-filling; this can be easily shown by setting $\langle n_m \rangle = 1$ where the terms become then,

in case of Anisimov DCC

$$(\langle n_m \rangle - \frac{1}{2}) = \frac{1}{2} \quad (2.38)$$

and in the case of the mean-field DCC

$$\frac{1}{2} \langle n_m \rangle = \frac{1}{2}. \quad (2.39)$$

2.4 Variational Cluster Approach

In the previous sections we introduced a multiatomic and multiorbital Hubbard-Hamiltonian that incorporates a sophisticated description of the Coulomb-interaction between electrons located on the same atom. To solve this Hamiltonian one can use in principle exact diagonalization methods. However, these methods suffer significantly from finite size effects due to the fact that only small systems can be solved practically. The inherent drawback of exact diagonalization is the large memory requirement as the Hilbert-space grows exponentially with cluster size and occupation.

The central idea of the VCA is to describe a large lattice by dividing it into smaller parts, so-called clusters, that can be treated by exact diagonalization (using Lanczos or similar methods). These clusters are in a next step coupled together using cluster perturbation theory (CPT) [33].

This has the advantage that, while long ranged correlations are still maintained on a mean-field level, correlations on the length scale of the cluster are treated exactly.

With the aid of the self-energy functional approach it is further possible to include a self-consistency scheme that allows to incorporate virtual operators. These virtual operators can be used to introduce symmetry breaking fields (like staggered fields for antiferromagnets or pairing fields for superconductors), as well as to ensure a thermodynamically consistent particle density.

2.4.1 Cluster Perturbation Theory

The basic principle of CPT is to divide the lattice into finite clusters containing N lattice sites (here we follow [34]),

$$H = \sum_{\mathbf{R}} \left\{ H_0^c(\mathbf{R}) + H_I(\mathbf{R}) \right\} + \sum_{\mathbf{R}, \mathbf{R}'} H_0(\mathbf{R}, \mathbf{R}'), \quad (2.40)$$

where H_0 denotes generally the non-interacting (single particle) part of the Hamiltonian, Eq. (2.6), with $H_0^c(\mathbf{R})$ being the part acting within the cluster located at \mathbf{R} and $H_0(\mathbf{R}, \mathbf{R}')$ being the part that connects different clusters located at \mathbf{R} and \mathbf{R}' (see Fig. 2.6), respectively. For simplicity only a single index is used (\mathbf{R}), depending on the problem the Hamiltonian may also depend on additional indices like an index to denote the site within the cluster and a spin and orbital index. $H_I(\mathbf{R})$ is the interacting part of the Hamiltonian and acts only within a cluster.

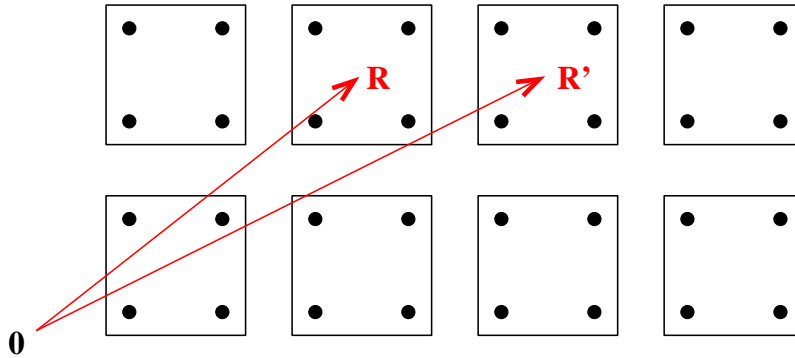


Figure 2.6: The lattice in this two dimensional example is divided into clusters (denoted as squares); the individual clusters are addressed by vectors \mathbf{R} and \mathbf{R}' . As generally the cluster consists of more than one lattice site (shown as black dots), additional indices are used to denote sites and orbitals within the cluster.

The hopping between the clusters, $H_0(\mathbf{R}, \mathbf{R}')$, is then treated in first order perturbation theory and one gets following relation

$$G^{-1}(\mathbf{R}, \mathbf{R}', \omega) = G^{c,-1}(\mathbf{R}, \mathbf{R}', \omega) - T(\mathbf{R}, \mathbf{R}') \quad (2.41)$$

where G is the lattice Green's function, G^c the cluster Green's function and the matrix $T(\mathbf{R}, \mathbf{R}')$ represents the hopping processes between different clusters⁴ ($T(\mathbf{R}, \mathbf{R}')$ vanishes necessarily if $\mathbf{R} = \mathbf{R}'$ as in that case $G^{-1} \equiv G^{c,-1}$).

⁴This is strictly true only within pure CPT; in VCA this term also contains virtual operators.

Further, it can be shown [34] that Eq. (2.41) is equivalent to

$$G^{-1}(\mathbf{R}, \mathbf{R}', \omega) = G_0^{-1}(\mathbf{R}, \mathbf{R}', \omega) - \Sigma^c(\omega) \quad (2.42)$$

where G_0 is the non-interacting Green's function and Σ^c the self-energy of the cluster. So, effectively, CPT approximates the self-energy of the lattice with the self-energy of the cluster.

This approach becomes exact in several limits:

1. $N \rightarrow \infty$ the limit of infinitely large clusters, as in that case the whole lattice is treated exactly
2. $T(\mathbf{R}, \mathbf{R}') \rightarrow 0$ the limit where all hoppings between clusters vanish
3. $U = 0$ the non-interacting limit as in that case $\Sigma = 0$ and Eq. (2.42) becomes exact

2.4.2 Self-energy functional approach

CPT itself does not have any self-consistency procedure and also does not allow the occurrence of symmetry breaking fields (like pairing fields in superconductors or staggered fields in antiferromagnets). Both issues are resolved in elegant fashion by the self-energy functional approach (SFA).

The self-energy functional approach was introduced quite recently by Potthof [35, 36] and is a general variational scheme to use dynamical information from an exactly solvable system (cluster, reference system) in order to obtain the infinite-lattice limit. As the SFA is very general, it is possible to construct a generic cluster approach which includes the CPT and cellular-DMFT as limits.

In combination with CPT, it defines a way to vary single particle operators such that the infinite lattice limit is recovered. This allows to include virtual fields as the self-consistency procedure is able to give a solution which is not symmetry broken.

To carry out this task, the SFA employs the universality of the Luttinger-Ward functional. In other words, the property that this functional does not depend on single-particle parameters t . This is done by first writing the grand canonical potential of the system (lattice) as a functional of the self-energy Σ

$$\Omega[\Sigma] = Tr \ln(G)^{-1} + F_U[\Sigma], \quad (2.43)$$

where $F_U\{\Sigma\}$ denotes the Legendre-transformed Luttinger-Ward functional, Σ the self-energy and G the full Green's function of the system. At the physical (self-consistent) self-energy $\Sigma = \Sigma_{t,U}$ this potential is stationary: $\delta\Omega_{t,U}[\Sigma_{t,U}] = 0$.

Next, one introduces a reference system, H' , which differs from the full system only in the single-particle part of the Hamiltonian,

$$H' = H_0(t') + H_1(U). \quad (2.44)$$

The grand canonical potential of this reference system is then

$$\Omega^c[\Sigma] = Tr \ln(G^c)^{-1} + F_U[\Sigma]. \quad (2.45)$$

Due to the universality of the Luttinger-Ward functional, $F_U[\Sigma]$ is the same in both cases. Combining both equations (2.43), (2.45) and using the self-energy of the reference system Σ^c as trial self-energy, one yields

$$\Omega[\Sigma^c] = \Omega^c[\Sigma^c] + Tr \ln(G^{VCA})^{-1} - Tr \ln(G^c), \quad (2.46)$$

where Ω^c is the grand canonical potential of the reference system and G^c the full Green's function of the reference system.

Thus, to get a self-consistent solution, one has to find a saddle point of Eq. (2.46) in the space spanned by the single particle parameters of the full Hamiltonian H . As this is practically not possible, one has to approximate this space by the subspace of the reference system.

In principle *all* single particle parameters of H_0^c should be varied to give an optimal result. This, however, is - with the exception of the most simple systems - impractical due to the high dimension of the resulting parameter space. Consequently, one focuses on a few variational parameters, which are chosen using physical arguments.

Virtual operators

CPT itself is not able to account for symmetry breaking fields which are essential for various physical systems like antiferromagnets or superconductors. With the aid of SFA it is possible to allow the occurrence of these phases.

When the Hamiltonian was decoupled in Eq. (2.40) into intra-cluster and inter-cluster parts, the perturbation term connecting the clusters consisted only of the hoppings between different clusters. However, there is in fact no restriction to what kind of single particle operators are included in this term. To be more specific, the Hamiltonian is invariant under the transformation

$$\begin{aligned} H_0^c(\mathbf{R}) &\rightarrow H_0^c(\mathbf{R}) + O(\mathbf{R}) \\ H_0(\mathbf{R}, \mathbf{R}') &\rightarrow H_0(\mathbf{R}, \mathbf{R}') - \delta_{\mathbf{R}, \mathbf{R}'} O(\mathbf{R}), \end{aligned} \quad (2.47)$$

where $O(\mathbf{R})$ is an arbitrary single particle term

$$O(\mathbf{R}) = \sum_{a,b} \Delta_{a,b} c_{a\mathbf{R}}^\dagger c_{b\mathbf{R}} \quad (2.48)$$

and a, b denote general quantum numbers within the cluster. This invariance can be interpreted as follows: an arbitrary single particle operator is added to the cluster Hamiltonian and subtracted perturbatively within CPT. From this follows that the lattice Hamiltonian is different from the cluster Hamiltonian as it does no longer contain this additional single particle term. However, the choice of $\Delta_{a,b}$ is now another degree of freedom and which value will improve the results physically is not obvious. The answer comes from the SFA as this virtual operator is just another variational parameter for which an optimum point of Ω , Eq. (2.46), has to be found.

The motivation to add such virtual terms is on one hand to allow the inclusion of symmetry breaking fields on the cluster level. This does not force the solution to be symmetry broken as using the variational scheme provided by the SFA, the solution with a saddle point of the grand potential Ω may be the one with vanishing virtual fields. On the other hand the inclusion of virtual operators allows to restore a thermodynamically consistent particle density which is not conserved within CPT.

In this thesis, only the chemical potential μ of the cluster is used as a variational parameter to obtain a thermodynamically consistent particle density $\langle N \rangle$ [37, 38]

$$\langle N \rangle = \sum_{i\sigma} \langle n_{i\sigma} \rangle \equiv -\frac{\delta\Omega}{\delta\mu}. \quad (2.49)$$

For the discussion of half-metallic ferromagnets it is not necessary to include a ferromagnetic field in order to obtain a ferromagnetic phase, as the symmetry can be broken already at the finite-cluster level by a proper choice of the occupation of the cluster.

Chapter 3

Correlation effects in real world materials

Half-metallic ferromagnets

In 1983, the unusual magneto-optical properties of several Heusler alloys provided the motivation to study the electronic structure of these materials and as a consequence a new class of solids was discovered, the half-metallic ferromagnets. Now after more than twenty-five years, it is not even completely clear how many materials with this property exist. This is due to the fact that there is no 'smoking gun' experiment to prove or disprove half-metallicity. The most direct way so far to access this property is spin-resolved positron annihilation, which however is costly and very time consuming. Other methods like Andreev reflection and superconducting-tunneling suffer from surface or interface effects. In addition, sample preparation is in many cases a difficult task as half-metallicity is generally sensitive to interfaces and disorder. Due to these experimental complications, electronic structure calculations continue to play an important role in finding and understanding effects in these materials.

Half-metallic ferromagnets form a quite diverse collection of materials with different chemical and physical properties as even the origin of its properties can be rather different. Just to name a few examples, half-metallic ferromagnetism was predicted for materials with structures ranging from the half and full Heusler- and zinc-blende structure to double perovskites, with chemical compositions including oxides, sulfides, ruthenates and was even predicted for low-dimensional organic structures.

Within the framework of this thesis a number of half-metallic and strongly correlated systems were investigated and the gathered results appeared in a number of publications (denoted as P1-P8); for a complete list with references see also App. B.

It is the aim of this chapter to present these results, so to gain insight into a number of very different half-metallic ferromagnets like CrO_2 , which has a comparatively simple structure, to NiMnSb , where the non-local correlations between both

transition metals play an important role.

Another motivation to study half-metallic ferromagnets is connected with the aim to use them in giant magnetoresistance and tunnel magnetoresistance devices. This started big interest to build and understand heterostructures containing half-metallic ferromagnets. With a similar intended use, calculations for large heterostructures of half-metallic CrAs on a semiconductor substrate are also presented to gain insight into the physics of these systems.

Strongly correlated systems

While for the presented half-metallic compounds the magnitude of the Coulomb-interaction is in the intermediate range, we applied the LDA+VCA approach also to a truly strongly correlated material, namely titanium nitride (TiN).

When prepared as thin film, this compound shows peculiar properties like a disorder driven transition from a superconductor to an insulating phase in which superconducting correlations persist. Our calculations performed for stoichiometric TiN give an interesting insight into this material; not only we find that this material is close to a Mott-metal insulator transition, but also that non-local correlations play a significant role in this compound.

3.1 Half-metallicity in CrO₂

3.1.1 Introduction

Transition metal oxides exhibit a rich collection of interesting and intriguing properties, which can be used for a wide variety of applications including quantum computing, ultra high-density magnetic data storage and more recently spintronic applications [22]. The transition metal oxide CrO₂ besides the full and semi-Heuslers, the most prominent and perhaps the simplest half-metallic ferromagnet known so far. It is currently an important material in industry and widely used in magnetic storage devices. CrO₂ is an outstanding example in which magnetism and correlation effects associated with electron-electron interaction determine the essential finite temperature properties such as polarization and magnetization [P1]. New effects resulting from an interplay of various phenomena attracted an increasing attention to motivate the investigation of the electronic properties of CrO₂ by a multitude of experimental [39, 40, 41, 42, 43, 44, 45] and theoretical approaches [46, 47, 48, 49]. Despite the large number of investigations, the understanding of the correlated electronic structure of CrO₂ is still not complete.

The ferromagnetic phase of CrO₂ is stable far above room temperature which makes this compound suitable for real world applications. Its half-metallic character was predicted by Schwarz [50], and a high spin polarization of more than 90% was found in point contact measurements at superconductor metal interfaces [51, 52]. This makes this material an interesting candidate for spintronic applications. However, this very large spin polarization, measured at 1.6K, is still lower than the ideal 100%. Even at low temperatures magnons can be excited, which can suppress the ideal spin polarization. Previously, it was shown for a large number of half-metals in the semi-Heusler and zinc-blende structure that a qualitative description of the electron-magnon interaction captured by the Dynamical-Mean Field Theory (DMFT), leads to the existence of non-quasiparticle states (NQP) [7, 53, 54, 55],[P1],[P3]. These states cause depolarization and their influence is dominant in comparison to other effects such as spin-orbit interaction or non-collinearity [54]. In addition, in the complicated real space structure of the half-metallic ferromagnets, effects like lattice imperfections, spin disorder or phonons may also affect depolarization. Nevertheless, even in perfect crystals, NQP-states are expected to play an important role.

3.1.2 Electronic structure

CrO₂ is a ferromagnetic metal with a Curie temperature of 385-400K [56]. The electrical resistivity has a metallic temperature dependence and shows anomalies around T_c indicating scattering of electrons by fluctuating magnetic moments at finite tem-

peratures. At low temperatures, optical spectroscopy (conducted at 10K [43]) show a saturation magnetization of $1.92\mu_B$ which is close to the ideal value of $2\mu_B$.

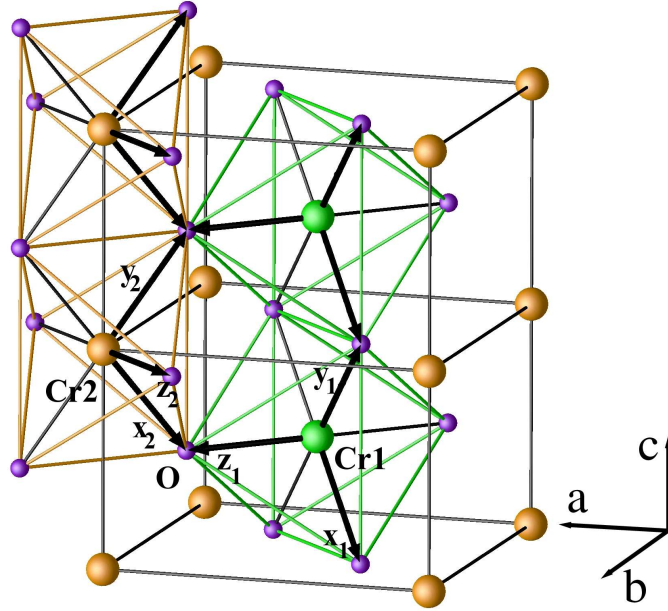


Figure 3.1: Rutile structure of CrO_2 : Cr1 (green) and Cr2 (orange) denote nonequivalent Cr-atoms (see text). Each Cr-atom is octahedrally coordinated by oxygen atoms (purple). x_i, y_i, z_i denote the local coordinate system used within NMTO.

The lattice of CrO_2 , as shown in Fig. 3.1, consists of a rutile (tetragonal) structure with $a = 4.421\text{\AA}$ and $c = 2.916\text{\AA}$ ($c/a = 0.65958\text{\AA}$). The Cr-ions order in a body-centered tetragonal lattice and each Cr-site is surrounded by octahedra formed by oxygen-atoms. Cr^{4+} has a closed shell Argon core and in addition two $3d$ -electrons. As the Cr-ions are sitting in the center of CrO_6 -octahedra and experience crystal field splitting. Therefore, the Cr($3d$)-orbitals are split into a Cr(t_{2g})-triplet and an excited Cr(e_g)-doublet. The tetragonal symmetry causes a distortion of the oxygen-octahedra, which partially lifts the degeneracy of the t_{2g} -orbitals into a d_{xy} ground-state and d_{yz-zx} and d_{yz+zx} excited states, where a local coordinate system is used for each octahedron (see Fig. 3.1 and Fig. 3.2).

For these two Cr(d) electrons a double exchange mechanism was proposed [57], in which due to strong Hund's rule coupling, supported by the distortion of the oxygen octahedra, the electron in the Cr(d_{xy})-orbital is localized, while the electron in the d_{yz} - and d_{xz} -orbitals has itinerant character.

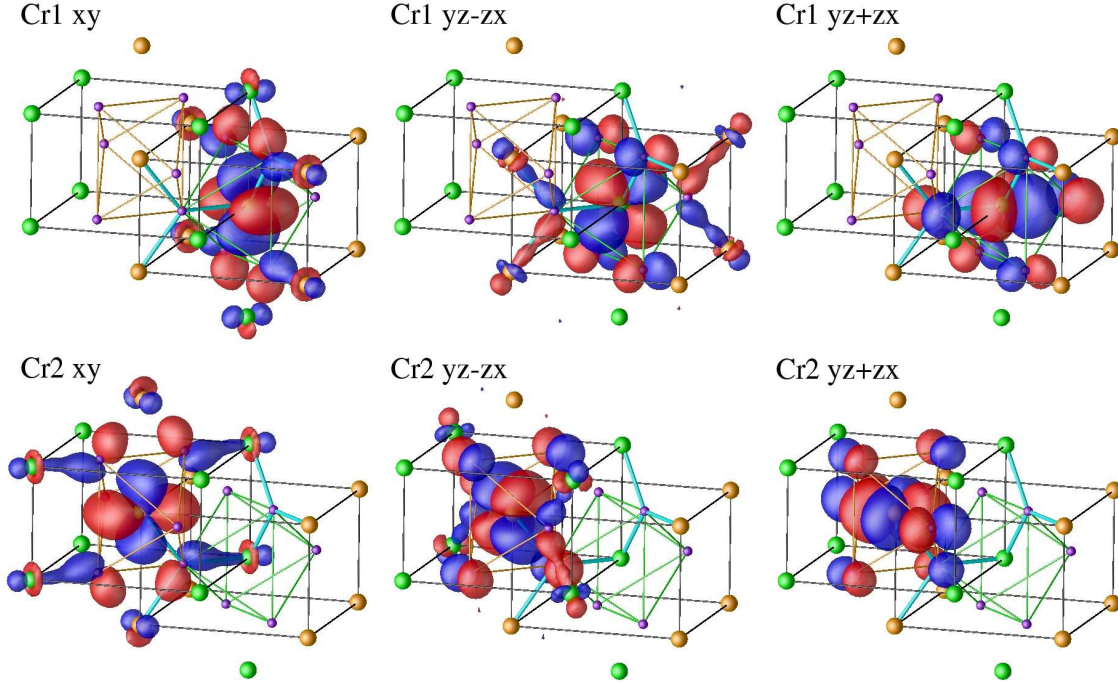


Figure 3.2: Real space distribution of the $\text{Cr}(t_{2g})$ Wannier-orbitals: Cr1 is shown in green, Cr2 in orange, oxygen in purple. The upper panel shows the orbitals for Cr1, the lower for Cr2.

With only two $3d$ -electrons we can neglect the energetically higher lying e_g -states and focus solely on the t_{2g} -triplet by downfolding all other orbitals (for more specific details concerning downfolding see chapter 2.2.1).

3.1.3 Model and realistic parameters for the Coulomb interaction

To explore correlation effects CrO_2 , we adopt a spin-rotational invariant Hubbard-Hamiltonian restricted to $\text{Cr}(t_{2g})$ -orbitals only. Realistic parameters are obtained via NMTO, as described in chapter 2.2. In that chapter we also show in Fig. 2.2 the full band structure of CrO_2 and provide a direct comparison to the $\text{Cr}(t_{2g})$ bands obtained from downfolding.

For the interaction part of the Hamiltonian we use accordingly the t_{2g} -subset of the full U -matrix as described as Eq. (2.24) on page 34 in chapter 2.3.2. For this subset, the Coulomb-interaction between the $\text{Cr}(t_{2g})$ electrons is independent of the orbital indices of the involved electrons.

The values of the Coulomb-interaction (U) and Hund's exchange (J) parameters

acting between Cr(t_{2g})-electrons are evaluated from first principles by means of a constrained LSDA method [58]. While this method is not very accurate, and may produce slightly different values depending on its exact implementation, it is quite clear that for CrO₂ the interaction parameters are not too strong. From this calculation one finds that an appropriate choice is $U \approx 3$ eV and $J \approx 0.9$ eV.

As reference system for the LDA+VCA calculation we use a cluster of eight sites, shown in Fig. 3.3. The cluster consists of four of each of the nonequivalent Cr-atoms. Every Cr-site has the t_{2g} -subset of the full- d manifold. For this choice of the cluster, finite size effects were investigated and found to be negligible (see Appendix D). The variational procedure includes only the chemical potential as discussed in connection with Eq. (2.49) in chapter 2.4. Notice that the particle density in the physical system is in general different from the one of the reference system [38]; the former turns out to be slightly doped with $n = 1.83$ electrons per unit cell.

Quite generally, multi-orbital strongly-correlated systems show a competition between different magnetic and orbital-ordered phases. In order to check that the ferromagnetic phase is the one with the lowest energy, we have compared its grand-canonical potential, Eq. (2.46), with the one of different magnetic phases containing mixed antiferromagnetic and ferromagnetic components in different directions. Moreover, for the chosen parameters we confirm that the ferromagnetic state is more favorable energetically with respect to all antiferromagnetic states we have considered, as well as to the paramagnetic state.

3.1.4 Results - Density of states

In order to analyze the role of the different Cr(t_{2g})-orbitals, we present in Fig. 3.4 the orbital and spin-resolved density of states (DOS).

A remarkable result of the LDA+VCA calculation is the presence of a significant amount of states at the Fermi-energy originating from the putatively localized d_{xy} -orbital. More specifically, we obtain that this orbital is not completely half-filled, its occupation being $n_{xy} \approx 0.87$, while for the other two orbitals we find $n_{yz+zx} \approx 0.49$, and $n_{yz-zx} \approx 0.45$. These values for the occupations are also confirmed by LSDA+DMFT calculations [P1]. As consequence of this significant amount of spectral weight at Fermi-energy, the d_{xy} -orbital consists of quite itinerant electrons, though with a large effective mass rather than of localized moments.

However, our findings are in contrast to previous DMFT [59, 60] calculations, in which the Fermi-energy only touches the tail of the d_{xy} DOS, which was consequently considered to be localized moments. This is probably due to the large value of the interaction parameter $U \approx 5$ eV used in these calculations. We believe that the smaller value of $U \approx 3$ eV used here is more appropriate, as it is obtained from first principles.

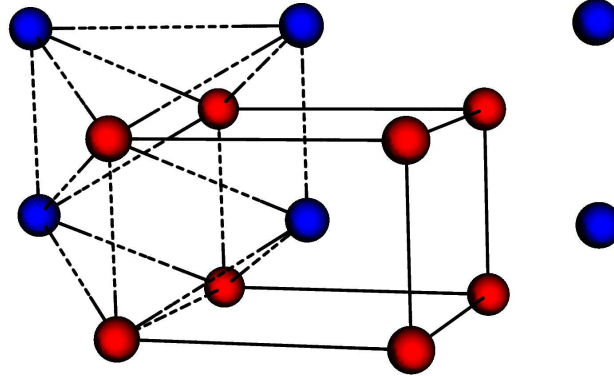


Figure 3.3: The reference system (atoms connected by dashed lines) used in the variational calculation; red and blue denote the unequal Cr-atoms Cr1 and Cr2, respectively. The solid line shows the tetragonal unit cell.

Non-quasiparticle states In the minority spin channel, NQP-states are clearly visible predominantly in the $d_{yz\pm zx}$ orbitals just above the Fermi-energy. The physical origin of NQP states is connected with the “spin-polaron” processes [61, 62]: the spin-down low-energy electron excitations, which are forbidden for half-metallic ferromagnets in the one-particle picture, turn out to be possible as superpositions of spin-up electron excitations and virtual magnons [61, 62]. An uniform superposition forms a state with the same total spin quantum number $S = (N + 1)/2$ (N is the particle number in the ground state) as the low-energy spin-up state, but with one “spin-flip”, i. e. with z -component $S_z = S - 1$. If the Hamiltonian is spin-rotational invariant, as is the one used here, this state with one additional spin-down particle must have the same energy as the low-energy state with one additional spin-up particle, although its weight is reduced by a factor $1/N$.

We stress that spin-rotation invariance is crucial in order to obtain low-energy NQP-states. For this reason, methods neglecting spin-flip processes in the interacting part of the Hamiltonian are not expected to provide a correct description of NQP-states. Similar NQP-states are obtained in the fully self-consistent LSDA+DMFT calculation [P1].

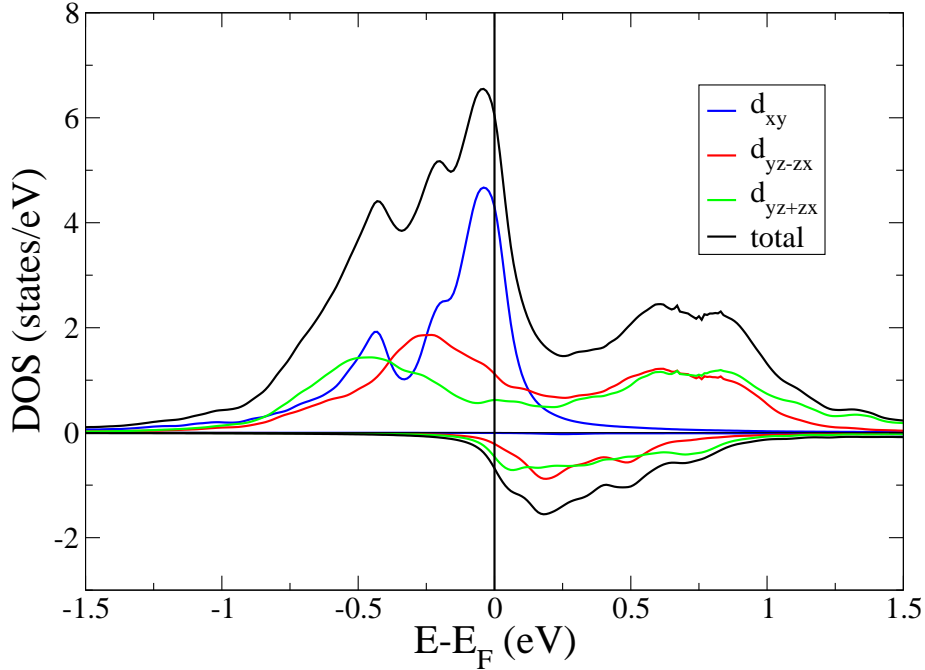


Figure 3.4: Cr(t_{2g}) orbital-resolved density of states in the ferromagnetic state, calculated within the LDA+VCA approach for $U=3\text{eV}$, and $J=0.9\text{eV}$, using the eight site cluster shown in Fig. 3.3.

3.1.5 Comparison to other theoretical results and to experimental data

To allow a comparison from the LDA+VCA results to results from density functional theory, Fig. 3.5 shows the density of states obtained from LSDA+U for $U=3\text{eV}$, and $J=0.9\text{eV}$. A strong hybridization of O(p) and Cr(d) states is present and the results indicate that outside an energy window of -1.5eV to 2.5eV O(p) states become important. Further, the results show a very large gap of about 2eV in the minority spin and a gap-like situation for the majority spin at Fermi-energy. In comparison to the LSDA-results in Fig. 3.6, the minority spin gap seen in the LSDA+U results is enlarged by about 0.5eV . The DOS of the majority spin is very similar and Fermi-energy sits also in the LSDA-results within a pseudo-gap. The obtained magnetic moment for both LSDA and LSDA+U calculations is integer $2.0 \mu_B$ and spin polarization is ideal 100% as shown in Fig. 3.8.

Fig. 3.6 shows LSDA and LDA+DMFT-results for comparison. Notably, the LSDA Fermi-level intersects the majority-spin bands near a local minimum and lies in the band gap of the minority spin states. Finite temperatures and correlation effects

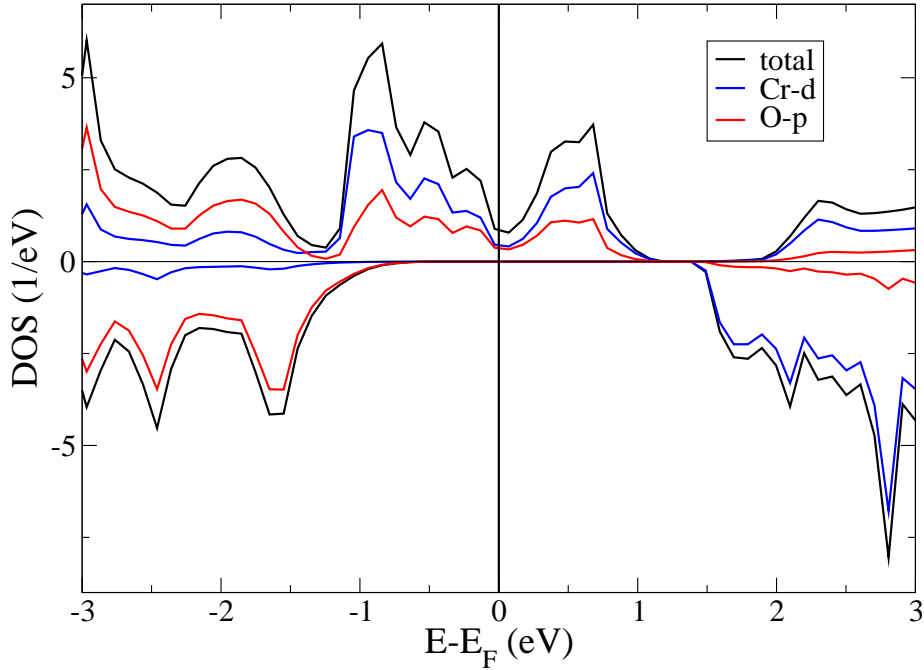


Figure 3.5: Density of states calculated for CrO_2 using LSDA+U for $U=3\text{eV}$, and $J=0.9\text{eV}$. Total DOS is shown as black line, blue denotes Cr(d) states and in addition O- p states are shown in red.

close this minimum around the Fermi-level, as can be seen from the LDA+DMFT results in Fig. 3.6. For both spin channels, the DOS is shifted uniformly to lower energies in the energy range of -2 and -6eV, where predominantly the O(p) bands are situated. This is due to the fact that correlated Cr(d) bands affect the O(p) states through the Cr(d)-O(p) hybridisation, so that the latter contribute actively to the mechanism of the ferromagnetic ground state. The results from the LDA+DMFT calculation confirm the existence of minority spin states just above the Fermi-energy, as observed in the DOS of LDA+VCA calculation.

In Fig. 3.7 we compare our results to quite recent experimental data including Bremsstrahlung isochromat spectroscopy (BIS) and ultraviolet photoemission (UPS) experiments conducted by Tsujioka et al [39] and to O($1s$) x-ray absorption (XAS) measurements done by Huang et al [45].

The inset of Fig. 3.7 shows a comparison of the BIS-data with the results from LDA+VCA where the two spin orientations were summed to yield non-spin polarized results. While the results from LDA+VCA agree quite well with the BIS-data for energies lower than about 0.6eV, a significant deviation occurs for higher energies. This can be explained by the onset of Cr($3d$)-O(p) hybridized states that are seen in

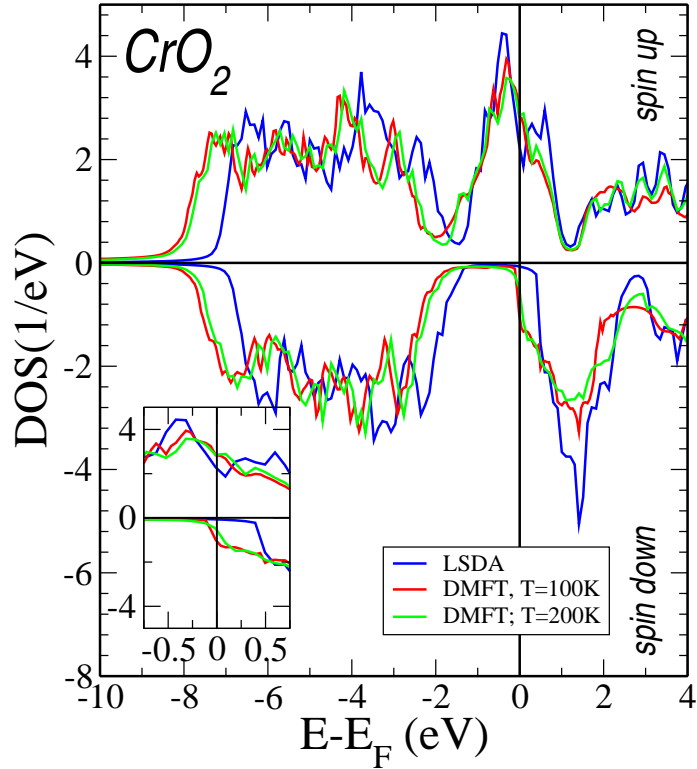


Figure 3.6: DOS for CrO_2 obtained from LSDA (blue line) and from LDA+DMFT for $T = 100\text{K}$ (red line) and for $T = 200\text{K}$ (green line). The LSDA-result is considered the zero temperature limit for the LDA+DMFT calculations [P1]. The inset shows in detail the region close to Fermi-energy.

the XAS-measurements for energies above 0.6eV (see Fig. 3.7).

Comparing the experimental data to results from other methods, it is interesting to note that the minority spin density of states obtained from LSDA and LSDA+U, as shown in Fig. 3.6 and 3.5, do not show any states for energies up to 0.5eV and 1.5eV , respectively.

At the Fermi-energy the experimental data from UPS do not show any significant spectral weight and experimentally the main Cr($3d$) spectral weight is located at about -1.2eV . This is in contrast to our results and to results from LDA+DMFT, which show large spectral weight at the Fermi-energy.

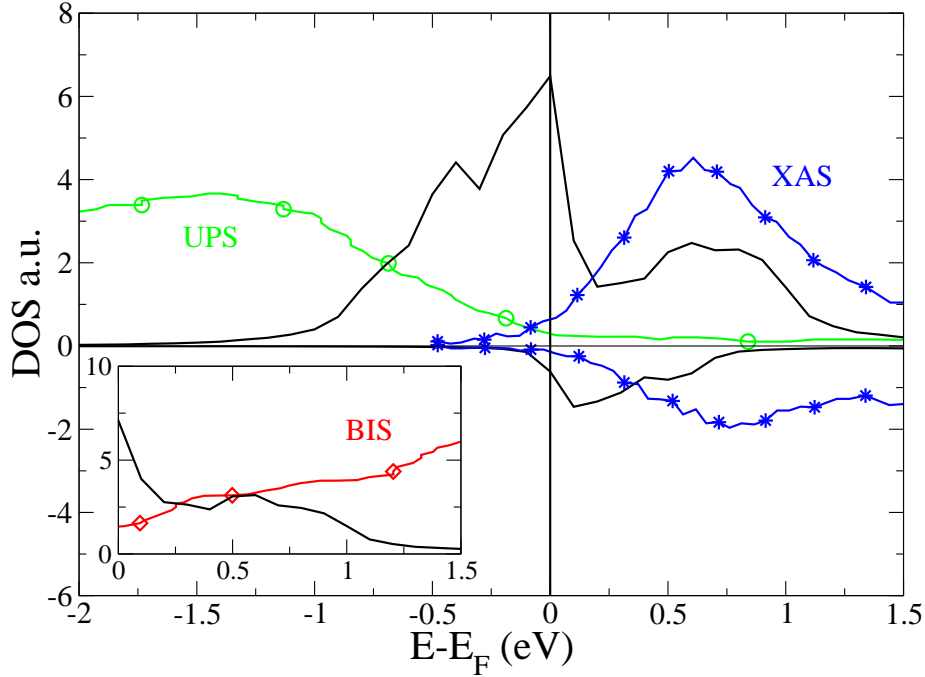


Figure 3.7: Comparison of the results obtained from LDA+VCA (solid black line) with ultraviolet photoemission (green line, decorated with circles) and data from O(1s) x-ray absorption measurements performed on the conduction band of CrO₂ (blue line, decorated with stars). The inset shows non-spin polarized data from Bremsstrahlung isochromat spectroscopy (red line, decorated with diamonds) in comparison to the results from LDA+VCA (black, solid line). For the inset, the LDA+VCA density of states of both spin orientations is added to yield non-spin polarized results.

Further we find that the many-body effects discussed above, especially the formation of NQP-states, contribute significantly to the energy dependence of the spin polarization $P(E)$, defined as

$$P(E) = \frac{N_{\uparrow}(E) - N_{\downarrow}(E)}{N_{\uparrow}(E) + N_{\downarrow}(E)}, \quad (3.1)$$

where $N(E)$ is the density of states of majority spin- \uparrow or minority spin- \downarrow electrons.

Fig. 3.8 shows a comparison between the measured [45] and computed polarization for the different ab-initio many-body calculations discussed here. It is important to note that the position of the Fermi-energy of the experimental data shown here is different by about two data points (corresponds to about 0.1eV) to the one presented

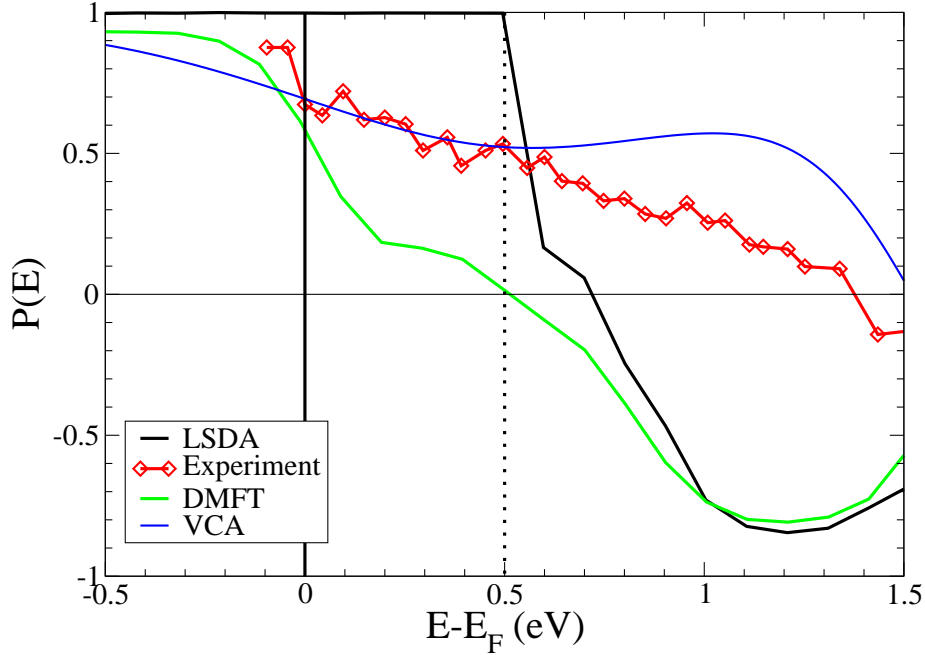


Figure 3.8: Energy dependence of the spin polarization $P(E)$, as defined in Eq. 3.1, found in x-ray absorption experiments (shown as red decorated, solid line, concerning exact position of the Fermi-energy see also text) in comparison to results from different theoretical calculations: LSDA (black), LDA+DMFT (green), LDA+VCA (blue). A Gaussian broadening of 0.4 eV (corresponding to the experimental resolution) has been added to the theoretical results.

in the original publication [45]. While this difference is small, spin polarization at Fermi-energy is significantly affected and no longer larger than 90% as reported in the original publication. The reason for this difference is not clear; however, as the data presented here was obtained directly from one of the authors, we consider the shown data to be more trustfull.

Due to the tails of the NQP-states, the spin polarization calculated with LDA+VCA is consistently less than 100% even at the Fermi level. The result obtained from LSDA overestimates the spin polarization at Fermi-energy as it is not able to capture non-quasiparticle states due to neglect of local correlation effects. On the other hand, both LDA+VCA and LDA+DMFT results show excellent agreement with the experiment at the Fermi-level. At an energy of about 0.5 eV polarization is reduced by about 50%, and up to this energy the agreement of the LDA+VCA calculation is particularly good, while the result from DMFT overestimates significantly depolarisation effects away from Fermi-energy. The deviation from experiment seen in the

LDA+VCA results for energies at ≈ 1 eV is probably due to the neglect of the Cr(e_g) orbitals which are gaining importance at higher energies.

3.1.6 Conclusion

Summarizing, the results obtained from LDA+VCA show that correlation effects play a significant role in CrO₂, despite the fact that the value for the Coulomb interaction that we use in the calculations is rather intermediate. As the values used here were derived ab-initio by the use of constrained LDA, we believe that these intermediate values are more appropriate.

Consequently, we find that many-body effects considerably change the mean-field LSDA and LSDA+U picture. Within these methods the single occupancy of the Cr(d_{xy}) orbital is determined by the exchange and crystal field splitting, whereas the inclusion of short ranged correlations within LDA+VCA induces a ferromagnetic state with an itinerant-type Cr(d_{xy}) orbital. Although electrons in the Cr(d_{xy}) orbital have a large effective mass, they are not purely localized. This finding is in contrast to previous results [47, 63, 59, 60], which, however, were obtained by using a larger value for the Coulomb-repulsion.

With respect to the half-metallic gap, we find that correlation effects lead to the appearance of non-quasiparticle states in the minority spin channel at Fermi-energy. These states reduce the large gap that is seen in LSDA and LSDA+U-results and cause depolarization for energies close to Fermi-energy. Therefore, they are crucial for a correct description of the energy dependance of the spin polarization as the comparison to experimental data shows.

A more complete quantitative analysis of depolarisation would, however, require the description of additional effects, such as, e. g., disorder or phonons, as these processes are also expected to contribute to spin depolarization.

3.2 The prototype half-metallic ferromagnet: NiMnSb

3.2.1 Introduction

More than twenty years ago *de Groot et al.* [64] carried out electronic structure calculations for the half-Heusler compound NiMnSb which showed peculiar magnetic features leading to the discovery of a by then new class of materials, the half-metallic ferromagnets. While within this thesis already a different half-metallic ferromagnet was studied, namely CrO₂, NiMnSb is not only interesting from an historical point of view. In comparison to CrO₂ the electronic structure of NiMnSb is complicated by the fact that two different transition metals are present. Both of them are important to determine the electronic properties of this material, as will be discussed in detail.

Despite the fact that high quality NiMnSb films have been successfully grown, they were not found to reproduce the half-metallic character of the bulk suggested by spin-polarized positron-annihilation [65, 66]. Values of spin polarization were reported between 40% in spin-resolved photoemission measurements [3] up to $58 \pm 2.3\%$ by superconducting point contact measurements at low temperatures [51] (see also Refs. [67, 68]). The discrepancy between theoretical calculations [64] and the above mentioned experimental facts were attributed to surface and interface effects. Consequently, different surface and interfaces of NiMnSb were theoretically investigated by *de Wijs* and *de Groot* [69], which demonstrated that half-metallicity can be preserved at the surface and/or interface by suitable reconstruction. The theoretical situation is complicated by the fact that the spin polarisation (or, more precisely the tunneling magnetoresistance) displays a substantial uniaxial anisotropy in epitaxial grown NiMnSb, as was demonstrated previously [70].

Recently, finite-temperature correlation effects were addressed in several half-metals [71, 7, 55, 72, 73],[P1]. For NiMnSb, a Local Density Approximation plus Dynamical Mean Field Theory calculation (LDA+DMFT) [7] showed the appearance of so-called non-quasiparticle (NQP) states. These states originate from spin-polaron processes, whereby the spin-down low-energy electron excitations, which are forbidden for half-metallic ferromagnets in the one-particle picture, turn out to be possible as superpositions of spin-up electron excitations and virtual magnons [61, 74, 62, 71]. Here, we extend this study by adopting the Variational Cluster Approach (VCA), which includes correlations beyond the locality captured by DMFT. In addition, the VCA is based on exact diagonalisation, which is more appropriate than the diagrammatic SPTF method [75, 76, 77, 78] adopted in Ref. [7] to solve the impurity problem.

In App. E, we investigate the spin polarization in NiMnSb taking into account only the *Mn-d* orbital basis set. The results of that calculation show that the *Mn-d*-only basis set is not sufficient to appropriately describe the low energy spectrum

of NiMnSb around the Fermi-level. For this reason, in the present work we adopt a multi-orbital Hubbard-type Hamiltonian written in a basis that includes all ten orbitals of Mn and $Ni-d$ states. Our present calculation confirms that the inclusion of the latter is essential for a proper description of ferromagnetic properties and of the minority spin gap in NiMnSb.

Our results support the existence of states within the minority spin gap in agreement with previous LDA+DMFT calculations [7, 71]. In addition, they indicate that these so-called nonquasiparticle states indeed have a vanishing quasiparticle weight at the Fermi energy. At the same time, our results predict a correlation-induced spectral weight transfer for the majority spin states. The combination of these two effects yields a polarization whose energy dependence is in qualitative agreement with experiments. Further, our calculations emphasize the importance of non-local correlation effects. In particular, we show that the imaginary part of the self energy for nearest-neighbor Ni and Mn sites is larger than the local one in the interesting region just above the Fermi energy for minority-spin states. The diagonal self-energy is in turn similar to the one obtained from the local DMFT construction discussed previously [7, 71]. These calculations lead to the conclusion that even in the presence of medium-size interactions, non-local electron correlations significantly affect the spin polarisation in half-metals.

3.2.2 Electronic structure calculations for NiMnSb

The intermetallic compound *NiMnSb* crystallizes in the cubic structure of *MgAgAs* type ($C1_b$) with the *fcc* Bravais lattice (space group $F\bar{4}3m = T_d^2$). This structure can be described as three interpenetrating *fcc* lattices of *Ni*, *Mn* and *Sb* with the lattice parameter $a = 11.20a_0$ ($a_0 =$ Bohr radius), respectively. The *Ni* and *Sb* sublattices are shifted relative to the *Mn* sublattice by a quarter of the [111] diagonal in opposite directions, see also Fig. 3.9.

The important aspects [64, 79, 80, 81, 82, 71] which determine the behavior of electrons near the Fermi-level, as well as the half-metallic properties are the interplay between the crystal structure, the valence electron count, the covalent bonding, and the large exchange splitting of *Mn-d* electrons. For the minority spin gap opening, not only the *Mn-d-Sb-p* interactions, but also *Mn-d-Ni-d* interactions have to be taken into account. In addition, the loss of inversion symmetry produced by the $C1_b$ structure (the symmetry lowering from O_h in the $L2_1$ structure to T_d in the $C1_b$ structure) are important for these effects. The existence of *sp*-valent *Sb* is crucial to provide stability to this compound.

The crystal structure is shown in Fig. 3.9, where the positions occupied by atoms are represented by spheres. For illustrative purposes, in Fig. 3.9 the radii of the spheres were chosen arbitrarily. The actual muffin-tin radii used in the calculations are $R_{MT}^{Ni} = 2.584$; $R_{MT}^{Mn} = 2.840$; $R_{MT}^{Sb} = 2.981$ and $R_{MT}^E = 2.583$ (atomic units) for

the vacant position situated in $(1/4, 1/4, 1/4)$. The LMTO-ASA basis used for the self-consistent calculations contains the spd -partial waves for Mn and Ni , the $sp(df)$ -partial waves for Sb and $s(pd)$ -partial waves for the empty sphere E . (l) means that the l -partial waves are downfolded within the selfconsistent calculations.

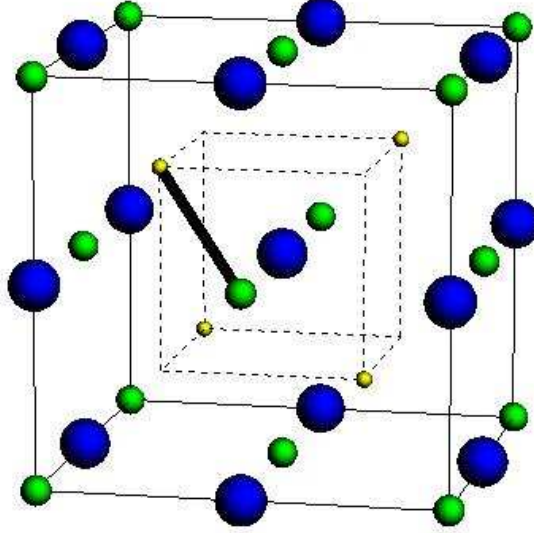


Figure 3.9: The conventional unit cell for the semi-Heusler $NiMnSb$ compound: Sb (large, blue spheres) and Mn (medium, green spheres) sit on the same faces of the large cube (shown with thin, solid lines), Ni (small, yellow spheres) forms a separate (small) cube drawn using dashed lines. In addition, the atoms belonging to the reference system of the VCA calculation are connected by a thick solid line. Sb orbitals are downfolded and, therefore, not included directly in the model calculation.

3.2.3 Ab-initio construction of the model Hamiltonian

In order to construct the effective low-energy Hamiltonian to use in our VCA calculation, we employed the Nth order muffin-tin-orbitals scheme as outlined in chapter 2.2.

From the discussion in Ref. [2] it follows that not only the $Mn-d-Sb-p$, but also $Mn-d-Ni-d$ interactions are required to open a gap in the minority spin channel: the minority occupied bonding states are mainly of $Ni-d$ character, while the unoccupied anti-bonding states are mainly of $Mn-d$ character. Therefore, in the present work we consider an enlarged NMTO-basis consisting of $Ni-$ and $Mn-d$ orbitals which span an energy window of about $\pm 3eV$ around the Fermi energy.

For the interaction part of the Hamiltonian we used, accordingly, the full U -matrix as described in Eq. (2.22) in chapter 2.3.2. We use the same effective Slater parameters for Mn and Ni , i. e. $F^0 = 1.26\text{eV}$, $F^2 = 5.58\text{eV}$ and $F^4 = 3.49\text{eV}$ (where the ratio of F^4/F^2 is fixed to $F^4/F^2 = 0.625$, see chapter 2.3), which give an intra-orbital Coulomb-interaction of $U = U_{mmmm} = 2.0\text{eV}$. Therefore, in our full- d model we unavoidably have orbital dependent Hund's rule couplings $J_{mm'mm'}$. In our work, the orbital-averaged value \bar{J} of the $J_{mm'mm'}$, is equal to $\bar{J} = 0.65\text{eV}$. In addition, we performed calculations for $U = 2.5\text{eV}$ and $U = 3\text{eV}$ with $\bar{J} = 0.78\text{eV}$, and verified that our results do not depend significantly on the chosen U and \bar{J} -values. This range of values corresponds to the one used in previous works [7, 53, 54, 55].

Following the discussion in chapter 2.3.3, the on-site energies calculated in NMTO already contain effects from the Coulomb interaction at the LDA mean-field level.

Therefore, one has to subtract so-called double counting corrections that are especially important for materials where many transition metals are present. Different schemes have been suggested and two of these, namely the around mean field scheme and the fully localized limit scheme, are discussed in chapter 2.3.3.

In order to investigate the influence of the used double-counting correction, we perform calculations for the different schemes. From these tests that are presented in App. F, we find that the spectral function obtained from LDA+VCA remains unchanged for energies within $E_F \pm 1\text{eV}$, while for energies outside this range (from $\pm 1\text{eV}$ to about $\pm 3\text{eV}$) a redistribution of Mn - and Ni - states is obtained. In the following for all calculations the AMF-DCC scheme is used.

As a reference system for the LDA+VCA calculation we use a cluster of two sites, representing one Mn -atom and one Ni -atom (see Fig. 3.9), each having the full- d manifold of five orbitals. Since we have to consider all five orbitals for each atom, it is very difficult to use larger clusters, which have to be exactly diagonalized many times in combination with the variational procedure.

3.2.4 Results - Density of states

In order to study the influence of correlations on the half-metallic gap, we first display the spin-resolved local density of states in Fig. 3.10. Here, we present a comparison of the results obtained from LSDA with the results from our LDA+VCA calculation. The LSDA-DOS is mainly characterized by a large exchange splitting (about 3eV) of the Mn - d states, leading to large spin moments on the Mn -site ($3.72\mu_B$). A small induced ferromagnetic moment is present on Ni ($0.29\mu_B$), while the Sb moment ($0.06\mu_B$) is anti-parallel to the Mn moment. Overall, the calculated moments are in very good agreement with previous ab-initio results [64, 71, 80, 2, 82].

The existence of large localized Mn moments of about $3.78\mu_B$ has been verified experimentally by neutron diffraction [83] as well as by the sum rule of the x-ray

magnetic circular dichroism spectra [84]. These two experiments also confirm the magnitude of the LSDA-computed moments for *Ni* and *Sb*. The gap in the minority spin channel is about 0.5eV wide and the total magnetic moment has an integer value of $4\mu_B$. Note, that in Fig. 3.10 in LSDA the minority occupied bonding states are mainly of *Ni-d* character, while unoccupied anti-bonding states are mainly of *Mn-d* character. It was pointed out [64] that the opening of a gap is assisted by *Sb* through the symmetry lowering with the consequence that the distinction between *Mn-t_{2g}* and *Sb-p* character of the electrons is lost.

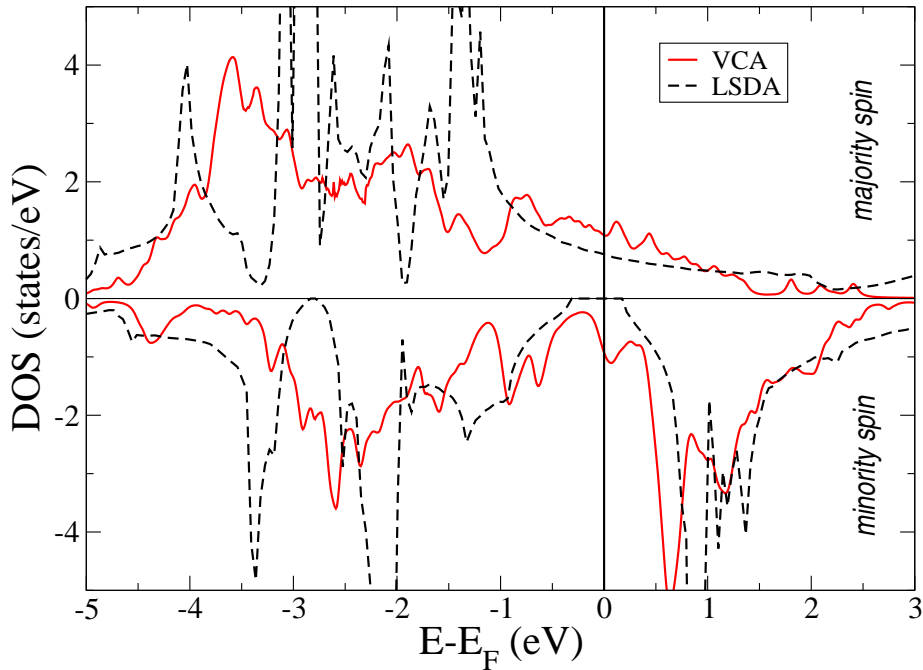


Figure 3.10: Density of states for NiMnSb obtained from LDA+VCA (red, solid line) for values of the average Coulomb and exchange parameters $U = 2\text{eV}$ and $\bar{J} = 0.65\text{eV}$ for both Mn and Ni atoms. in comparison to results obtained from LSDA (black, dashed line).

Concerning the LDA+VCA results, we find a total magnetic moment of $3.7\mu_B$, which is in reasonable agreement with experimental values [83, 84]. In direct comparison to LSDA, our results show that correlation effects do not affect too strongly the general picture of the minority spin DOS for energies which are more than 0.5 eV away from the Fermi energy. In the range $0.5\text{eV} \lesssim E - E_F \lesssim 3\text{eV}$, unoccupied *Mn*-states are visible in the minority spin sector, similarly to LSDA. However, these states are shifted to lower energies due to a slight reduction of the *Mn*-exchange splitting generated by the many-body correlations.

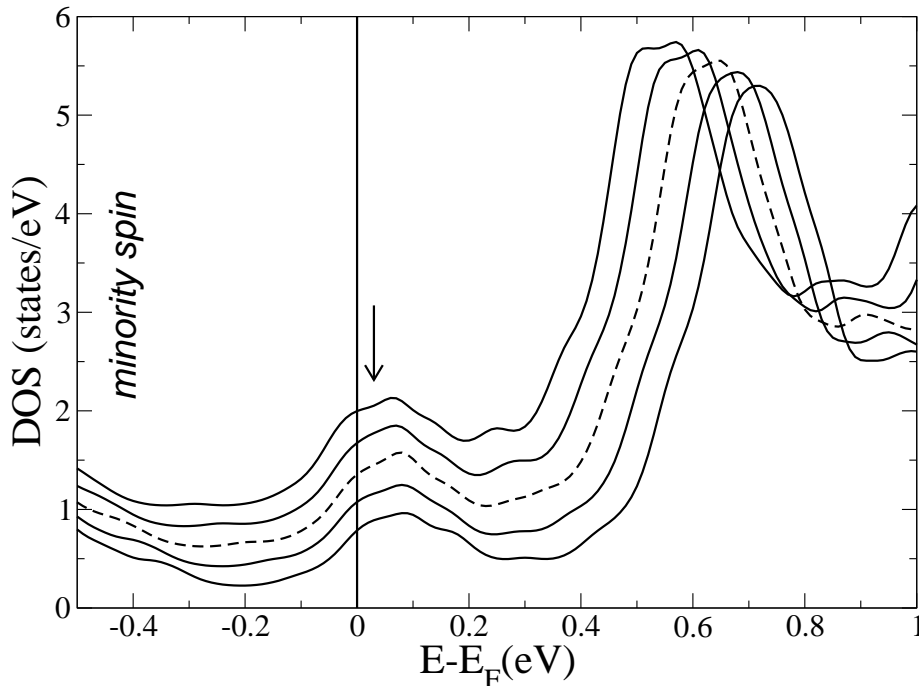


Figure 3.11: Density of states for the minority spin channel of NiMnSb using $U = 2$ and $\bar{J} = 0.65\text{eV}$, calculated for different values of the chemical potential. The NQP-states (marked with an arrow) stay pinned at the Fermi-energy independently of the chosen value of the chemical potential. The dashed line shows the reference result for the correct occupation of 14 electrons per unitcell.

Just above the Fermi-level, NQP-states are present, with a peak around the energy of 0.06eV . It is important to note that these states were also obtained in previous calculations using a LDA+DMFT many-body approach [7] at finite temperatures. In comparison to the DMFT description, the non-local correlations captured by VCA enhance the spectral weight of the NQP-states and slightly shift their position.

It is interesting to note that according to the presented LDA+VCA results, Fig. 3.11 and the previous LSDA+DMFT calculations the position of the NQP states are not significantly changed being pinned in the close vicinity of the Fermi-level.

We argue that the spectral-weight enhancement of the NQP-states is caused by non-local contributions to the imaginary-part of the self-energy which, as discussed in Sec. 3.2.6 below, turn out to be larger than local contributions in the relevant energy range. As a matter of fact, the density of NQP-states is proportional to the imaginary part of the self-energy, as discussed in Ref. [71, 61, 62].

Comparing our results with previous DMFT calculations, [7] one can conclude that, although the local DMFT description predicts a weaker spectral weight for

NQP-states, it is still sufficient to detect their existence. The spectral weight of NQP-states is large enough, so that we expect them to be well pronounced in corresponding experimental data. While model calculations for single-band Hamiltonians [71] suggest that NQP-states should only touch the Fermi-level with zero weight at $T = 0K$, in our VCA calculation they maintain a finite weight at the Fermi-level, thus leading to a reduction of spin polarisation, even at $T = 0K$.

In the LSDA-results, the bonding states below the Fermi-level have dominant *Ni-d* character and are responsible for the gap formation. While these states form a single peak at $-1.5eV$ in LSDA, the LDA+VCA-results show a splitting into two peaks centered around $-1eV$. One of these peaks is pushed closer to the Fermi-level, while the other one is shifted to higher energies. The latter correlation effect is also seen in previous LSDA+DMFT results [7].

A significantly stronger effect caused by many-body correlations is visible in the majority-spin channel (see Fig. 3.10). Here we discuss the behaviour in the same energy range within $\pm 3eV$ around the Fermi-level, since this is the energy window spanned by our NMTO basis. The LSDA density of states in this energy range is determined mainly by the covalent *Ni-Mn-d* hybridization, and by the large exchange splitting of *Mn-d* electrons [64, 71, 2]. At the Fermi-level and above a reduced density of states is present.

The density of states obtained from the LDA+VCA calculation shows a very strong spectral redistribution for the majority spin electrons: the LSDA peak situated around $-3eV$ is lowered in energy while in the energy range between $-2eV$ and E_F , a spectral-weight transfer towards the Fermi-level takes place. In particular, the large LSDA-peak at $-1.5eV$ is shifted to about $-1eV$, which results in a significant contribution to the states at the Fermi-level. Just above the Fermi-level, at energies where NQP states are formed in the minority-spin channel, a resonance peak is present in the density of states of the majority-spin electrons.

A further maximum of the density of states is present at $0.5eV$. The meaning of this maximum will become clear in the Sec. 3.2.5 where the \mathbf{k} -resolved spectral functions are discussed. In contrast to our VCA calculation, DMFT results [7] do not change significantly the picture for the majority-spin states. Although the LDA+DMFT density of states shows a similar reduction of spectral weight for the peak at $-2eV$, its position remains unchanged. The differences between these two results might be explained by the fact that within DMFT *Mn* and *Ni* atoms are only coupled via the general many-body and charge-self consistency conditions, while correlations are treated independently on the two atoms. In contrast, the present VCA approach treats correlations exactly on the length scale of the cluster.

These inter-atom correlations are possibly responsible for the splitting of the cova-

lent *Ni-Mn-d* electron hybridization in the majority spin states. Due to the breaking of this hybridization, the *Mn-d* exchange splitting is decreased, which could explain the slight shifts of the minority unoccupied and occupied majority *Mn-d* states.

3.2.5 Spectral properties

In order to gain insight into the non-local features of the density of states, we compute the \mathbf{k} -resolved spectral function $A(\mathbf{k}, \omega)$. Majority- and minority-spin spectral functions are presented in Figs. 3.12 and 3.13, respectively, with \mathbf{k} following high-symmetry points in the Brillouin zone (BZ). The explanation of the main features of the LSDA band structure was provided by *de Groot et. al.* in his pioneering paper [64]. Emphasis was placed on the interaction between *Mn* and *Sb* connected by the symmetry constraint, while less attention was given to the *Ni* atom, although *Mn* and *Ni* are first-neighbors and a strong hybridization between them is evidenced in the density of states. In our LDA+VCA calculation, *Ni-d* and *Mn-d* states are included explicitly, while *Sb-* states are admixed by the downfolding procedure.

Due to correlation, the majority-spin bands crossing the Fermi energy are substantially narrowed with respect to the uncorrelated LSDA bands. Specifically, our results show for the bands crossing the Fermi-level a reduction of the bandwidth from 3.2eV to 2.2eV. Along the path $\mathbf{W} \rightarrow \mathbf{L}$ both LSDA bands and the VCA spectral function cross the Fermi-level at almost the same \mathbf{k} -point. The degenerate unoccupied level situated in the \mathbf{L} -symmetry point, around 1.5eV, is strongly pushed towards the Fermi energy, and determines the appearance of the peak visible at 0.5eV in the DOS discussed in Sec. 3.2.4. At the same time, correlation effects further split the degenerate levels at the $\mathbf{\Gamma}$ -point seen in LSDA at around 2eV. Note that along $\mathbf{\Gamma} \rightarrow \mathbf{X}$ crossing of the Fermi-level occurs close to the corresponding crossings of the LSDA-bands.

Furthermore, along the path $\mathbf{X} \rightarrow \mathbf{W} \rightarrow \mathbf{K}$ both VCA and LSDA bands are only weakly dispersive. However, the VCA bands are shifted towards the Fermi-level, while along the line back into the $\mathbf{\Gamma}$ -point, the Fermi-energy crossing of the VCA bands takes place closer to the \mathbf{K} -point.

The minority-spin band structure of LSDA shows an indirect gap of about 0.5eV between $\mathbf{\Gamma}$ and \mathbf{X} -point. Within this indirect gap formed by the mostly *Ni-d* occupied and mostly *Mn-d* unoccupied states, the LDA+VCA results show substantial spectral weight, as can be seen in Fig. 3.13. Notably, across the Fermi-level a weakly-dispersive band is present, centered around 0.1eV, representing the NQP-states. At higher energies, in the range of 1 to 2eV above E_F , the VCA bands are substantially correlation-narrowed with respect to LSDA. The features above the Fermi-level, including the non-quasiparticle states, have dominant *Mn-d* character.

Below the Fermi-level, correlations split off the occupied bands having mainly *Ni-d* character. The spectral weight is redistributed: a part is transferred towards the Fermi-level, however with smaller weight, while most weight is transferred towards

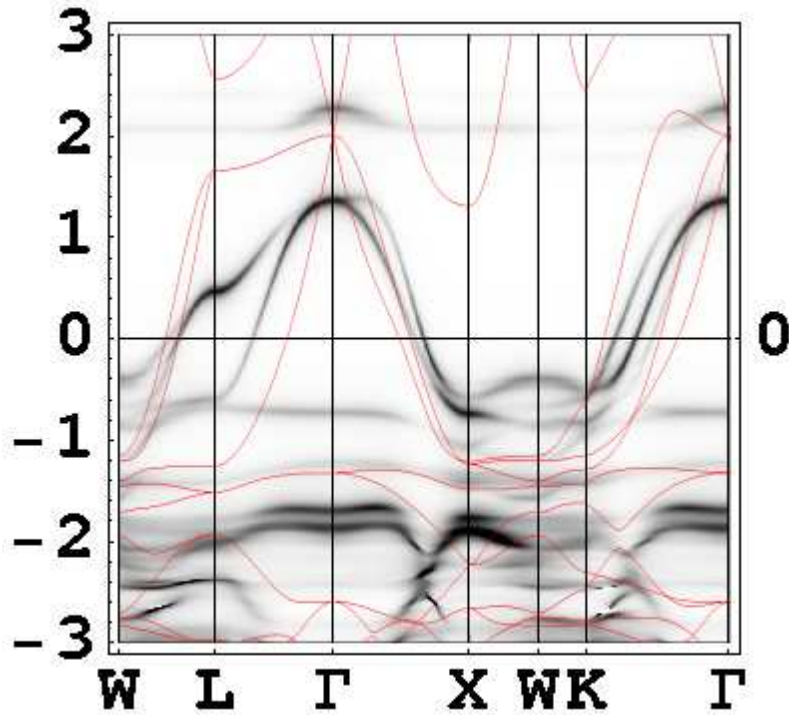


Figure 3.12: Majority spin LDA+VCA spectral-function of NiMnSb (black/white density plot) along the conventional path in the BZ. $\mathbf{W}(0.5, 1, 0)$, to $\mathbf{L}(0.5, 0.5, 0.5)$ through $\mathbf{\Gamma}(0, 0, 0)$, $\mathbf{X}(0, 1, 0)$, $\mathbf{K}(0, 0.75, 0.75)$ points and ending at $\mathbf{\Gamma}(0, 0, 0)$. The LSDA bands (red, thin solid lines) are shown for comparison. Parameters are as in Fig. 3.10.

higher binding energies. The same effect is visible in the density of states plot displayed in Fig. 3.10. Notice that while the shift towards higher binding energies is also seen in the previous LSDA+DMFT calculation [7], the weak shift towards the Fermi-level is only obtained within the present calculation.

3.2.6 Local and non-local self-energies

In order to explore correlation effects in more detail, we plot in Fig. 3.14 the on-site total (i.e. traced over orbitals) self-energy on Mn and Ni sites on a large energy window $E = E_F \pm 5\text{eV}$. The upper/lower panel of Fig. 3.14 shows the spin resolved real/imaginary parts of the self-energy near the Fermi crossing at $\mathbf{k} = (0.5, 0.7, 0.3)\pi/a$. Both $\text{Im}\Sigma$ on Mn and Ni show a peak just above the Fermi level within the minority spin channel, signaling the presence of NQP states in the

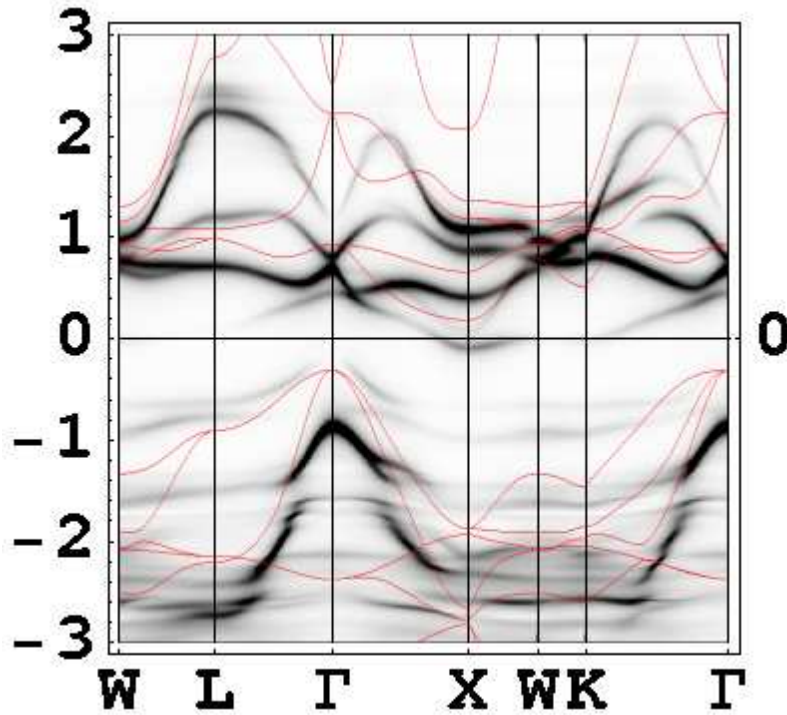


Figure 3.13: Minority-spin LDA+VCA spectral function of NiMnSb (black/white density plot) along the same BZ path as in Fig. 3.12. The LSDA bands (red, thin solid lines) are shown for comparison. Parameters are as in Fig. 3.10.

density of states. The difference between majority and minority spin contribution is significant in *Mn* owing to its large magnetic moment, while the small *Ni* moment agrees with the minor differences found between the self-energies of the minority and the majority spin channel.

Looking closer at the results for manganese, its minority-spin self-energy is significantly different in comparison to the self-energy of the majority spin channel. Especially just above the Fermi-level, a clear peak in $\text{Im}(\Sigma_{VCA}^\downarrow)$ is present with a maximum around the energies of the non-quasiparticle states (see Fig. 3.10 and Fig. 3.13). In previous DMFT calculations [7], a very similar behaviour of the imaginary part of the local self-energy was seen. In that case, the pronounced feature above E_F was attributed to the minority *Mn-d*(t_{2g}) states. The real part of the self-energy displays a negative slope $\partial\Sigma/\partial\omega < 0$ at the Fermi energy for both spin directions, which confirms that the quasiparticle weight $Z = (1 - \frac{\partial\Sigma}{\partial\omega})^{-1}$ is reduced by

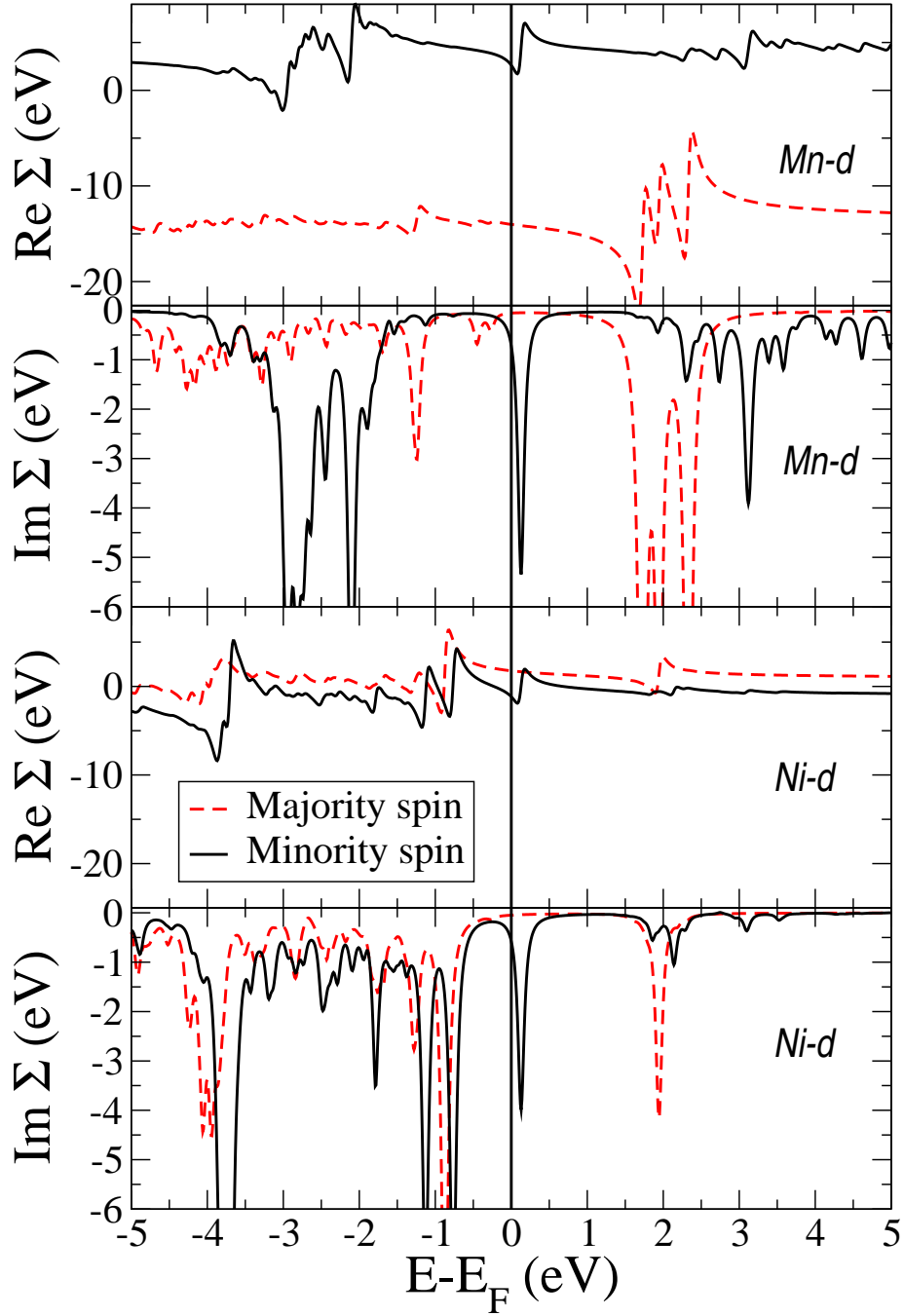


Figure 3.14: Spin resolved self-energies for Mn and Ni sites obtained as a sum of orbital-diagonal contribution, at the crossing point $\mathbf{k} = (0.5, 0.7, 0.3)$. The strong $Mn-d$ spin splitting is due to the significant difference between majority and minority spin self energies, while the lack of magnetic moment on Ni is a consequence of similar spin resolved selfenergies.

correlations. However, while for majority spins $|\partial\Sigma_{\uparrow}/\partial\omega|$ is clearly less than unity, for minority spins $|\partial\Sigma_{\downarrow}/\partial\omega| \gtrsim 1$ (within our approximation, we cannot determine Σ with sufficient accuracy), suggesting the nonquasiparticle nature of the minority spin states within the gap.

To illustrate non-local correlation effects, we plot in Fig. 3.15 the majority-spin (upper panels) and the minority-spin (lower panels) imaginary parts of the local (left column) and non-local (right column) self-energies between various orbitals, on the energy scale of $E_F \pm 2\text{eV}$ around the Fermi-level.

In the minority spin channel, within this energy range, the largest term is the one connecting $Mn-(t_{2g})$ and $Ni-(t_{2g})$ orbitals just above the Fermi level. This is the energy at which NQP-states appear in the density of states (Fig. 3.10). Notice that at the same energy a strong local contribution to $\text{Im}\Sigma$ is present as well. The additional non-local contribution results in an enhancement of the NQP-spectral weight as compared to its value obtained from DMFT-calculations [7]. Notice that all other non-local contributions to $\text{Im}\Sigma$ are significantly smaller.

In the local contributions below the Fermi energy, at about $E_F - 1\text{eV}$ two maxima are visible. In the minority spin channel, the lower energy maximum is dominated by the $Ni-(t_{2g})$ contribution, while the peak at higher energies is predominantly of $Ni-(e_g)$ character. These maxima contribute to the overall shift of Ni -states towards the Fermi-level, visible in the occupied part of the DOS in Fig. 3.10. These local orbital-diagonal contributions of $\text{Im}(\Sigma)$ produce changes in the density of states that are similar to the ones obtained from the local DMFT-approach [7].

For majority spin electrons, the site- and orbital diagonal contribution, shown in the upper left panel in Fig. 3.15, displays the same double peak structure at $E_F \approx -1\text{eV}$ for both $Ni-(t_{2g})$ and $Ni-(e_g)$ contributions as in the case of the minority spin electrons. However, in contrast to the minority spin contribution the $Mn-(t_{2g})$ contribution is visible and overlaps significantly with $Ni-(t_{2g})$. At this energy the $Ni-(e_g)$ contribution is reduced, which causes an enhancement of the higher energy peak where $Ni-(e_g)$ is dominant. There is no Mn -contribution at all in the higher energy peak, however, at energies closer to E_F a second $Mn-(t_{2g})$ peak is visible. This has important consequences for the majority spin density of states. The correlation induced spectral weight transfer towards the Fermi energy can be attributed to the appearance of self-energy contributions, which are site- and orbital-diagonal and close to the Fermi-level. In addition, this contribution changes the $Mn(d)$ - $Ni(d)$ hybridization. The majority spin site- and orbital-off-diagonal contributions, shown in the upper, right corner of Fig. 3.15, are less significant than its minority spin analog.

The above analysis clearly emphasizes the influence of non-local correlations cap-

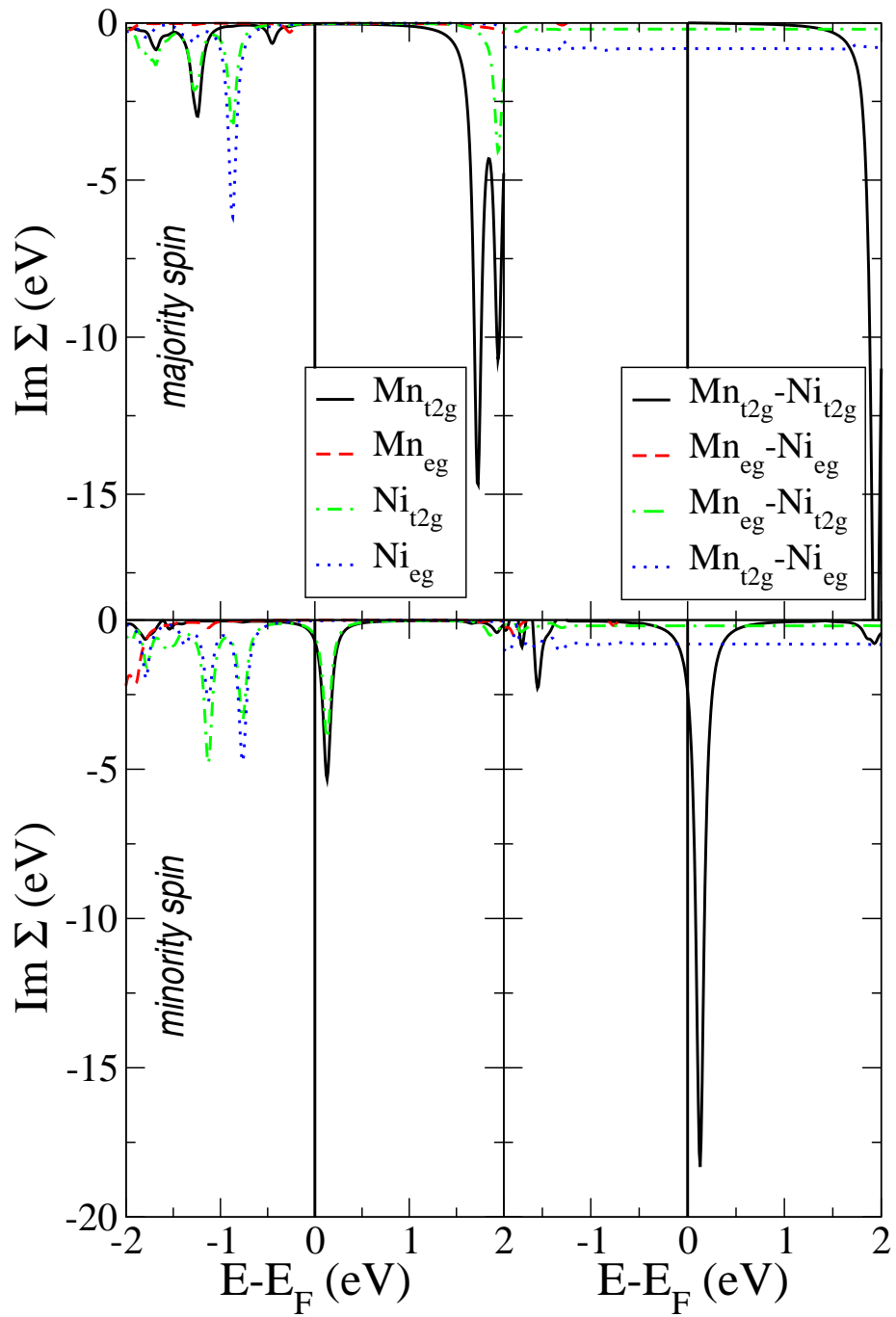


Figure 3.15: Imaginary part of the local and orbital-diagonal self-energy (left column). The right column shows the nearest-neighbor parts of $\text{Im}\Sigma$.

tured by the VCA, as well as the necessity to consider both *Mn*- and *Ni-d* orbitals to obtain a complete picture for the low energy physics in NiMnSb.

3.2.7 Low-energy spin polarization and comparison with experiments

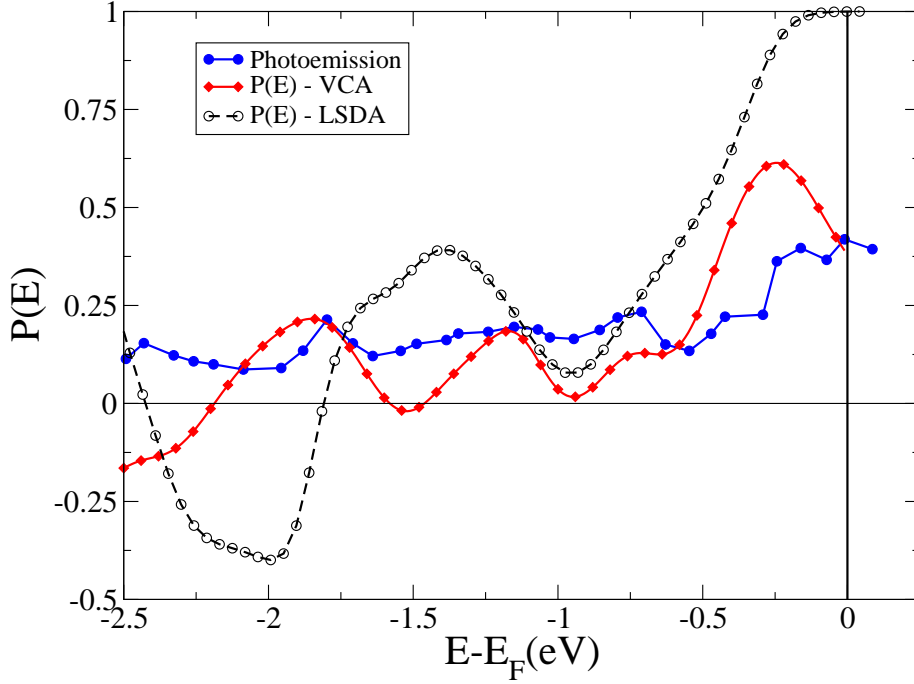


Figure 3.16: Energy-dependent polarization obtained from LSDA and LDA+VCA in comparison with data from spin-polarized photoemission [3] (data used with kind permission from the authors).

To investigate the consequences of the modification of majority and minority spectral weight at the Fermi energy produced by correlations, we turn to the issue of the spin polarization. This is given by the expression

$$P(E) = \frac{N_{\uparrow}(E) - N_{\downarrow}(E)}{N_{\uparrow}(E) + N_{\downarrow}(E)},$$

with $N_{\sigma}(E)$ being the spin-resolved density of states, and is plotted in Fig. 3.16 as a function of energy E measured with respect to the Fermi-level. The computed LSDA and VCA values are compared with the raw data obtained from spin-resolved photoemission measurement by Zhu et al. [3]. For this comparison, the density of states was multiplied with the Fermi-function and a Gaussian broadening of 100meV

was used to account for experimental resolution. *Zhu et.al* [3] discuss the appearance of a shoulder close to the Fermi-level when proper annealing is performed to restore the stoichiometry in NiMnSb. This shoulder is visible in the majority spin channel (Fig.2c from Ref. [3]) and could be an indication for the correlation-induced spectral weight transfer of the majority spin states, not present in the LSDA calculations. In addition, the value of the spin polarization at the Fermi-level obtained from our LDA+VCA-results is situated in the interval of values reported experimentally [85, 3, 51].

At the end of this section we want to comment on the connection between the present approach and the seminal works of *Edwards* and *Hertz* [61, 86], followed by *Irkhin* and *Katsnelson* [62, 74, 87, 88] to describe properties of itinerant electron ferromagnets using the Hubbard-model. In particular, the self-energy was computed for the interesting case of strong ferromagnetism, where all the electrons have only one spin direction (the half-metallic systems in discussion) using diagrammatic perturbation [61, 86], *s-d*, spin-wave theory [62, 87] or many-electron X-operator representation [74, 88]. In a more physical picture the self-energy represents the process of magnon emission and absorption by an electron as the electron's response to the fluctuating magnetic field that it sees as it moves through the crystal [61, 86]. It was demonstrated that a such caused self-energy affects significantly the one-electron states by introducing non-quasiparticle contributions, which was later confirmed by numerical calculations in realistic materials [71, 7, 54, 55, 72, 73, 54],[P1].

In the present work we have extended previous LDA+DMFT results for NiMnSb [71, 7] in order to include many-body effects which are beyond the single-site description. A natural extension can be achieved using the cluster perturbation theory, where interaction is treated exactly at the length scale of the cluster. As clusters including Mn-only basis sets are not sufficient to describe the low energy features around Fermi-energy ([P2] and App. E), we included here explicitly Ni-*d* orbitals in the basis. Thus, the computed cluster contains two sites and a number of five orbitals are considered on each site. The magnon excitations arise owing to the spin dynamics, the spin-flip and pair-flip terms included in the Hamiltonian.

Note that, both in the framework of single-site DMFT and within this cluster method the magnon dispersion cannot be properly taken into account when considering the effects of electron-magnon interaction since the magnon frequencies are replaced by some average value ω . This means that the detailed shape of the nonquasiparticle contributions to the density of states ($E - E_F \ll \hbar\omega$), $\delta E \propto (E - E_F)^{3/2}$, see (Ref. [62, 86, 88]), cannot be reproduced correctly in both these approaches. Notice, however, that the values of magnon frequencies are not essential to estimate the total spectral weight of the nonquasiparticle states and DOS in general at $E - E_F > \hbar\omega$, see also (Ref. [71]).

3.2.8 Summary

We have investigated correlation effects in NiMnSb using a combined LDA+VCA approach and results obtained from two distinct basis sets were studied. A reduced basis set, employing only $Mn-d$ as suggested by the literature [2], and further an extended basis which includes $Mn-d$ and $Ni-d$ states. Concerning the appropriate choice of basis for this material, our results lead to the conclusion that although $Mn-d$ accounts significantly for the physics at the Fermi-energy, also the $Ni-d$ states have to be considered to fully describe the low energy physics around the Fermi-energy.

Following this conclusion, the parameters for the effective non-interacting Hamiltonian were obtained using the downfolding procedure, for a basis including Ni and $Mn-d$ orbitals. The multi-orbital Hubbard-type many-body Hamiltonian was solved using the variational cluster approach for different values of $U_{Mn/Ni}$ in the range of 2 – 3eV and for $J_{mm'mm'}$ for which the orbitally averaged value $\bar{J}_{Mn/Ni}$ ranges between 0.65/0.78eV. The results presented do not show significant differences for the studied range of parameters, nor for different double-counting procedures used.

The presence of $Ni-d$ orbitals in the NMTO-basis allows for a more complete description of the low-energy behavior of NiMnSb as it leads to a correct description of the spectral weight transfer towards the Fermi-level in the majority spin channel. Moreover, it shows in agreement with LDA+DMFT the formation of minority-spin states with vanishing quasiparticle weight (NQP-states) just above the Fermi-level. The analysis of the minority-spin spectral function shows for the NQP-states a weakly dispersive band having dominantly $Mn-d$ character. Due to electron correlations, the covalent $Ni-Mn d$ -hybridization in the majority-spin channel splits up and part of the weight is transferred towards the Fermi-level.

The *simultaneous* presence of majority spin spectral weight transfer towards the Fermi-level, and the occurrence of minority-spin non-quasiparticle states emphasizes the importance of correlation effects in this material, despite the small value of U . One should remark that our results were obtained in the ideal isotropic case, while it is known that epitaxially grown NiMnSb displays significant uniaxial anisotropy [70]. When taking into account this effect, we expect nonquasiparticle states to be shifted to higher energies away from the Fermi surface, due to the corresponding gap occurring in the magnon spectrum.

Despite the fact that high-quality films of NiMnSb have been grown, they do not reproduce the half-metallic character of the bulk detected by spin-polarized positron annihilation [65, 66]. On the other hand, one should mention that the positron annihilation technique only provides an evidence for halfmetallicity by means of a consistency check. In other words, the “proof” is carried out by modeling the data

assuming a half-metallic band structure, with a full minority spin gap, *from the outset* [65, 66]. For this reason, it would be interesting to revisit the analysis of the positron-annihilation data by using the correlated band structure obtained here, in other words by taking into account the existence of non-quasiparticle states.

3.3 Half-metallicity at interfaces: (CrAs)/(GaAs)-superlattices

3.3.1 Introduction

The major players in the present-day semiconductor-based electronics have a zinc-blende structure. Therefore, half-metals which would follow the structure and bonding of zinc-blende semiconductors are especially attractive as they are compatible with existing technology.

Recently, zinc-blende CrAs was predicted to be half metallic from first-principles calculations [89, 90]. In addition, its density of states (DOS) does not show any clear peaks around the Fermi level, suggesting that the majority spin states at the Fermi level are not strongly localized and therefore zinc blende CrAs could be a good conductor.

As the zinc-blende configuration is not a stable phase of CrAs, it is not possible to grow sufficiently thick films which are needed for applications in practical devices. It is, however, possible to grow thin films and consequently the idea evolved to stack such zinc-blende CrAs thin films alternating with semiconducting layers to build sufficiently large half-metallic heterostructures.

In recent years, the increasing ability to control the growth of semiconductor crystals has made possible the fabrication of such high-quality artificial heterostructures of many different geometries and semiconductor classes. These heterostructures containing half-metals with semiconductors are technologically very attractive, since in principle they can be used to achieve high polarization spin injection from a ferromagnetic electrode into the semiconductor. The high polarization is a result of the central property of half-metallic ferromagnets, that is these materials exhibit a metallic density of states for one spin channel and a gap at Fermi-level for the other [64, 71].

3.3.2 Electronic structure of CrAs

In order to discuss how the hetero-structure gap is affected by the presence of electron-electron interactions, let us briefly summarize the principal physical factors leading to gap formation in the zinc-blende structures. Bulk properties of zinc-blende pnictides and chalcogenides were discussed in many papers [91, 92, 93, 94].

In this structure, every atom has tetrahedral coordination with the first neighbors being of the other atomic species. The d -states split into the $d(t_{2g})$ and $d(e_g)$ manifolds. While the $d(t_{2g})$ -states hybridize with the p -states of the neighboring

atom, forming bonding and anti-bonding states, the later $d(e_g)$ orbitals are practically non-bonding and form narrow bands. The bonding anti-bonding splitting is a characteristic for the tetrahedral coordination. The Fermi-level E_F is situated in the gap between the bonding bands and the narrow non-bonding $d(e_g)$ -bands. In addition, the existence of the band gap is assisted by the exchange splitting which keeps minority $d(e_g)$ states higher in energy. This situation can change when lattice parameters are modified, typically when the half-metal is grown on a semiconductor substrate. If the lattice mismatch is small, the electronic structure will change only slightly.

Electronic structure calculations for bulk CrAs with different lattice constants at finite temperatures and in presence of correlation effects were performed recently [53]. In this work, correlations were shown to induce spectral weight above the Fermi-energy in the minority spin gap, with the consequence that the material remains half-metallic. The spectral weight in the minority spin gap is known to be produced by so-called non-quasiparticle (NQP) states. The occurrence of these states is connected to “spin-polaron” processes [61, 62]: the spin-down low-energy electron excitations, which are forbidden for half-metallic ferromagnets in the one-particle picture, turn out to be possible as superpositions of spin-up electron excitations and virtual magnons [61, 62]. The only situations in which substantial half-metallicity was preserved in calculations of our group was in the case of CrAs and VAs, while in others, like in (semi-)Heusler materials (e.g. NiMnSb), a strong depolarization takes place [7, 95, 72],[P7]. In contrast to these many-body effects, the spin-orbit coupling, which causes depolarization through the mixing of the two spin channels, was found in CrAs to be less than 1% [96]. Consequently, this interaction is not taken into account in the present calculations.

It is the purpose of the present work to investigate effects caused by many-body correlations at finite temperatures in zinc-blende CrAs/GaAs interfaces and multilayers. These ab-initio calculations are performed within a combined density functional and many-body approach at finite temperatures. We mainly focus our attention on the spin polarization at the Fermi-level and possible depolarization effects determined by strong electron-electron interactions.

3.3.3 Geometry of multilayers

Recently, *Zhao* and *Zunger* [97] investigated the relative stability of NiAs and ZB structures under pseudomorphic epitaxial conditions. They found that under epitaxial growth condition, most of the *Cr* and *Mn* pnictides and chalcogenides cannot be stabilized below a lattice constant of 6.5\AA . However, these conclusions are valid for the growth of thick layers, whereas the growth of very thin films is dominated by the strain energy at the interface. This explains the experimental observation that CrAs

can be grown in the zinc-blende structure for thicknesses up to a few monolayers.

The first experimental realization of such thin films was done by *Akinaga et al.* [90]. They have synthesized zinc-blende CrAs thin films of 3nm thickness on GaAs substrates. They measured a magnetic moment of $3\mu_B$ which is in agreement with theoretical prediction, and found an experimental Curie temperature of above 400 K [90]. From the experimental point of view, such a small thickness makes this material difficult to use in practical devices. Therefore, attention was directed towards CrAs/GaAs multilayers [98]. Previous ab-initio calculations showed high spin polarization through the entire region of the multilayer in the case of $(\text{CrAs})_2/(\text{GaAs})_2$, where two monolayer CrAs and two monolayer of GaAs are stacked alternatively [99]. Initially the produced multilayers of zinc-blende CrAs/GaAs grown on GaAs substrates [98] indicated that the surface and interface of the multilayer were not completely flat. However, it was found that the multilayers grow much thicker than pure zinc-blende CrAs. Recently, by optimizing the growth temperature, the quality of the samples was improved significantly and epitaxial growth of zinc-blende multilayer with flat surface and interface was achieved [100]. Magnetisation measurements for a multilayer structure of $(\text{CrAs})_2/(\text{GaAs})_2$ repeated 100 times [100] showed a value of $2\mu_B$ per formula unit, lower than the theoretical prediction of $3\mu_B$. In addition, the temperature dependence of magnetisation indicated a ferromagnetic transition temperature of about 800K. It has been confirmed by electronic structure calculations that the spin polarization is preserved throughout the multilayer, and in addition that it is insensitive to substitutional disorder between the *Cr* and *Ga* sites [99].

In agreement with [99], we chose the interface geometry such that an As-atomic layer is placed between *Ga* and *Cr* atomic layers.

As outlined, the experimental limit for thickness of single layers of CrAs on GaAs appears currently to be 3 nm, which corresponds to about five layers CrAs. Consequently, we study multilayers of up to five monolayers of CrAs and GaAs. More precisely, calculations are done for the $(\text{CrAs})_n/(\text{GaAs})_n$ superlattice structures with $n = 1, 2, 3, 5$.

The different structures are depicted in Fig. 3.17.

The supercells are described by a tetragonal lattice with the constants $a = b = a_0/\sqrt{2}$ and $c = a_0 \times n$. In these calculations [P8] we used the lattice parameter $a_0 = 5.75\text{\AA}$, which is the optimized GaAs lattice constant obtained from a spin-GGA calculation [4]. This value is slightly larger than the one found experimentally for bulk GaAs (5.65\AA) and the one predicted for $(\text{CrAs})_2/(\text{GaAs})_2$ double monolayers (5.69\AA) [99].

Quite generally half-metallic ferromagnets are sensitive to different lattice constants, so we performed additional calculations for $(\text{CrAs})_1/(\text{GaAs})_1$ and $(\text{CrAs})_3/(\text{GaAs})_3$ using the bulk GaAs-lattice constant (5.65\AA).

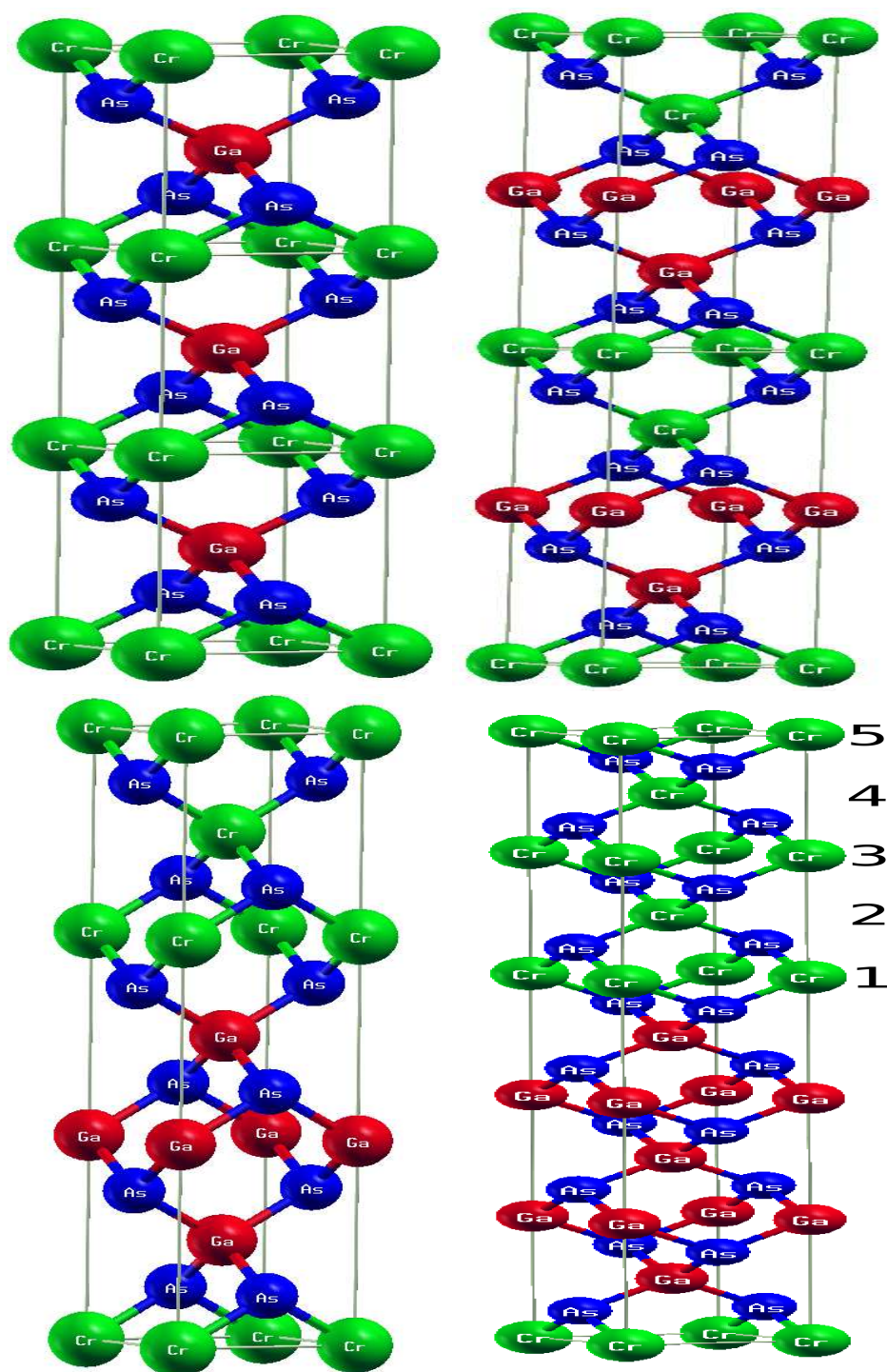


Figure 3.17: The supercells for the $(\text{CrAs})_n/(\text{GaAs})_n$ compounds. Cr (green), As (blue) and Ga (red). On the top left, $n = 1$ the cell is repeated three times along z . On the top right, $n = 2$, the cell is repeated twice, while on the bottom left and right, the $(\text{CrAs})_3/(\text{GaAs})_3$ and $(\text{CrAs})_5/(\text{GaAs})_5$, respectively, is presented. For $(\text{CrAs})_5/(\text{GaAs})_5$ the individual Cr-layers are marked in agreement with section 3.3.5.

3.3.4 Method - the LDA+DMFT scheme

So far the LDA+VCA scheme was used to investigate electron correlation effects in (bulk) materials of interest. Due to the large unit cells of the heterostructures it is not feasible to use the LDA+VCA approach as the required effort in downfolding is impractical and second, the Hilbert-space of the large basis sets would be prohibitively large. Therefore a different ab-initio approach is used, the LDA+DMFT method, which is better suited for large supercells. In the following this well known method is shortly outlined.

In the recently developed LDA+DMFT scheme [16], correlation effects in the valence Cr- d orbitals are included via an on-site electron-electron interaction in the form $\frac{1}{2} \sum_{i\{m,\sigma\}} U_{mm'm''m'''} c_{im\sigma}^\dagger c_{im'\sigma'}^\dagger c_{im''\sigma''} c_{im'''\sigma'''} c_{im''\sigma''} c_{im'\sigma'} c_{im\sigma}$. The interaction is treated in the framework of dynamical mean field theory (DMFT) [15], with a spin-polarized T-matrix Fluctuation Exchange (SPTF) type of impurity solver [77]. Here, $c_{im\sigma}/c_{im\sigma}^\dagger$ are the usual fermionic annihilation (creation) operators acting on an electron with spin σ on orbital m on site i . The Coulomb matrix elements $U_{mm'm''m'''}$ can be computed for the particular material taking into account the symmetry of the orbitals and of the crystal structure in terms of effective Slater integrals and Racah or Kanamori coefficients [22, 15].

To describe electron correlations in $(\text{CrAs})_n/(\text{GaAs})_n$, we used the following effective Slater parameters: $F^0 = 3\text{eV}$, $F^2 = 7.73\text{eV}$ and $F^4 = 4.863\text{eV}$ (which results in a Coulomb-interaction of $U = 3\text{eV}$ and a Hund's rule coupling of $J_{t2g} = 0.9\text{eV}$). These values are in agreement with previous works [7, 53, 54, 55].

Notably, constrained LDA predicts significantly larger values for the Coulomb-interaction, $U = 6.5$ [53]. This large value for the Coulomb-interaction is believed to be an overestimation, nevertheless calculations with this value showed only negligible differences from the results presented here. For the exchange correlation functional the LSDA-approximation was used, as we found no differences to results obtained with the GGA-approximation.

Double counting correction Similar to LDA+VCA, the static part of the interaction is already included in the local spin-density approximation (LSDA); therefore these “double counted” terms must be subtracted. To achieve this, we replace $\Sigma_\sigma(E)$ with $\Sigma_\sigma(E) - \Sigma_\sigma(0)$ [101] in all equations of the LDA+DMFT procedure [15]. Physically, this is related to the fact that DMFT only adds *dynamical* correlations to the LSDA result. For this reason, it is believed that this kind of double-counting subtraction “ $\Sigma(0)$ ” is more appropriate for a DMFT treatment of metals than the alternative static “Hartree-Fock” (HF) subtraction [32].

Due to the required numerical effort it was not feasible to use identical resolution in \mathbf{k} -space for all supercells. For $(\text{CrAs})_1/(\text{GaAs})_1$ and $(\text{CrAs})_2/(\text{GaAs})_2$ we used 440 \mathbf{k} -vectors in the irreducible part of the Brillouin-zone which corresponds to

1599 \mathbf{k} -vectors in the full Brillouin-zone. For and $(\text{CrAs})_3/(\text{GaAs})_3$ we used 216, for the LSDA-calculation of $(\text{CrAs})_5/(\text{GaAs})_5$ 84 and for the LDA+DMFT calculation of $(\text{CrAs})_5/(\text{GaAs})_5$ 21 \mathbf{k} -vectors in the irreducible part of the Brillouin-zone which corresponds to 767, 287 and 71 \mathbf{k} -vectors in the full Brillouin-zone. In all calculations we used a cutoff of $l_{\text{max}}=6$ for the multipole expansion in charge density and the potential as well as a cutoff of $l_{\text{max}}=4$ for the wavefunctions. We checked higher cutoffs for $(\text{CrAs})_1/(\text{GaAs})_1$ and found only negligible differences. For the DMFT-results we used a temperature of 200K, however calculations at 300K show no differences.

A broadening of 0.014eV was used for $(\text{CrAs})_1/(\text{GaAs})_1$, $(\text{CrAs})_2/(\text{GaAs})_2$ and $(\text{CrAs})_3/(\text{GaAs})_3$ and a broadening of 0.07eV was used for $(\text{CrAs})_5/(\text{GaAs})_5$ in the calculation of the density of states of these systems.

3.3.5 Results

Density of states

Figures 3.18, 3.19 and 3.20 show the evolution of the total density of states in LSDA when increasing the number of monolayers. In all cases, LSDA predicts $3.0 \mu_B$ magnetization per formula unit. Fig. 3.18 shows the evolution of the density of states of the heterostructures within LSDA and LDA+DMFT, respectively. The results from both methods show with the exception of $(\text{CrAs})_1/(\text{GaAs})_1$ that half-metallicity is conserved throughout. Although the geometry of the minority spin gap changes for the individual structures, no interface states are formed within the minority spin gap for multilayer structures with more than one layer of CrAs. In case of $(\text{CrAs})_1/(\text{GaAs})_1$, interface states are visible in the minority spin gap in Fig. 3.19 for both LSDA and DMFT-results. We have verified that these states are genuine and are not caused by broadening.

It is interesting to note that local correlations shift the peak located at about -1eV in the LDA+DMFT results further away from the Fermi-energy. This has the consequence that the minority spin gap is effectively enlarged in comparison to the LSDA-results. In the majority spin channel it is interesting to note that the density of states of $(\text{CrAs})_1/(\text{GaAs})_1$ shows at +2eV a depression, that appears shifted closer to Fermi-energy (about +1eV) for $(\text{CrAs})_2/(\text{GaAs})_2$ and is not found in the density of states of $(\text{CrAs})_3/(\text{GaAs})_3$ and $(\text{CrAs})_5/(\text{GaAs})_5$.

While the LDA+DMFT yields for single, double and triple monolayers a distinctly different density of states, the result for five monolayers shows only minor differences with respect to the triple monolayer result and appears already to be close to the limit of an infinite number of monolayers. It is interesting to note that a small number of monolayers actually favors halfmetallic ferromagnetism, as the gap in the minority spin is largest and centered at Fermi-energy in the cases of single and double monolayers. For three and five monolayers, this gap becomes smaller due to an increase

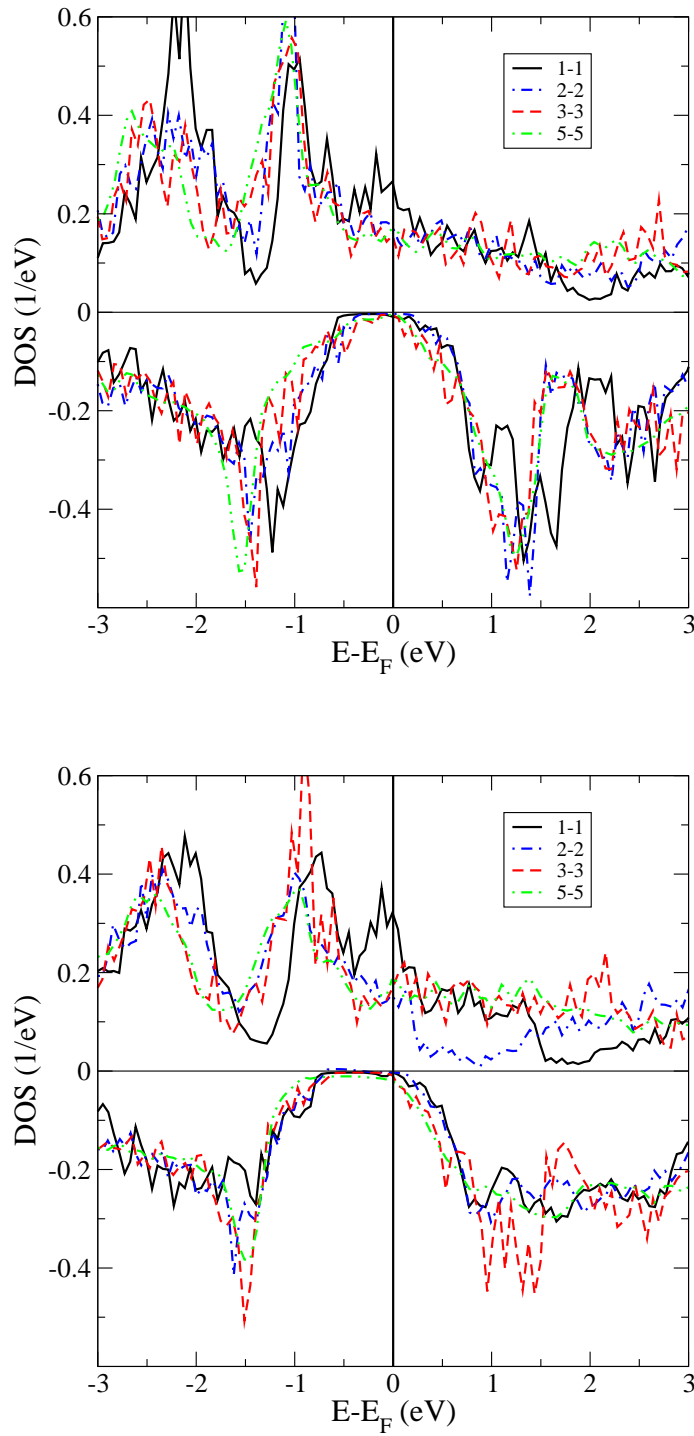


Figure 3.18: Overview of the total density of states of LSDA and LDA+DMFT for $(\text{CrAs})_n/(\text{GaAs})_n$ for $n = 1, 2, 3, 5$.

in spectral weight of the states located closely above Fermi-energy and a broadening of the peak located at -1.5eV .

$(\text{CrAs})_1/(\text{GaAs})_1$ shows a peculiar peaked structure in the majority spin at the Fermi-energy that is not found in the results for the other multilayer structures and also not seen in bulk CrAs. This peak at the Fermi-energy is even more pronounced in the LDA+DMFT results and indicates that the Cr- d electrons are significantly localized. Further, the introduction of local correlations shifts the peak located at about -1eV in majority spin channel in the LSDA-results closer to the Fermi-energy in the LDA+DMFT results. At the Fermi-energy the peak-like structure in the LSDA-results is even more pronounced in the LDA+DMFT results. The density of states below about 2eV and above the Fermi-energy is mostly unchanged. In the minority spin channel, correlations shift the peak located at about -1eV in the LSDA-results even further away from the Fermi-energy. This is due to correlation effects as this peak in the minority spin consists of Cr-As-hybridized states, which are pushed away from the Fermi-energy. This effectively enlarges the minority spin gap by about 0.3eV . In addition, a redistribution of spectral weight takes place for the structure located at about 1eV in the minority spin channel of the LSDA-results. The peak like structure is more flattened in the LDA+DMFT results.

In the LDA+DMFT-results the spectral weight of the states located at 0.5eV above the Fermi-energy increased slightly, and we attribute this to the appearance of non-quasiparticle states which increase spectral weight at this energy.

For all multilayers we find that the dominant peak at -1eV in the majority spin channel is shifted towards the Fermi-energy. This is caused by local correlations, as this peak is of dominant Cr- d character.

For $(\text{CrAs})_2/(\text{GaAs})_2$ the results for the majority spin channel show a redistribution of spectral weight, notably the peak located at -1eV in the LSDA-results is flattened and shifted closer to the Fermi-energy, while at $+1\text{eV}$ a depression in the density of states is found in the LDA+DMFT results.

In the minority spin channel the gap found in the LSDA-results is again enlarged in the DMFT-results as correlations push the peak located at -1eV further away from the Fermi-energy. The LDA+DMFT results show an increase of the spectral weight just above the Fermi-energy in comparison to LSDA-results.

In case of $(\text{CrAs})_3/(\text{GaAs})_3$, the results for the majority spin channel are similar to the results of $(\text{CrAs})_2/(\text{GaAs})_2$, with the exception that no depression of states is seen. In the minority spin channel the results from LSDA show only a very narrow gap of about 0.2eV magnitude. In comparison, the introduction of local correlations in the DMFT-results enlarges the gap to about 0.5eV . This is due to the fact that the onset of states located between -0.5eV and -1eV in the LSDA-results is suppressed in the DMFT-results. The peak at 1eV above the Fermi-energy experiences a slight

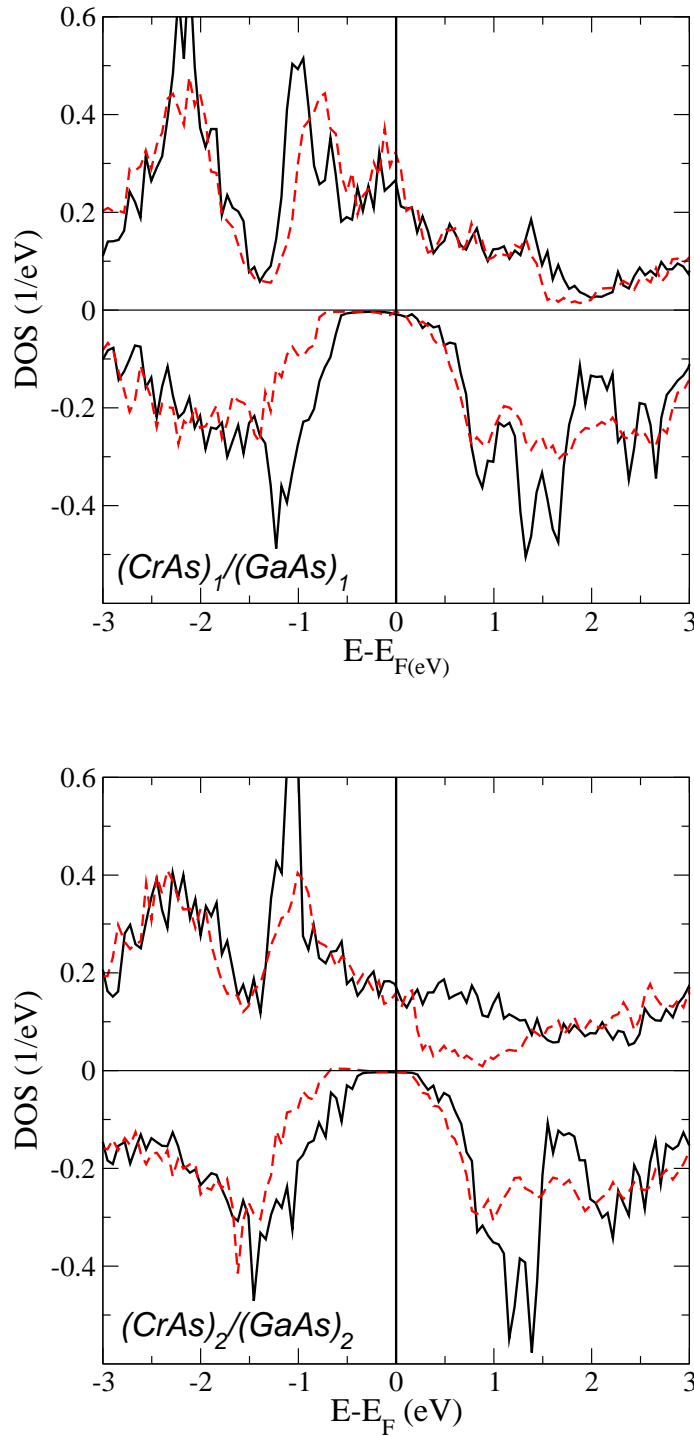


Figure 3.19: Comparison of the total density of states of LSDA and LDA+DMFT for $(\text{CrAs})_n/(\text{GaAs})_n$ for $n = 1, 2$; the results from LSDA are shown as solid black line, the results from DMFT as broken red line.

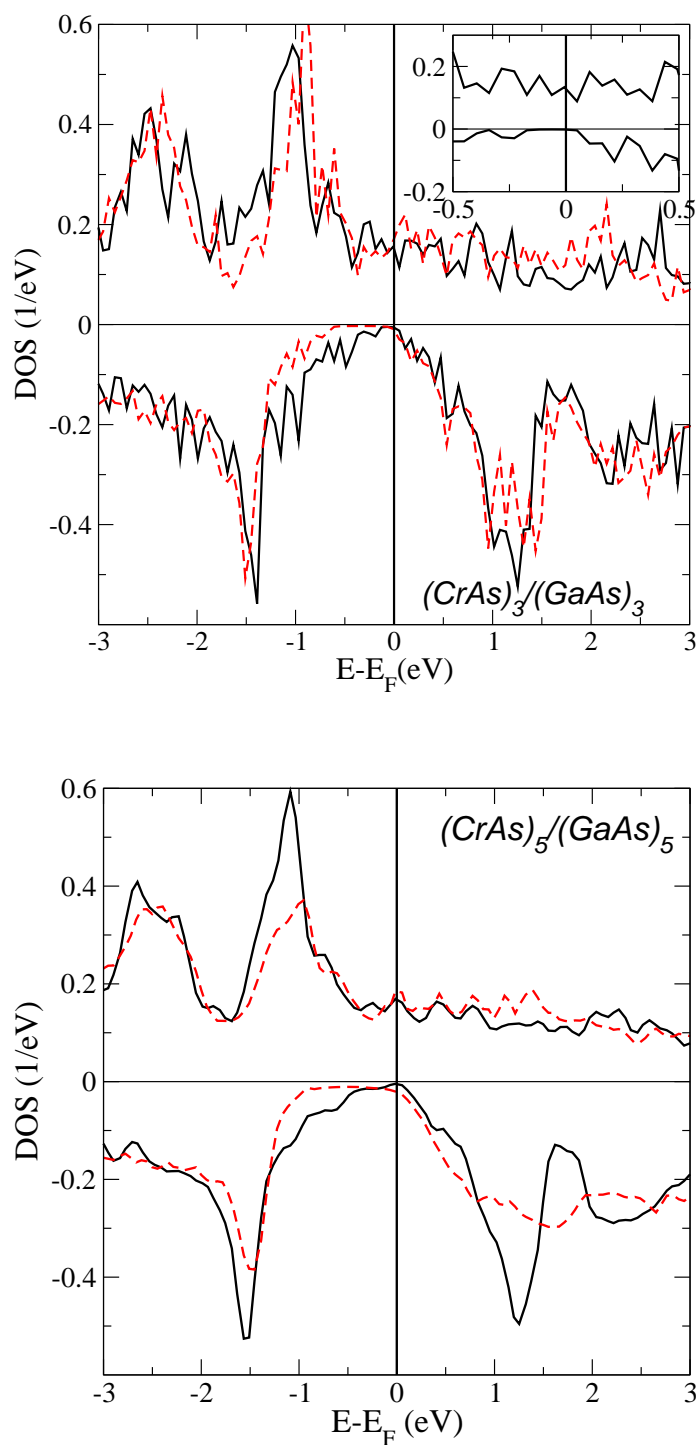


Figure 3.20: Comparison of the total density of states of LSDA and LDA+DMFT for $(\text{CrAs})_n/(\text{GaAs})_n$ for $n = 3, 5$; the results from LSDA are shown as solid black line, the results from DMFT as broken red line. In the upper plot the inset shows the LSDA-results around the gap with a reduced broadening of 0.004eV .

redistribution of spectral weight as its height is slightly reduced and the pseudo-gap like region at 1.5eV is slightly filled in the DMFT-results.

From the (CrAs)₅/(GaAs)₅ results only general conclusions can be drawn due to the low number of \mathbf{k} -vectors that are feasible for this large unit cell. In comparison to (CrAs)₃/(GaAs)₃ the results are very similar and differ mostly in fine details. This is probably due to the enlarged broadening and smaller number of \mathbf{k} -points used in this calculation. The majority spin channel shows the general behaviour that the large peak at -1eV is flattened and shifted closer to the Fermi-energy. The LSDA-results for the minority spin channel show the same small gap as it is found for (CrAs)₃/(GaAs)₃. The results from LDA+DMFT for (CrAs)₅/(GaAs)₅ show the same enlargement of the gap as found for (CrAs)₃/(GaAs)₃. From the results for (CrAs)₅/(GaAs)₅ it appears that (CrAs)₅/(GaAs)₅ is already very close to the limit of infinite number of layers.

Bulk limit

To investigate to which extent the interface affects the individual Cr-layers in comparison to bulk CrAs (bulk limit), Fig. 3.21 shows the Cr- d density of states of the individual CrAs layers of (CrAs)₅/(GaAs)₅. Three layers Cr1, Cr2, Cr3 are discussed as the remaining two are identical due to symmetry (see also Fig. 3.17 where the individual layers are numbered according to this scheme). Cr1 denotes the Cr- d states of the CrAs layer directly at the interface to GaAs, Cr2 the corresponding states in the next layer, which is at the same time the first layer surrounded only by CrAs-layers. Cr3 denotes the Cr- d states of the innermost CrAs-layer. For comparison the density of states obtained from LDA+DMFT for the Cr- d states of bulk CrAs (using the same lattice constant as for the supercells) is shown.

Quite generally, only the first Cr- d layer is significantly changed by the GaAs-interface and shows many redistributions of spectral weight in comparison to bulk CrAs. In the majority spin channel the LSDA-results of Cr1- d show a flattening of the peak located at -2.5eV, where the spectral weight is shifted closer to the Fermi-energy and fills the pseudo gap at about -1.75eV. The large peak at about -1eV is broadened in comparison to bulk CrAs. In the minority spin channel the results show a broadening of the peak located at -1.5eV, where a shoulder extends close to the Fermi-energy, up to about -0.4eV.

The density of states of Cr2- d and Cr3- d is very similar and especially Cr3- d is close to bulk CrAs.

It is interesting to note that the gap in the LSDA-results in the minority spin channel is nearly perfectly preserved in comparison to the LSDA-results for bulk CrAs, though it appears to be slightly shifted to higher energies. In the minority spin channel the Cr- d states below the Fermi-energy converge quickly to the bulk limit. This is in contrast to the region between 1eV and 2eV where convergence is slower;

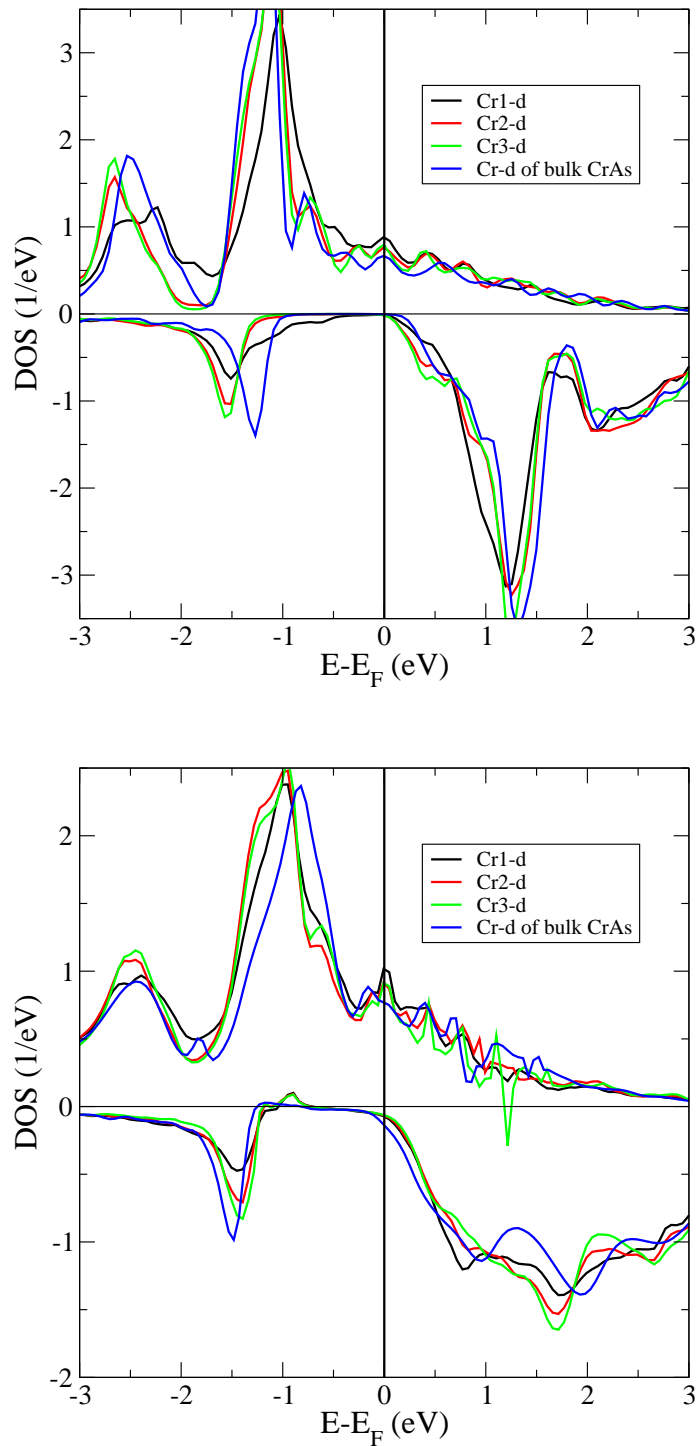


Figure 3.21: Density of states from LSDA (top) and from DMFT (bottom) for the Cr-*d*-orbitals of $(\text{CrAs})_5/(\text{GaAs})_5$ in comparison to the density of states from DMFT for the Cr-*d* states in bulk CrAs with the same lattice constant.

the dominant Cr- d peak seen in bulk CrAs is present in the supercell-results, however the pseudo-gap at 2eV forms stronger with increasing number of layers. Above 2eV the density of states for the Cr- d states of the supercell and from bulk CrAs are again fairly similar. The LDA+DMFT results show a fairly similar behaviour with respect to the bulk-limit. The majority spin density of states shows that the individual Cr- d states of the (CrAs)₅/(GaAs)₅ heterostructure are very close the Cr- d states of bulk CrAs with the exception of the position of the dominant peak at -1eV that appears slightly shifted in comparison. The density of states of the minority spin channel shows that as expected the Cr1- d states at the interface experience the largest deviations in comparison to bulk CrAs. Between the second and third Cr-layer the differences are very small and are below the Fermi-energy almost identical to the d -states of bulk CrAs. Above the Fermi-energy the depression at 1.5eV found in bulk CrAs is not present in the results of the heterostructure. However, with increasing number of layers the peak in bulk CrAs at about 2eV forms also in the results of the heterostructure, albeit shifted slightly closer to the Fermi-energy.

Influence of different lattice constants

In our calculations we used the lattice parameter $a_0 = 5.75\text{\AA}$, which is the optimized GaAs lattice constant obtained from a spin-GGA calculation [4]. As mentioned earlier, this value is slightly larger than the one found experimentally for bulk GaAs (5.65\AA) and the one predicted for (CrAs)₂/(GaAs)₂ double monolayers (5.69\AA) [99].

As generally half-metallic ferromagnets are sensitive to different lattice constants, we performed additional calculations with the GaAs-lattice constant (5.65\AA) found in experiment. For these calculations we used 84 \mathbf{k} -vectors in the irreducible part of the Brillouin-zone which corresponds to 287 \mathbf{k} -vectors in the full Brillouin-zone.

We performed calculations for (CrAs)₁/(GaAs)₁ to study whether still interface states are present for this lattice parameter, and for (CrAs)₃/(GaAs)₃ to investigate whether there exists still a gap in the minority spin density of states. The results are shown in Fig.3.22 and Fig.3.23 for (CrAs)₁/(GaAs)₁ and (CrAs)₃/(GaAs)₃, respectively.

For the stacked monolayers, (CrAs)₁/(GaAs)₁, a common global shift of the density of states to lower energies by about 0.1eV is seen in the LSDA-results. There are still interface states present at the Fermi-energy and the width of the gap is slightly reduced as the states above the Fermi-energy in the minority spin channel are located closer to the Fermi-energy, while the onset of states below energy stays unchanged. In the majority spin channel the states below the Fermi-energy are shifted also to lower energies, while the states at the Fermi-energy stay unchanged and the states above the Fermi-energy experience a slight shift to higher energies. Overall, the results are almost identical to the results using the 5.75\AA lattice constant. The results from LDA+DMFT are a little more complex. They show differences in spectral weight, most notably for the peak located at about -1eV in the majority spin channel. The

states in the majority spin are not commonly shifted as in the LSDA-results. In the minority spin, the spectral weight of the states at the Fermi-energy is considerably enlarged and the states located above the Fermi-energy at about 1eV are shifted by about 0.2eV closer to the Fermi-energy. However, also the results from LDA+DMFT for this smaller lattice constants leave half-metallic ferromagnetism intact.

While the gap of $(\text{CrAs})_1/(\text{GaAs})_1$ is rather large in comparison, the situation for $(\text{CrAs})_3/(\text{GaAs})_3$ is much different; in this case the gap seen in the LSDA-results is already very small for 5.75\AA and restricted to a small region at the Fermi-energy. It is interesting to note that the results for the smaller lattice constant, 5.65\AA , do experience the same shift as observed in $(\text{CrAs})_1/(\text{GaAs})_1$, but the gap itself is almost unaffected. Although the states above the Fermi-energy in the minority spin are shifted closer to the Fermi-energy, the shift almost completely vanishes at the Fermi-energy. Consequently, spin polarization is almost unaffected. The results from LDA+DMFT are similar and show also a common global shift and its magnitude is comparable to the one seen in the LSDA-results. Of bigger importance is however the fact that the gap in the minority spin channel is affected. More importantly, the minority spin gap is affected by this shift; in the LDA+DMFT results the gap is essentially closed for this lattice constant.

Calculations for $(\text{CrAs})_1/(\text{GaAs})_1$ and $(\text{CrAs})_3/(\text{GaAs})_3$ using the experimental GaAs-lattice constant (5.65\AA) showed only an overall slight shift of the density of states of about 0.1eV closer to the Fermi-energy.

Low-energy spin polarization

To investigate the magnitude of spin-polarization that can be expected from these heterostructures and to investigate the consequences of the correlation induced modification of majority and minority spectral weight at the the Fermi energy, we turn to the issue of the spin polarization. This is given by the expression

$$P(E) = \frac{N_{\uparrow}(E) - N_{\downarrow}(E)}{N_{\uparrow}(E) + N_{\downarrow}(E)},$$

with $N_{\sigma}(E)$ being the spin-resolved density of states, and is plotted in Fig. 3.24 as a function of energy E measured with respect to the Fermi-level. A gaussian broadening of 0.4eV was used to account for a common experimental resolution.

From these results one finds that spin polarization calculated with LSDA ranges from about 70% for $(\text{CrAs})_1/(\text{GaAs})_1$ to about 50% for $(\text{CrAs})_5/(\text{GaAs})_5$. While the spin polarization decreases steadily while increasing the number of monolayers from $(\text{CrAs})_1/(\text{GaAs})_1$ to $(\text{CrAs})_2/(\text{GaAs})_2$ to $(\text{CrAs})_3/(\text{GaAs})_3$, no further decrease can be seen for $(\text{CrAs})_5/(\text{GaAs})_5$. This indicates that the spin polarization reaches a saturation limit of about 50% for $(\text{CrAs})_3/(\text{GaAs})_3$. This is in agreement with the finding that with $(\text{CrAs})_3/(\text{GaAs})_3$ the infinite number of layers is practically reached.

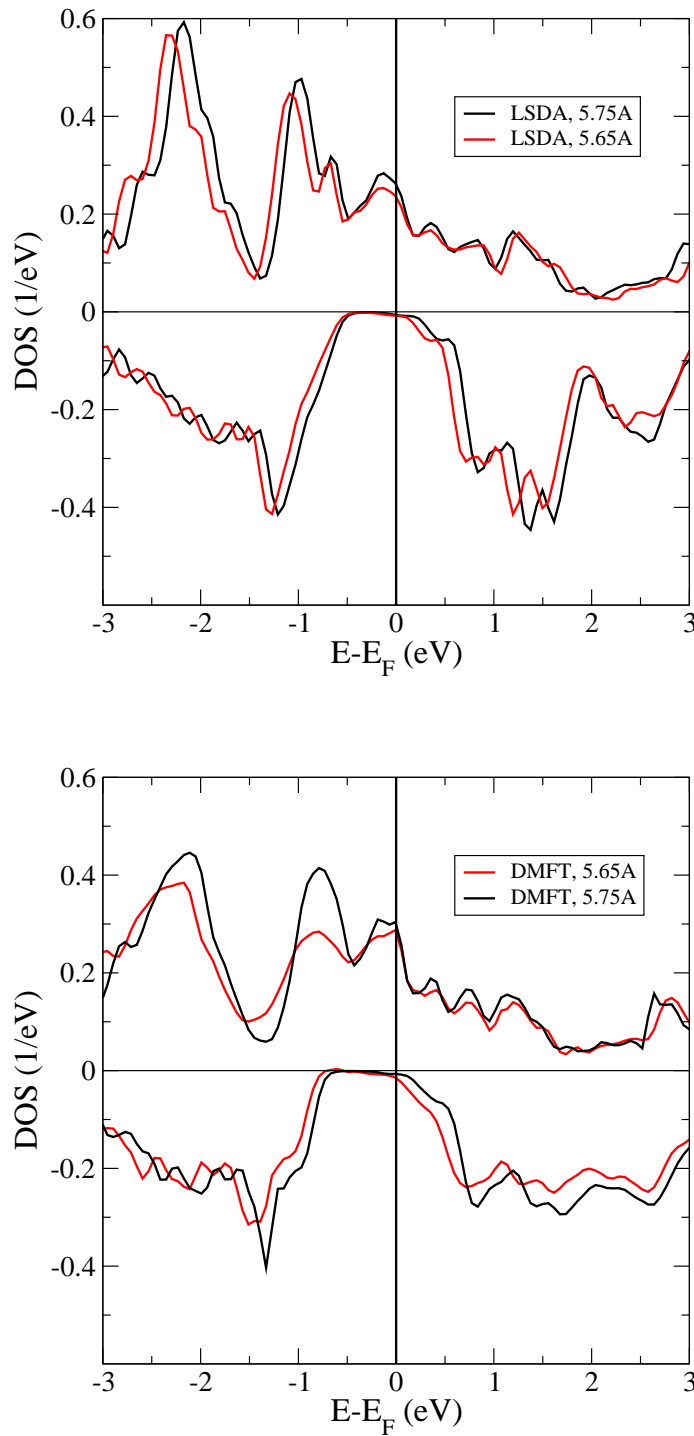


Figure 3.22: Density of states calculated with LSDA (left) and DMFT (right) for $(\text{CrAs})_1/(\text{GaAs})_1$ using different lattice constants: black denotes the lattice constant obtained from an optimized spin GGA-calculation [4] ($a_0 = 5.75\text{\AA}$), results shown in red use GaAs-lattice constant found in experiment ($a_0 = 5.65\text{\AA}$).

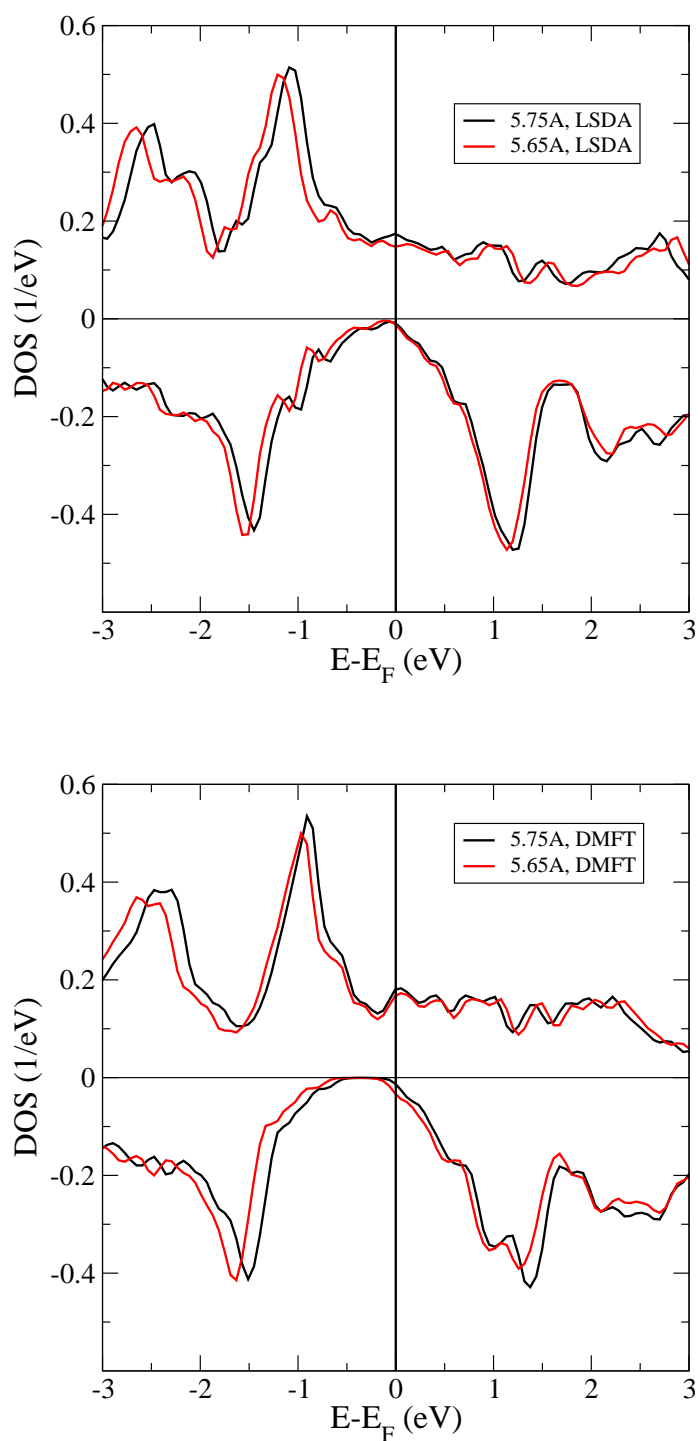


Figure 3.23: Density of states calculated with LSDA (left) and DMFT (right) for $(\text{CrAs})_3/(\text{GaAs})_3$ using different lattice constants: black denotes the lattice constant obtained from an optimized spin GGA-calculation [4] ($a_0 = 5.75 \text{ \AA}$), results shown in red use GaAs-lattice constant found in experiment ($a_0 = 5.65 \text{ \AA}$).

The results from LDA+DMFT are similar despite the large differences in the corresponding density of states. Overall the spin polarization is higher, ranging from about 75% for (CrAs)₁/(GaAs)₁ to 55% for (CrAs)₅/(GaAs)₅. From the LDA+DMFT results the decrease in spin polarization with increasing number of monolayers is even more evident, however the value at the Fermi-energy also saturates at 55% for (CrAs)₃/(GaAs)₃. Although (CrAs)₅/(GaAs)₅ has in comparison to (CrAs)₃/(GaAs)₃ a significantly lower spin polarization slightly below the Fermi-energy, both heterostructures show the same spin polarization at the Fermi-energy.

3.3.6 Summary

Halfmetallic ferromagnetism is surprisingly strong in this material. The results from both employed methods, LSDA and LDA+DMFT, show that halfmetallicity is preserved for multilayers of up to five monolayers of each CrAs and GaAs. Although these multilayers are perfectly ordered, it was also shown [99] that halfmetallicity is not affected by specific forms of disorder similar to atomic diffusion between layers.

Summarizing, the results from both LSDA and LDA+DMFT show that the minority spin gap decreases with increasing number of monolayers. (CrAs)₁/(GaAs)₁ is however not the most promising candidate for real devices as the results show formation of interface states in the gap and a strong peak in the majority spin channel indicating localization of the Cr-*d* electrons: therefore (CrAs)₁/(GaAs)₁ might not be a good conductor. The results for (CrAs)₂/(GaAs)₂ show a minority spin gap of about 0.5eV in LSDA and a gap of about 0.8eV in the LDA+DMFT results. The spin polarization is of similar magnitude as for (CrAs)₁/(GaAs)₁. For (CrAs)₃/(GaAs)₃ and (CrAs)₅/(GaAs)₅ the results show a further decreased minority spin gap and a reduced spin polarization. In addition, as the study of a smaller lattice parameter shows, the gap for (CrAs)₃/(GaAs)₃ and likely also for (CrAs)₅/(GaAs)₅ is sensitive to the lattice constant which is a further complication in practical realization.

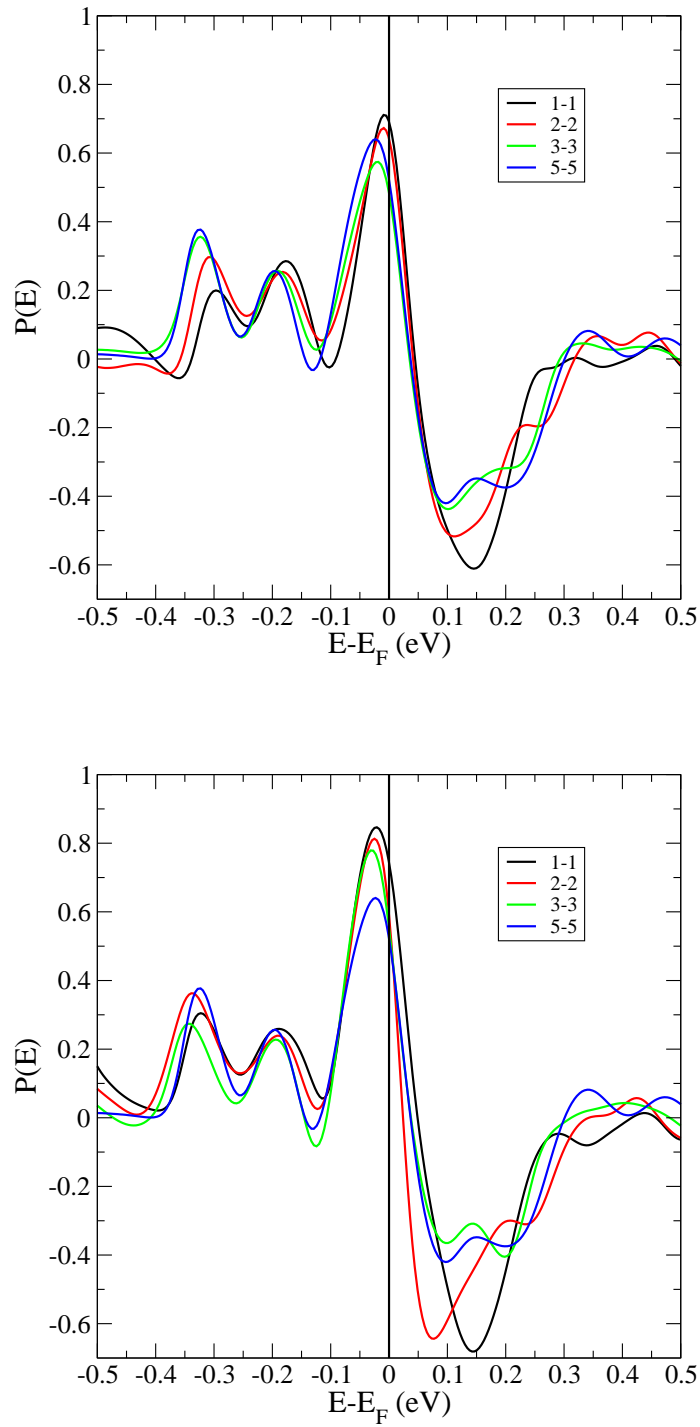


Figure 3.24: Energy-dependent polarization obtained from LSDA (top) and LDA+DMFT (bottom) for $(\text{CrAs})_n/(\text{GaAs})_n$ for $n = 1, 2, 3, 5$.

3.4 Almost a Mott-Hubbard insulator - TiN

3.4.1 Introduction

Transition metal-nitrides have been studied for several decades due to their appealing properties, such as ultra-hardness, high melting point and high Curie-temperature. This combination of physical and chemical characteristics makes them particularly suitable for coating applications. These materials exhibit metallic conductivity and some of them even show superconductivity, as for example the Nb based carbonitride [102] which has a transition temperature of 18K. Recent low-temperature transport properties of thin TiN superconducting films [103] show a disorder-driven transition from a superconductor to an insulating phase in which superconducting correlations persist. These experiments were performed on homogeneously disordered TiN films and clearly demonstrate the important role of electronic correlations. For these reasons, one can expect that signatures of many-body effects might be also present in bulk, stoichiometric TiN.

Electronic properties of bulk transition metal nitrides have been investigated using X-ray Photoelectron Spectroscopy (XPS) [5, 104], Ultraviolet Photoemission Spectroscopy (UPS) [105], X-ray emission [106], Bremsstrahlung-Isochromat Spectroscopy (BIS) [107], and Electron-Energy-Loss Spectroscopy (EELS) [108, 109]. A number of optical reflectivity measurements have also been carried out [110, 111]. On the theoretical side, a large number of band structure calculations using density functional theory (DFT) - mostly within the local-density-approximation (LDA) - is present in the literature [112, 113, 114, 5]. From the LDA-results bonding is described in terms of (i) a *metallic* contribution giving a finite density of states at the Fermi level, (ii) a *ionic* contribution caused by the charge transfer from the metal to the non-metal atom, and (iii) a *covalent* contribution due to the interaction between the non-metal p and the metal d valence states in addition to the (iv) *metal-metal* interactions. In the case of TiN, it is believed that bonding is mostly covalent in origin. However, while the LDA results for the occupied part of the density of states show a good agreement with spectroscopic data *at high binding energies*, they fail to describe correctly the energy range in the vicinity of the Fermi-energy (see, e. g., Fig. 3.26) where predominantly Ti-3*d* states are present [115, 116, 6]. In particular, a suppression in the XPS spectrum over a range of energy down to $\approx 1\text{eV}$ below the Fermi-energy, could be explained so far only by means of an artificial broadening, whose parameters are optimized to fit the experimental data. With our results, we present an alternative view and argue that this suppression can be naturally explained in terms of correlation effects, and, specifically, by the proximity to a Mott metal-insulator transition.

Recent developments in the methodology of electronic-structure calculations allow to go beyond the LDA and include *electronic correlation* effects, which are particu-

larly important for electrons in d or f orbitals. The simplest mean-field extension of LDA is the LDA+U approach [28]. However, as we show below, even such extension is not sufficient to improve the agreement with experiments in TiN. For this reason, it is necessary to go beyond the mean-field approach and to appropriately deal with *dynamical* correlation effects, we do this by applying the Variational Cluster Approach.

3.4.2 Electronic structure calculations for TiN

TiN crystallizes in the rock-salt (B1) structure where Ti and N atoms are sitting on interpenetrating face-centered cubic lattices originating at $(0, 0, 0)$, and at $(\frac{1}{2}, \frac{1}{2}, \frac{1}{2})$ in units of the lattice parameter $a = 7.65a_0$ ($a_0 =$ Bohr radius), respectively. Each Ti (N) atom has six N (Ti) nearest neighbors in an octahedral geometry. Fig. 3.25 shows the conventional unit cell containing Ti (large spheres, red) and N (small spheres, blue) atoms.

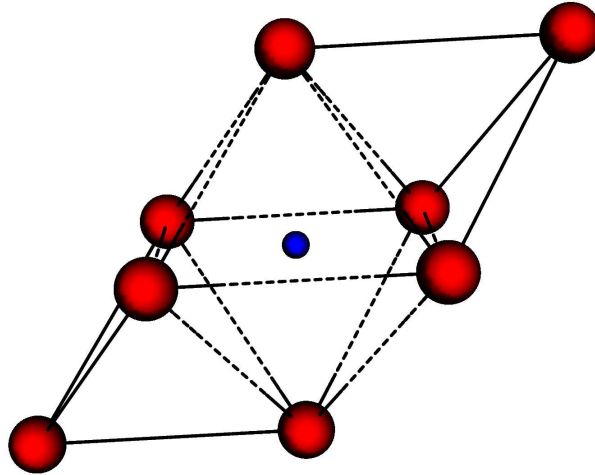


Figure 3.25: Octahedral environment formed by the Ti-atoms (large, red spheres) around the N atom (small, blue sphere). The unit cell is represented by the black lines; the subset of Ti-atoms connected by dashed lines shows the cluster geometry that was used as reference system for the LDA+VCA-calculation (see text).

The electronic configuration of the outer shell of Ti is $4s^2 3d^2$. Therefore, following from the formal oxidation Ti^{3+} , there is a single Ti electron in the valence band. Due to the octahedral symmetry, the Ti- d -orbitals are split into the three t_{2g} orbitals at

lower energy, and two e_g orbitals at higher energy.

The LDA band structure of TiN was computed with the LDA-LMTO (ASA) code [117] which uses the basis of linearized muffin-tin orbitals in the atomic sphere approximation. Two empty spheres per unit cell have to be introduced at the positions $(\frac{1}{4}, \frac{1}{4}, \frac{1}{4})$ and $(\frac{3}{4}, \frac{3}{4}, \frac{3}{4})$. Results are shown in Fig. 3.26. In the density of states, the N- s orbital (not shown) form the lowest valence band widely separated from the other valence bands. At higher energies, one finds the set of bands formed by N- p orbitals situated between -10 and -4eV. Finally, the last five bands mainly consist of Ti- d orbitals. The DOS around the Fermi level is dominated by Ti- t_{2g} bands, while Ti- e_g bands remain above the Fermi level and are empty. Ti- t_{2g} and Ti- e_g bands overlap in the unoccupied part of the spectrum. Below Fermi-energy the hybridization of Ti- d orbitals with N- p orbitals is at the origin of the covalent bonding.

Concerning the $p-d$ hybridization, the energetically higher d -bands form the anti-bonding states while the lower p -bands form the bonding states. The position of the Fermi level (E_F) is determined by the number of valence electrons per unit cell being equal to 9.

We evaluate values of the Coulomb-interaction U and Hund's rule coupling J parameters acting between the Ti- t_{2g} -electrons from first principles by means of a constrained LSDA method [118, 58]. For TiN - as is discussed in more detail in the next section - we obtained large values of $U = 10\text{eV}$ and $J = 1.3\text{eV}$ from constrained LDA.

As constrained LDA is also for other reasons [119] criticized to provide too large values for U , we study a range of U -values and compare the results to experimental data.

In order to take into account correlation effects on a mean field-level, we carried out an LDA+ U calculation. As one can see in Fig. 3.26 there are no significant differences between the LDA and the LDA+ U results despite the large value of U . However, a comparison of these calculations with valence band XPS spectra, which provide a measure of the total density of occupied states as a function of energy, shows that neither LDA nor LDA+ U results are appropriate to describe the experimental spectra in the vicinity of the Fermi energy unless one introduces ad-hoc broadening terms. Specifically, while the position of the N- p bands obtained by LDA and LDA+ U is in reasonable agreement with the XPS measurements (see Fig 3.26), both methods fail to reproduce the behavior of the DOS within a range of ≈ 2 eV below the Fermi-energy. In particular, the XPS spectra show a local maximum at energies of $\approx -1\text{eV}$, followed by a "pseudo-gap"-like suppression at the Fermi-energy. These LDA+ U results do not change qualitatively when decreasing U down to $U \approx 8$, which, as argued below, is more appropriate for this material.

These results suggest that static inclusion of correlations is not sufficient to explain

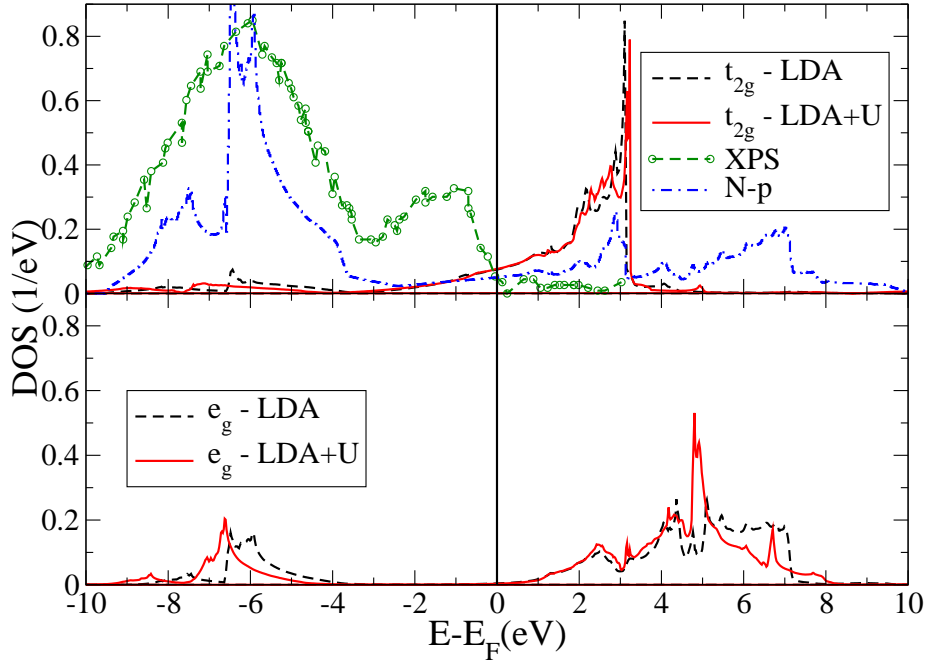


Figure 3.26: Orbital-resolved density of states for TiN obtained by LDA and LDA+U. The upper (lower) panel shows the Ti- t_{2g} (e_g) contribution. The upper panel also displays the N- p density of states and the experimental XPS spectrum [5] (Experimental data reproduced with kind permission of the authors).

the DOS near Fermi-energy. For this reason, we have taken into account dynamical correlation effects beyond the LDA-results by means of the LDA+VCA, a method appropriate to treat correlated systems.

3.4.3 Model and realistic parameters for the Coulomb interaction

In order to limit the size of the Hilbert space, it is necessary to use an effective Hamiltonian describing a small number of correlated effective orbitals per lattice site in the close vicinity of the Fermi level. From Fig. 3.26, we conclude that the minimal model for TiN has to be restricted to Ti-(t_{2g}) bands, while higher Ti-(e_g) bands are unoccupied and can be neglected.

In order to construct the effective low-energy Hamiltonian to use in our LDA+VCA calculation, we employ the NMTO-technique to calculate the non-interacting part of the Hamiltonian, as outlined in chapter 2.2. Following the discussion in Sec. 2.2.1, the minimal basis set is obtained by downfolding to the $Ti-d(t_{2g})$ manifold. To optimize the overall agreement with the energy bands, we chose the following expansion points

$E_\nu - E_F = 1.512\text{eV}$, 0.016eV , and -0.664eV . Results are quite stable for choices of the E_ν around these values.

In Fig. 3.27 we show the eigenvalues of the effective Hamiltonian along some high-symmetry directions in direct comparison to the bands obtained from the full orbital basis. From this figure it is clear that the Ti- $d(t_{2g})$ manifold is well described by the non-interacting part of the effective Hamiltonian.

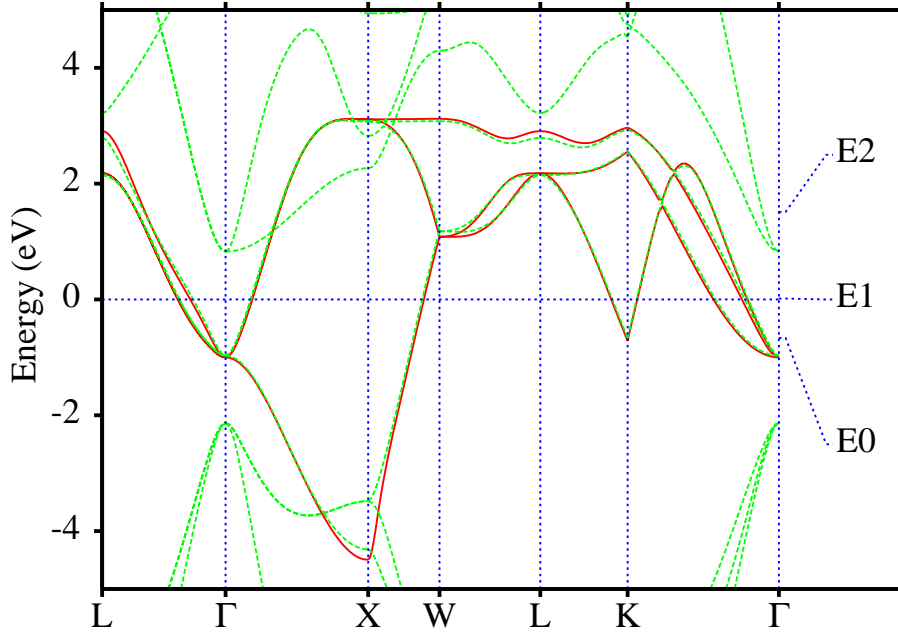


Figure 3.27: Band structure of TiN calculated for a path in the Brillouin zone (BZ) going from the **L**-point (0.5, 0.5, 0.5) through the Γ (0, 0, 0), **X** (0, 1, 0), **W** (0.5, 1, 0), **L** (0.5, 0.5, 0.5), **K** (0, 0.75, 0.75) points and ending at the Γ point (0, 0, 0). The bands shown as dashed/green lines are obtained from the LDA calculation for the complete orbital basis set. The NMTO bands (full/red line) are obtained after downfolding to the Ti- $3d(t_{2g})$ orbitals.

As the non-interacting Hamiltonian of TiN is rather simple in comparison to CrO_2 , which has two nonequivalent Cr-sites, and to NiMnSb , where a very large number of hoppings occur as Ni- d and Mn- d orbitals form the basis set, it will be presented as example in the following.

In the chosen NMTO basis, m is labeled by the three Ti- t_{2g} orbitals $m = xy, yz, zx$ (we use this order for the definition of the matrix elements below). In this basis, the on-site matrix elements $t_{m',m}^{000}$ are diagonal and independent of m . The precise value of these terms, as well as the double-counting correction, are not important as they can be absorbed into the chemical potential. The directional hopping matrix elements

up to second nearest-neighbor are given by

$$t_{m',m}^{\frac{1}{2}\frac{1}{2}0} = \begin{pmatrix} -0.66 & 0 & 0 \\ 0 & 0.15 & -0.1 \\ 0 & -0.1 & 0.15 \end{pmatrix},$$

$$t_{m',m}^{100} = \begin{pmatrix} -0.23 & 0 & 0 \\ 0 & 0.01 & 0 \\ 0 & 0 & -0.23 \end{pmatrix},$$

in units of eV. Only one representative hopping integral is shown for each class. Other hopping terms can be derived from proper unitary transformation using crystal symmetry. See, e.g., Ref. [120] for details.

Further hoppings are taken into account up to a range of $r = 1.1a$. Neglected hoppings are at least by a factor 40 smaller than the largest nearest-neighbor hopping.

In order to make sure that neglecting the Ti- e_g orbitals is safe, we have also carried out a LDA+VCA calculation (for smaller clusters) using an Hamiltonian downfolded to *all five* Ti- d bands. We have verified that the occupation of the Ti- e_g bands is less than 10^{-3} electrons per Ti-atom, so that the corresponding Wannier-functions can be safely neglected in our calculation. Notice, however, that due to hybridization the Ti- t_{2g} Wannier functions have also a certain amount of Ti- e_g character.

For the interaction part of the Hamiltonian we use accordingly the t_{2g} -subset of the full U-matrix as described by Eq. (2.24). For this subset, the Coulomb-interaction between the Ti- t_{2g} electrons is independent of the orbital indices of the involved electrons.

The values for the Coulomb-interaction U and Hund's rule coupling J parameters acting between the Ti- t_{2g} -electrons we calculate from first principles by means of a constrained LDA method [118, 58]. While this method is not very accurate, and may produce slightly different values depending on its exact implementation, it is a useful tool to derive the values for the interactions from first principles. For TiN, we obtain large values of $U = 10\text{eV}$ and $J = 1.3\text{eV}$ from constrained LDA, whereby occupancies on all Ti- d orbitals have been fixed. Since the Ti- e_g effective orbitals are essentially empty, as discussed above, they do not contribute to screening and can be safely neglected.

In a discussion with O. K. Andersen a reason for this unexpected high value for the Coulomb-interaction U became clear. In the elemental metal Ti one finds a Coulomb-interaction U of about 4eV for the electrons in the Ti- d orbitals. However, for electrons in the Ti- d orbitals of TiN, a U of about 10eV is obtained. This large difference originates from significant changes that occur in chemical bonding: the Ti- d orbitals in elemental Ti have bonding character and neighboring wave functions overlap such that they add with the neighboring wave function centered on the next lattice site. This is in contrast to TiN, where the $p - d$ hybridization causes anti bonding character of the Ti- d orbitals which in turn leads to the fact that neighboring

wave functions do not add, but have a node at the center and change sign. Within constrained LDA this means that U is overestimated, as less electrons contribute in screening the Coulomb-interaction and less screening causes a larger U .

The constrained calculation yields a value of $U \approx 10\text{eV}$ and $J \approx 1.3\text{eV}$. However, as it was shown by Aryasetian et al [119], constrained LDA gives larger values for U and J compared to other methods based on the evaluation of the screened Coulomb interaction within the Random Phase Approximation [121]. Therefore, we have also investigated smaller U values. While the results from LDA+VCA do not depend dramatically on J , we show in the next section that results change drastically around $U \approx 9\text{ eV}$, where a Mott-insulator transition takes place.

As correlations on a mean-field level are already included in LDA, one should in principle subtract the discussed double-counting [29, 32] correction. However, since the Ti- t_{2g} orbitals are degenerated, this correction yields only a constant that can be absorbed in the chemical potential (see also section 2.3.3 for more details to the double counting correction in this specific case).

3.4.4 Results - Density of states

As discussed in Sec. 3.4.2, the low-energy XPS [5] spectrum is characterized by a peak at about -1 eV followed by a “pseudogap”, i. e. a suppression of states at the Fermi level. This latter fact is consistent with the K-ELNES spectrum [122], which provides information about the DOS above the Fermi energy (see Fig. 3.29). This suppression is not reproduced by LDA electronic structure calculations, suggesting that strong electronic correlations may play an important role for this material. In a previous work [5], it was suggested, in order to improve the agreement with the measured spectra, to convolute the computed DOS with a combination of a Lorentzian and a Gaussian curve, to take into account the broadening due to lifetime and experimental resolution effects. This treatment indeed improves on the overall shape producing a peak at an energy of about -1.5 eV , although one should point out that the fitted broadening parameters are much too large (around 0.6 and 0.8eV , respectively).

From our work, we argue that the pseudo-gap observed in the DOS of stoichiometric TiN is intrinsic to this material and signals the proximity to a Mott metal-insulator transition. To show this we start by calculating the DOS within LDA+VCA using the Hamiltonian discussed in the previous section with the value of $U = 10\text{ eV}$ obtained from constrained LDA. The results, displayed in Fig. 3.28, predict for this value of U a Mott-insulating state with a gap of about 1eV . However, this is in contrast to the experimental situation, since electrical conductivity in TiN shows a metallic behavior, although with a relatively low residual conductivity [123]. Since results obtained from constrained LDA are only approximate and tend to overestimate U due to the delocalized nature of Wannier orbitals, we also present results for

smaller values of U down to 8eV (Fig. 3.28). As one can see, no significant changes can be detected for states more than 3eV away from the Fermi-energy. Here, only static correlations, which get absorbed into the chemical potential, play a role. In contrast, the situation changes rapidly around the Fermi-energy. In particular, our results show that the Mott gap starts closing at $U \approx 9\text{eV}$, and at smaller U down to $U \approx 8\text{eV}$ it acquires the shape of a pseudo-gap. As a matter of fact, the density of states calculated for $U = 8.5$, shown in Fig. 3.29, agrees quite well with experimental measurements. Notice that, in order to avoid introducing *ad-hoc* parameters, and to show fine-detailed features of the spectrum, the calculated curve has not been additionally broadened to meet experimental resolution. Taking this into account, we see that our results reproduce quite well the experimental features both above (K-ELNES) and below (XPS) the Fermi-energy, and in particular the “pseudo-gap” behavior between -1.0 and 1.0eV .

We want to remind that we are using an effective low-energy model which is expected to correctly reproduce correlation effects close to the Fermi energy, but is not expected to reproduce features beyond the range of the NMTO bands shown in Fig. 3.27 (full/red curves). To reproduce the spectrum at higher binding energies, LDA and LDA+ U are more appropriate. In this sense, our results complement these techniques in the low-energy region.

In addition, the computed LDA+VCA density of states spectra show a set of peaks in the energy range of -5 to -3eV . These states only appear when a sufficiently large cluster is taken as a reference system. Therefore, these states can be seen as non-local many-body incoherent features. It is tempting to associate these states with the corresponding “kink” in the XPS spectrum [5] at energies around -4eV . However, this kink is also affected by the presence of N- $2p$ states whose bands start at $\approx -4\text{eV}$ (see Fig. 3.26). Therefore, our result suggests a strong hybridization between these states and the correlated many-body structures at $\approx -4\text{eV}$.

The nitrogen K-ELNES spectrum is related to the unoccupied partial density of states with p -symmetry at the nitrogen site. The peaks situated at energies around 2 and 4eV can be attributed to the unoccupied N- $2p$ states hybridized with Ti $3d$ states. Notice that the downfolded operators used in our effective Hamiltonian (2.8)+(2.24) describe anyway an effective particle ultimately producing the bands of Fig. 3.27, i.e. the corresponding particle also contain a “mixture” of other orbitals such as Ni- p , in order to correctly reproduce the hybridization. It is remarkable to note that our calculation with $U = 8.5\text{eV}$ captures most of the features of the experimental spectra at both peaks, in particular the separation of the two peaks is in very good agreement with the experimental value 2.3eV [6].

It is important to mention that combining the experimental data from the occupied and unoccupied parts of the spectra with electric and magnetic properties of TiN

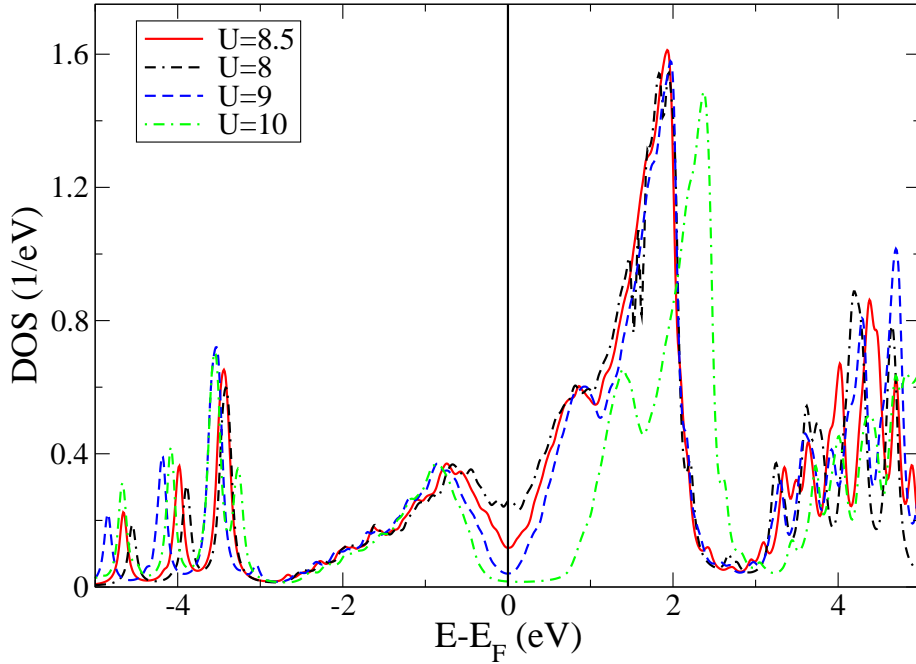


Figure 3.28: TiN density of states calculated with LDA+VCA for different values of the Coulomb-interaction parameter U and for the Hund's rule coupling $J = 1.3$.

[123], a peculiar metallic behavior emerges. Magnetic susceptibility measurements show that TiN is a Pauli-paramagnet, and electrical conductivity demonstrates a metallic behavior with a relatively large residual resistivity. In combination with the measured XPS spectra, one can conclude that at the Fermi level a pseudo gap in the density of states is formed, signaling the vicinity of a Mott-insulating phase.

The present LDA+VCA calculation includes correlation effects exactly on a length scale of an octahedral cluster consisting of six sites as shown in Fig. 3.25 (atoms connected by dashed lines). Notably the results of our present calculations give the correct description of the -1eV peak and the double peak in the occupied part of the spectra. In addition, at lower energies, many-body non-local incoherent features are formed which can explain the kink in the XPS spectra situated at -4eV . Therefore, it is clear that the present LDA+VCA results show notable improvements with respect to previous DFT-results in the low-energy region, and explain the peculiar metallic behavior of TiN.

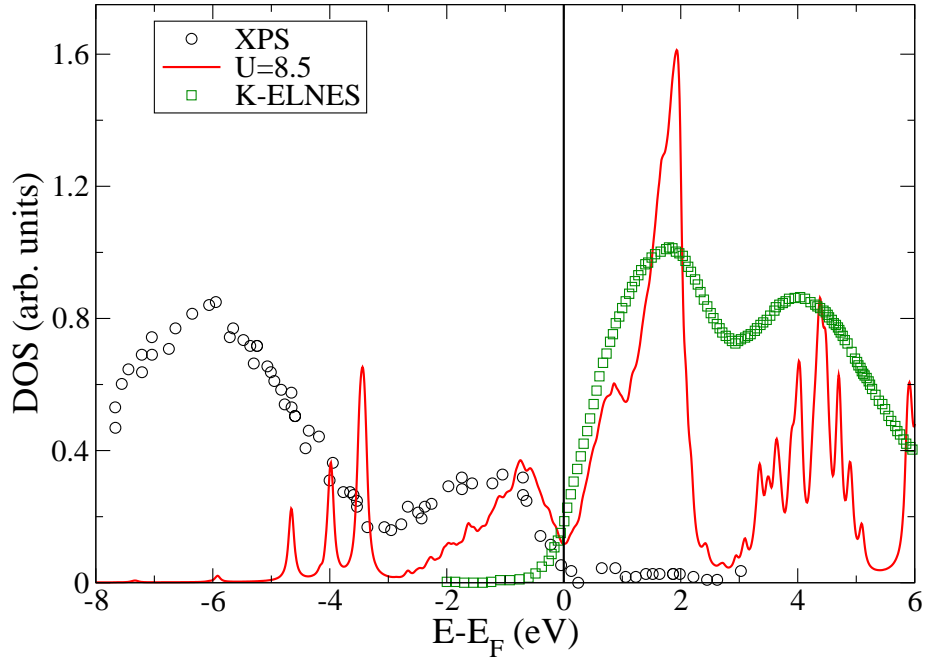


Figure 3.29: TiN density of states calculated within LDA+VCA for $U = 8.5\text{eV}$ and $J = 1.3$ compared with measured XPS [5] and K-ELNES [6] spectra (Experimental data reproduced with kind permission from the authors).

Non-local correlations and cluster geometry

For the LDA+VCA results that we discussed so far, an octahedral reference cluster was chosen (Fig. 3.25) in order to conserve the lattice symmetry. This is needed, as we have verified that in smaller clusters, without the lattice symmetry, this non-local feature is not present.

While the geometry of the reference system always has some effect on the results, TiN shows a particularly dramatic dependence which goes beyond what is usually obtained (see for a more usual scaling behavior also Appendix D). The reason for this, as will be outlined below, are non-local correlation effects present in TiN.

To investigate the cluster dependence in more detail we carried out a number of calculations. In a first step, only the onsite-energies and correlation terms are kept and all hopping terms are removed (atomic limit). The result from such a calculation using a reference system formed by four sites is shown in Fig. 3.30 and compared to the results from a full calculation (all hopping terms taken into account), conducted for the same reference system.

Comparing the results of this four sites system, it is evident that the hopping terms cause states that mainly add spectral weight to the close vicinity of the peaks

caused by the onsite and correlation terms. For this choice of the cluster geometry, that does not have the same symmetries as the unit cell of the lattice, the results do not show the depression and the novel states at -4eV as seen in Fig. 3.28.

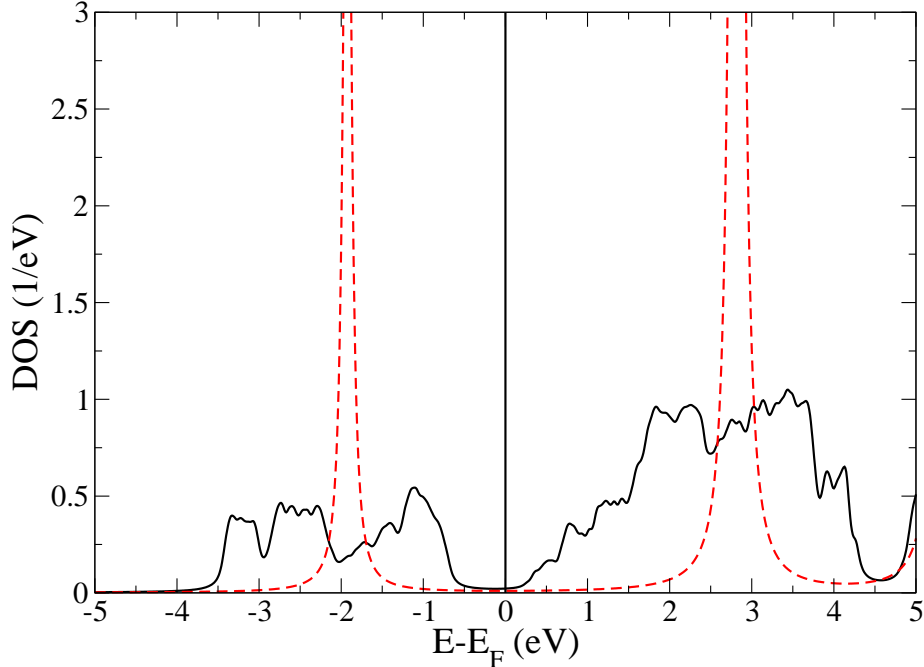


Figure 3.30: Density of states for TiN calculated with a reference system consisting of four sites: shown in black are the results from the full calculation and depicted as red, dashed line the result for the atomic limit at the same value of the chemical potential. For this choice of the reference system the hopping terms included in the full calculation mainly broaden the peaks caused by onsite energies and interaction terms.

It is important to note, that following the discussion in chapter 2.4, the LDA+VCA approach becomes exact in the atomic limit; consequently the result within the atomic limit shown in Fig. 3.30 does not depend on the size of the reference system and is necessarily also obtained using the six sites reference system.

In a next step, we test our assumption that the novel states seen in the result for the six sites reference system (see Fig. 3.28) are indeed caused by non-local correlation effects which can occur only for this (or a comparable) cluster geometry. To this task, we investigate the influence of the CPT-approximation on the calculation and whether the CPT approximation could cause the appearance of these novel states. To do so, we add hopping terms to the atomic calculation of the six sites reference system; these are, however, not treated within the exact diagonalization of the cluster, but only within the CPT approximation. For practical reasons, not all hopping terms

are considered, but only the largest. The result of this calculation is shown in Fig 3.31. It is interesting to note that the treatment of these additional hopping terms within the CPT approximation of the atomic calculation causes merely a broadening of the states caused by onsite and correlation terms; the result is very similar to the result of the full calculation for the smaller, four sites calculation which is shown as reference in Fig 3.31.

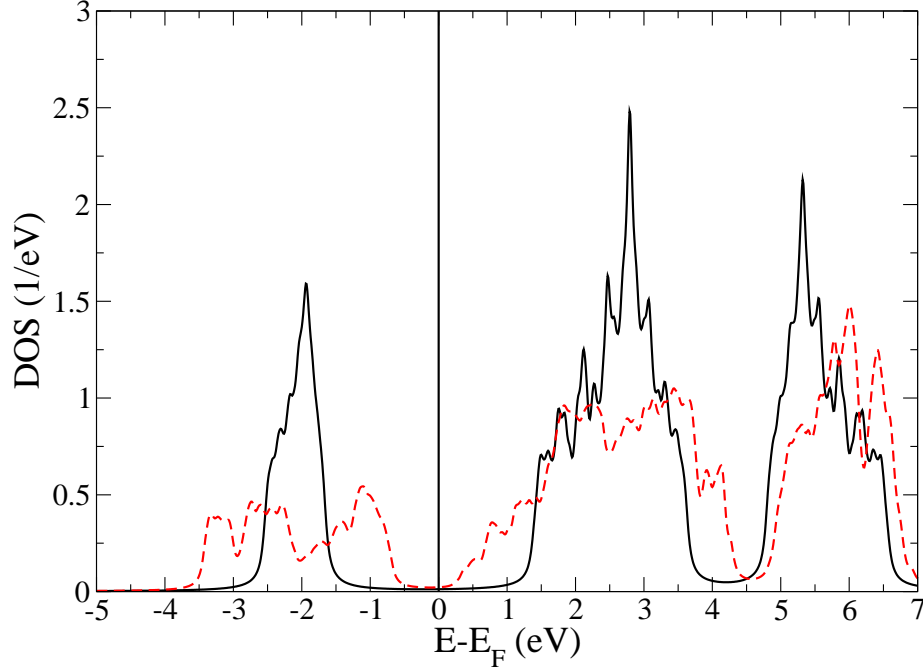


Figure 3.31: Density of states from a six sites calculation with onsite-, correlation-terms and the largest hopping terms treated only within the CPT approximation (black solid line); in comparison the result from a full calculation for the four sites reference system is shown as red dashed line.

Though not a definitive proof, the results support our thesis that the novel states appearing in the (full) six sites calculation, shown in Fig. 3.28, are caused by non-local correlation effects that become possible only for the reference system that shares the same symmetries as the underlying lattice. It would be interesting to investigate their origin in more detail, however for a more thorough analysis the number of hopping terms in the calculation is impractically large.

However, non-local real space effects cause \mathbf{k} -dependent states in reciprocal space; therefore, one expects to find interesting features in the self-energy.

Finally, a remark should be made concerning vacancy effects. It is well known that transition metal carbides and nitrides usually contain vacancies in the metalloid (N)

sub lattice. The presence of vacancies profoundly influences the physical properties of this family of compounds. It is known from electronic-structure calculations that the presence of vacancies reduces the partial nitrogen s and p density of states, and produces additional peaks close to the Fermi level. These *vacancy peaks* show up in the LDA-DOS of non-stoichiometric TiN at about -2eV and in the vicinity of the Fermi level [124, 115, 116, 125]. The peak at -2eV is associated with σ -bonding between Ti atoms through the N vacancy, while the peak at E_F is related to the σ -bonding between the nearest-neighbor Ti atoms [124, 115]. A quantitative comparison of the measured spectra and the broadened density of states obtained for non-stoichiometric materials shows that the calculated density of states peaks are too narrow and shifted to lower binding energies with respect to experimental results. The shift and the narrowing of the theoretical peaks was interpreted [126] as due to limitations of the local density approximation in describing electronic interactions.

3.4.5 Spectral properties

In order to gain insight into \mathbf{k} -dependent features of the local DOS, we have computed the \mathbf{k} -resolved spectral function $A(\mathbf{k}, \omega)$, which is plotted in Fig. 3.32. From this figure one can clearly discern two metallic bands crossing the Fermi-energy near to the \mathbf{W} point, and one between \mathbf{K} and $\mathbf{\Gamma}$, however, with a small spectral weight, consistent with the pseudo-gap picture discussed in Sec. 3.4.4.

In the energy range between -3 to -5eV the spectral function in Fig. 3.32 shows a dispersionless feature, which is responsible for the non-local correlation peaks in the same energy range also discussed in the previous section.

As discussed in connection with the density of states, this feature cannot be captured within a single-site LDA+DMFT approach, so that a cluster approach, as the one presented here, is required.

3.4.6 Self-energy

As discussed above, our calculations show that dynamical correlation are important for TiN. On the other hand, it turns out that also *non-local* correlations are crucial.

To show this, we plot in Fig. 3.33 the self-energy on the same path around the BZ as for the spectral function (Fig. 3.32). As real and imaginary part of the self-energy are not independent from each other, dispersive structures appear in both at comparable energies. The plot of the real part of the self-energy gives an overview and covers a large energy window that is identical to the density of states plot. The imaginary part is shown for a smaller window around Fermi-energy to show the dispersive features in more detail. As one can see from the plots, there is a strong \mathbf{k} dependence, especially in the region around the Fermi-energy. This is an indication for the non-locality of the self-energy. This non-locality strongly affects the metal-insulator transition as well, since the most dispersive part of Σ is precisely

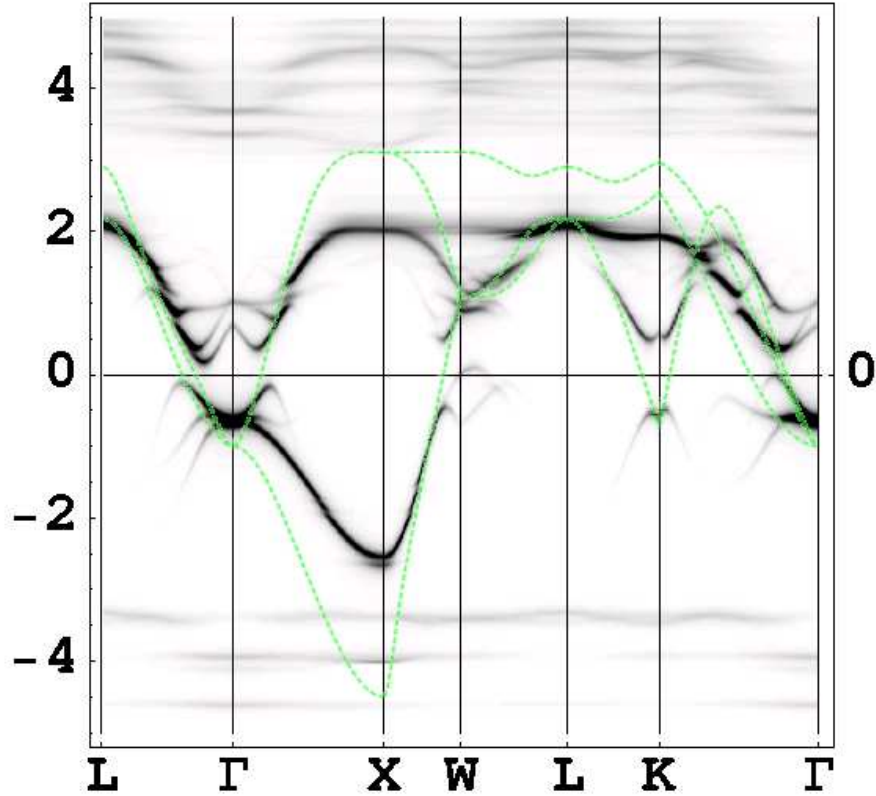


Figure 3.32: Spectral-function of TiN for $U = 8.5$ and $J = 1.3$ shown as density plot for the same path in the BZ as in Fig. 3.27. The bands obtained from downfolding (dashed, green lines) are shown as reference.

around the Fermi energy. Further, there are contributions to the self-energy at larger energies (shown in Fig. 3.33), which, however, are essentially flat as a function of \mathbf{k} , and, thus, localized in real space.

3.4.7 Effective mass

The \mathbf{k} -resolved spectral function allows us to determine the LDA+VCA quasiparticle bands, which are shown as density plot and are compared to the (dashed) bands obtained from LDA. One can observe a reduction of the quasiparticle bandwidth from approximately 7.5 eV in LDA to 4.5 eV in LDA+VCA. Accordingly, the band narrowing due to correlation effects can be described in terms of a “high-energy” (HE) mass-renormalization factor $m_{HE}/m_{HE,LDA} \approx 1.7$.

Further, we evaluate the (low-energy, LE) effective mass also from the self-energy

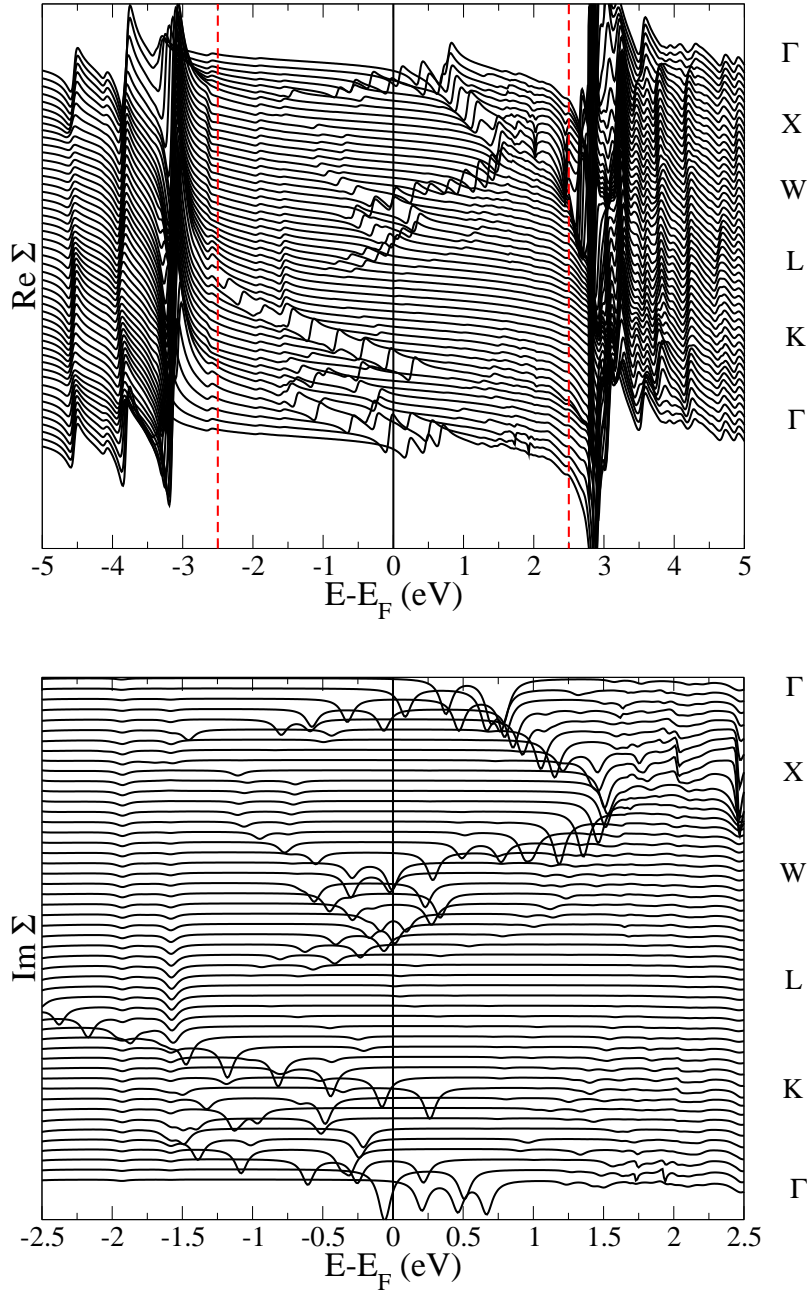


Figure 3.33: Real (top) and imaginary part (bottom) of the self-energy calculated for the same parameters and along the same BZ path as for the spectral-function in Fig. 3.32. As real and imaginary part of the self-energy are not independent from each other as described by the Kramers-Kronig relations, we use the plot of the real part (top) to give an overview over a large energy range (identical to the density of states plot in Fig. 3.28) and the plot of the imaginary part (bottom) for a smaller energy range to show the region around the Fermi-energy in more detail.

according to the expression

$$\frac{m_{LE}^*}{m_{HE,LDA}} = \left| \frac{1 - \frac{\partial \Sigma(E, \mathbf{k})}{\partial E}}{1 + \frac{\partial \Sigma(E, \mathbf{k})}{\partial E}} \right|_{E=E_F, \mathbf{k}=\mathbf{k}_F},$$

and we obtain after averaging over three different \mathbf{k} -vectors an effective mass of $\frac{m_{LE}^*}{m_{HE,LDA}} = 1.8$.

Experimental measurements provide the total ratio m_{HE}/m_e (m_e is the free electron mass), which contains also the mass renormalization factor $m_{HE,LDA}/m_e$ coming from the band structure. The latter can be roughly estimated by equating

$$m_{HE,LDA}^* = \frac{\hbar^2 k_F^2}{2E_F^{\text{band}}} k_F = \left(\frac{3\pi^2 n}{V} \right)^{1/3}, \quad (3.2)$$

for a single electron, $n = 1$, in the unit cell volume $V = a_0(a_1 \times a_2)$ with the a_i being the unit cell translation vectors. To calculate the Fermi-energy we set the origin of energy to the bottom of the Ti- t_{2g} bands and found $E_F^{\text{band}} = 4.42\text{eV}$. Using these values we find an effective mass of $\frac{m_{\text{band}}^*}{m} = 1.27$ due to band effects, which gives a total effective mass correction to the electron resting mass of 2.2 and 2.3, respectively. These values lie approximately in the middle of the values calculated by other methods. Theoretical estimates of m^* [127] obtained in the literature cover a large range of values from 0.8 to 3.

Despite the good agreement of the high and low energy mass renormalization factors, available experimental measurements discussed below provide an estimate for m_{HE} and not for the low-energy contribution. Experimentally, an estimate of the electron effective mass in TiN has been obtained by UPS and EELS experiments using high-energy synchrotron radiation [128]. These experiments also allow to determine band density n of the Ti- d -electrons and the width of the $3d$ -band E_F . To estimate the Ti- d -electron density several characteristics of the UPS spectrum such as peak area, photoemission cross section and inelastic mean free path are used. The estimation of the d -bandwidth is obtained from the position of the minimum in intensity between the valence and conduction bands [128]. In this case, the computed mass renormalization factors, being 2.2 and 2.3 respectively, are in a reasonable agreement with the value presented in Ref. [128], table 3, sample d, with the value 2.7 ± 0.3 .

3.4.8 Summary

Our results suggest that TiN is a peculiar metal with a pseudo-gap at the Fermi-level indicating the proximity to a metal-insulator transition. In our calculations the pseudo-gap regime is best described for a value of $U = 8.5\text{eV}$ for the Coulomb-interaction.

It is important to mention that this result could be achieved only by an appropriate treatment of dynamical and non-local correlations. In particular, neither LDA nor LDA+U calculations provide even a qualitative description of the DOS suppression at the Fermi-energy. Due to the non-locality of the self-energy, we expect that even single-site DMFT may not be appropriate for a proper description of this system at low energies.

Our calculations provide a good qualitative and semiquantitative agreement with experiments, when comparing the DOS with XPS and K-ELNES spectra close to the Fermi-energy. In particular, our results show a coherent feature situated at -1eV which can be clearly identified in the XPS spectra. We stress that none of previous theoretical investigations are able to capture this particular low energy feature. Furthermore, at low energies our results provide a qualitative interpretation of the -4eV kink in the XPS spectra as an hybridization of incoherent non-local many-body features with the N- p states. Also, in the unoccupied part above the Fermi-level, our results reproduce the double peak structure in good agreement with the K-ELNES spectra.

Finally, we calculated the effective mass from high- and low-energy spectral features and found the values 2.2 and 2.3, respectively, which reasonably agree with values from experiment.

Chapter 4

Summary

Strong correlated systems show a variety of different phases and properties arising from the central property that kinetic and potential energy of the valence electrons are of comparable magnitude. A number of methods has been developed to study these systems, like the Dynamical Mean Field Theory, and each method comes with its own compromises, like in case of DMFT the neglect of non-local correlation effects. It is the aim of this thesis to introduce a new approach that allows to study also systems where non-local correlations play a significant role.

So, in chapter 2, the LDA+VCA method is developed as an intermediate approach for real world compounds. At its heart is the VCA-approach which treats short ranged correlations exactly while long ranged correlations are kept on a mean field level. To investigate real world compounds the VCA-approach is combined with NMTO, a powerful downfolding technique that allows to obtain ab-initio single particle parameters for the material of interest. As employing results from density functional theory within the Hubbard-model leads to a double counting of terms, different correction schemes are discussed. In particular two different schemes are presented, namely the Around Mean Field-scheme and the Fully Localized Limit-scheme, and for a specific case results obtained from both schemes are compared.

It was the original aim of the development of the LDA+VCA approach to investigate compounds consisting of transition metals. Consequently, in chapter 3 results for a number of distinctly different compounds are presented. The range of materials comprises intermediate correlated systems that despite interaction is not so strong experience significant changes by non-local correlations, like in the two half-metallic ferromagnets that is studied, the half-Heusler compound NiMnSb and the oxide CrO₂. An example for a truly strongly correlated system is presented, the nitride TiN.

For NiMnSb, we have shown that non-local correlation effects between *Mn-d* and *Ni-d* states are particularly strong and play an important role for the low energy physics in this material. This follows from the result that the major contribution to the non-quasiparticle states are caused by these non-local correlation effects. These

non-quasiparticle states are crucial to describe spin polarization as can be seen from the good agreement to experimental data. In addition, the importance of the *Ni-d* states in the understanding of NiMnSb is shown by performing calculations with a *Mn-d* only basis and discussing the adherent problems.

In case of CrO₂ we have shown that according to our results the ferromagnetic state is determined by itinerant electrons with a rather large effective mass in contrast to previous results that predicted localized moments. Further, the results from the LDA+VCA approach show the appearance of non-quasiparticle states above Fermi-energy and contribute significantly to a better description of the energy dependent spin polarization as found in experiment.

For the strongly correlated system TiN we could show the presence of both local and non-local correlation effects which show their fingerprint in amongst others the self-energy. Further, we could explain the presence of a pseudo gap in this material with the close proximity to a metal insulator transition. A number of calculations for different strengths of the Coulomb-interaction are performed and the result almost at the Mott-Hubbard transition fits best the experimental data. Concerning the LDA+VCA approach, we discuss for this material the importance of choosing a suitable geometry for the reference system.

Wherever possible, results obtained from LDA+VCA are compared to experimental data and generally we find good to excellent agreement, so that we can be confident that the LDA+VCA approach is a valuable addition to the presently available methods suitable to describe correlated systems.

From the perspective of half-metallic ferromagnets, another special system is studied within this thesis, namely the (CrAs)_{*n*}/(GaAs)_{*n*} with *n* = 1, 2, 3, 5 heterostructures, which are of particular interest due to their structural compatibility to existing semiconductor technology. As bulk CrAs was predicted to be a half-metallic ferromagnet with a Curie-temperature practical for real devices, these heterostructures were developed to circumvent the problem that zinc-blende CrAs is not a stable phase and cannot be grown thicker than thin films of a few monolayers. To study these large systems, the LDA+VCA approach is impractical due to the large number of orbitals necessary to keep within the basis. Therefore, two other approaches are employed, the LSDA to study the results from a mean-field perspective and the LDA+DMFT approach to study effects in the presence of intermediate correlations. A number of calculations were done to study the influence of different correlation strengths and different lattice constants. From the results we find that despite the presence of intermediate correlations and the presence of an interface, the half-metallic gap is conserved throughout with the exception of the monolayer (CrAs)₁/(GaAs)₁, where interface states appear in the minority spin gap. Further, we find that especially the double mono layer structure (CrAs)₂/(GaAs)₂ promises good potential for future applications like efficient spin filters and similar devices.

4.1 Outlook

While many results obtained with LDA+VCA and LDA+DMFT are presented, there are still many things to be desired. While the LDA+VCA is in principle not limited to the ground state, it is currently mostly used as a $T = 0$ method as the use of exact diagonalization requires further increased numerical effort to go to finite temperatures. An alternative solver like quantum monte carlo allows finite temperatures, but at the cost of using the maximum entropy method which brings its own certain amount of uncertainty. In addition, the possible occurrence of the so-called fermion sign problem poses also difficulties. On the other hand, the LDA+DMFT method is used at finite temperatures, but it is by construction a local method working essentially with a single site. Cluster-DMFT extensions are currently developed, but again these have their own difficulties like convergence problems which often do not allow to go down to realistic temperatures.

Summarizing, the field of strongly correlated systems stays an active field and no slow down can be seen at present. We are confident that the introduction of the LDA+VCA approach enriches this field and will allow to study systems not accessible by other methods, notably compounds where non-local correlation effects play a significant role. The introduction of the LDA+VCA approach therefore adds actively to the understanding of a number of very different systems as the number and diversity of results presented in this thesis shows.

Appendix A

Acknowledgment

I want to thank the whole institute of theoretical and computational physics of the technical university Graz for their kind support in every respect over the years; especially my supervisor Prof. E. Arrigoni for giving me regularly deep insight into interesting theoretical aspects that emerged from our work. I'm also indebted to Liviu Chioncel for his friendship and his continued introducing me to exciting methods. Both a big thank you for giving me the chance to work in this interesting field and allowing me generously to present our work at many international conferences. It was big fun all these years to work and learn in this group.

In addition, I am also grateful to Anna, Christian, Peter, Ralf, Xiancong, Khalid, Markus, Maria, Michi, both Martins, Jing, Ingrid, Franz and the whole plasma physics-group for the kind atmosphere and good discussions. I also want to thank Mik, for her consistent patience when some exciting new result kept me regularly longer at the institute. I am much obliged to my parents for making all this possible.

The cpu-power needed for the calculations presented within this thesis is extensive and I feel indebted to the institute for tolerating my at critical times liberal use of the available powerful servers. A thank you also to Andi for doing such a good job at keeping the machines up and running.

Finally, supporting the years of my PhD I am grateful for the financial support by the Austrian science fund (FWF projects P18505-N16 and P18551-N16), and by the cooperation project "NAWI Graz" (F-NW-515-GASS).

Appendix B

List of publications

- [P1] L. Chioncel, H. Allmaier, E. Arrigoni, A. Yamasaki, M. Daghofer, M.I. Katsnelson and A.I. Lichtenstein, “Half-metallic ferromagnetism and the spin polarization in CrO₂” in *Physical Review B*, Vol. 75, Issue 14, 2007, pp. 140406 (R) (available at <http://arxiv.org/abs/cond-mat/0609060>).
- [P2] H. Allmaier, L. Chioncel, E. Arrigoni, M.I. Katsnelson and A.I. Lichtenstein, “Spin polarization study of NiMnSb using the VCA” in *Journal of Optoelectronics and Advanced Materials*, Vol. 10, No 7, 2008, pp. 1671-1674.
- [P3] H. Allmaier, L. Chioncel, E. Arrigoni, E. Burzo, F. Beiușeanu, M.I. Katsnelson and A.I. Lichtenstein, “Half-metallic ferromagnetism and spin-polarization in CrO₂: a detailed VCA-study” in *Journal of Optoelectronics and Advanced Materials*, Vol. 10, No 4, 2008, pp. 737-743.
- [P4] H. Allmaier, L. Chioncel, E. Arrigoni, M.I. Katsnelson and A.I. Lichtenstein, “Electron correlation effects in the half-metallic NiMnSb within a cluster perturbation approach with ab-initio parameters” in *Iranian Journal of Physics Research*, Vol. 8, No 2, 2008, pp. 67-71.
- [P5] E. Burzo, N. Bucur, H. Allmaier and L. Chioncel, “Half-metallic ferromagnetism in light-rare earth nitrides” in *Journal of Optoelectronics and Advanced Materials*, Vol. 10, No 2, 2008, pp. 389-395.
- [P6] H. Allmaier, L. Chioncel and E. Arrigoni, “Titanium nitride: A correlated metal at the threshold of a Mott transition” in *Physical Review B*, Vol. 79, Issue 23, 2009, pp. 235126 (available at <http://arxiv.org/abs/0904.3569>).
- [P7] H. Allmaier, L. Chioncel and E. Arrigoni, M.I. Katsnelson and A.I. Lichtenstein, “Half-metallicity in NiMnSb: a Variational Cluster Approach with ab-initio parameters” in *Physical Review B*, Vol. 81, Issue 5, 2010, pp. 054422 (available at <http://arxiv.org/abs/0909.3807>).
- [P8] H. Allmaier, L. Chioncel, E. Arrigoni and collaborators, “Half-metallicity in CrAs/GaAs-heterostructures” in preparation for submission to *Physical Review B* and <http://arxiv.org/>.

Appendix C

The Löwdin-downfolding technique

In this appendix the Löwdin-downfolding technique is presented to outline the principle of downfolding and its difficulties.

Downfolding is a useful technique to calculate only a subset of eigenvalues and eigenfunctions of an eigenproblem. Following [26], the principle is sketched below.

We consider the general case

$$\bar{H}\mathbf{u} = \epsilon\mathbf{u}, \quad (\text{C.1})$$

where \mathbf{u} is the eigenvector of matrix \bar{H} corresponding to the eigenvalue ϵ .

However, the choice of the subelements of \bar{H} is in principle not limited. As an example, we may only be interested in calculating the subset \bar{H}_{oo} of eigenvalues and eigenvectors corresponding to the odd-numbered columns and rows of the full matrix \bar{H} . Consequently, we rewrite this eigenproblem

$$\begin{aligned} \bar{H}_{oo}\mathbf{u}_o + \bar{H}_{oe}\mathbf{u}_e &= \epsilon\bar{1}_{oo}\mathbf{u}_o \\ \bar{H}_{eo}\mathbf{u}_o + \bar{H}_{ee}\mathbf{u}_e &= \epsilon\bar{1}_{ee}\mathbf{u}_e, \end{aligned} \quad (\text{C.2})$$

where \bar{H}_{oo} and \bar{H}_{ee} denote the subblocks of the full matrix \bar{H} that contain only the odd or even numbered columns and rows, respectively. $\bar{1}$ represents the unit matrix.

From the expression for \bar{H}_{eo} in Eq. (C.2) we calculate

$$\begin{aligned} \bar{H}_{eo}\mathbf{u}_o &= (\epsilon\bar{1}_{ee} - \bar{H}_{ee})\mathbf{u}_e \\ \mathbf{u}_e &= (\epsilon\bar{1}_{ee} - \bar{H}_{ee})^{-1}\bar{H}_{eo}\mathbf{u}_o \end{aligned} \quad (\text{C.3})$$

and inserting the result into the expression for \bar{H}_{oo} in Eq. (C.2) gives

$$(\bar{H}_{oo} + \bar{H}_{oe}(\epsilon\bar{1}_{ee} - \bar{H}_{ee})^{-1}\bar{H}_{eo})\mathbf{u}_o = \epsilon\bar{1}_{oo}\mathbf{u}_o. \quad (\text{C.4})$$

By using Eq. (C.4) to calculate the eigenproblem for the odd-ordered elements the problem is reduced in dimension in comparison to the original problem Eq. (C.1).

The advantage of reducing the dimension comes with the complication that the left hand side of the equation depends now on the eigenvalue which is not known at the beginning.

By combining the NMTO-downfolding technique with density functional theory, the Stuttgart NMTO-band program¹ allows to downfold iteratively. By choosing ϵ by hand the chosen subset of the full band structure of the system of interest is calculated and compared to the full band structure. Generally, many iterations are needed for satisfactory agreement. However, in principle this can be done to arbitrary precision, at least for isolated bands [26].

¹The Stuttgart NMTO-band program (version 47.7) of Ole Krogh Andersen and Tanusri Saha-Dasgupta, Max-Planck-Institut für Festkörperforschung, Heisenbergstrasse 1, D-70569 Stuttgart

Appendix D

Finite size effects

As discussed in chapter 2.4, the VCA approach approximates the interactions on the lattice by the self-energy of the cluster. Consequently, the quality of the obtained results depends to a certain degree on the choice of the reference system.

In general one will choose the largest reference system that is still practical, however, for simple systems a point of diminishing returns may be reached even with a rather small number of sites within the cluster and increasing the system size further may not give sufficient additional benefit to justify the increase in numerical effort.

In addition, in chapter 3.4 the LDA+VCA calculations for TiN show a peculiar scaling behavior. For a specific cluster geometry suddenly non-local correlations appear that are not present for smaller clusters.

To show that TiN is a rare exception, it is the intention of this chapter to show the normal scaling behavior. Therefore, we investigate finite size effects for CrO₂ by choosing either four, six and eight sites as shown in Fig. D.1. This again demonstrates the need to keep the number of orbitals in the basis low as it was not possible to go beyond eight sites. For a nine site cluster an integer overflow¹ occurred that caused the process to abort.

Following chapter 3.1, the Oxygen octahedra around the Chromium-sites sitting on the face of the tetragon are rotated against those located at the *bcc*-sites. Therefore, all Chromium-sites are no longer equivalent [2] and all reference systems have to include the two different Chromium sites, Cr₁ and Cr₂.

Fig. D.1 shows the tetragonal CrO₂-lattice, where the two nonequivalents Chromium-sites are shown with different colors. Since the LDA+VCA approach becomes exact in the limit of an infinitely large reference system one expects that beyond a certain cluster size the changes in the results become negligible. This is further supported by the observation that in real compounds the hopping amplitudes between lattice sites decrease with increasing distance.

In Fig. D.2 the results from LDA+VCA are shown for the three different cluster geometries.

Overall, the results for all cluster geometries agree very well and one finds only small differences. The most notable differences for the various cluster sizes can be

¹We are using 64 Bit integers.

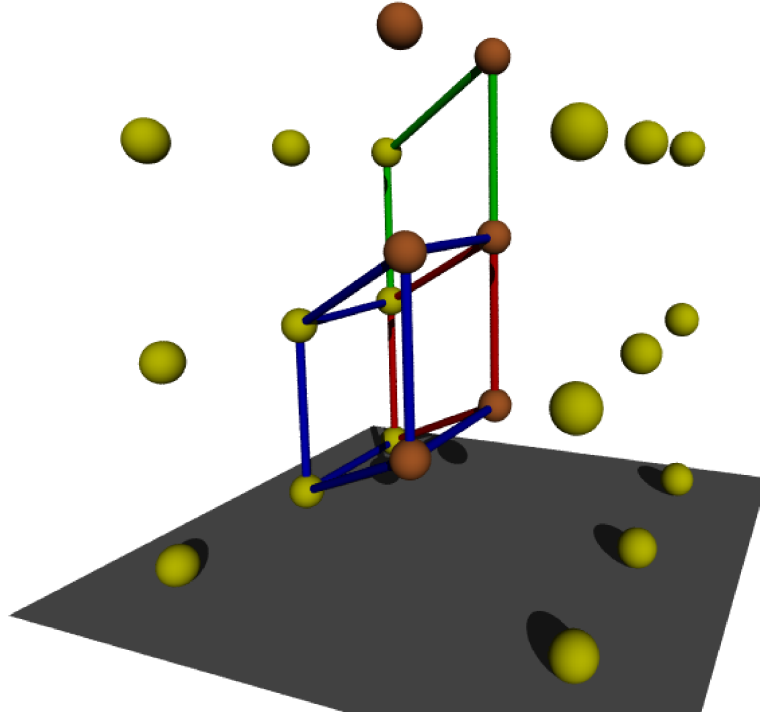


Figure D.1: The tetragonal CrO_2 -lattice showing the various cluster geometries employed as reference system: yellow and orange denote the two different Chromium-sites; the red lines denote the four sites cluster (located in the (110)-plane), extended by the green lines to six sites and doubled to eight sites by the blue lines.

seen in the minority spin channel, where the smallest cluster of four sites overestimates the peaks located at 0.3 eV and 2 eV giving however the correct position. This is not the case for the peak at 3.3eV, where the position is shifted by roughly 0.15eV relative to the larger cluster sizes. Further the shape changes as well from an double peak structure of equal height to a major peak with a shoulder (as in the eight sites case). The structure further away from the Fermi-energy, located around 5eV, is again slightly shifted, by about 0.1eV and also the shape itself is again affected: the small pseudo gap structure at 5.5eV is no longer seen in the results from the larger cluster sizes.

Since the six sites cluster is not included in the eight sites geometry, one expects to find also differences related to the inclusion of different lattice sites, which is indeed the case. Comparing the four sites result with the result from eight sites they appear

to bear closer resemblance than six to either four or eight sites; most notably the minority peak at 3.3eV deviates in position and shape significantly from the other results. The same is true but to a lesser amount for the majority peak touching the Fermi-energy where the position of the peak is slightly changed in relation to the other results.

It is important to note that all these geometries do not take into account the symmetries of the underlying lattice. As was shown for TiN, non-local correlations can arise if the cluster is chosen in agreement with the symmetry of the lattice. However, this is not always the case and also does not happen for CrO₂ as one can see in the eight sites result, Fig. 3.4, presented in chapter 3.1, where an octahedral cluster was used. The differences to the eight site cluster discussed here are negligible.

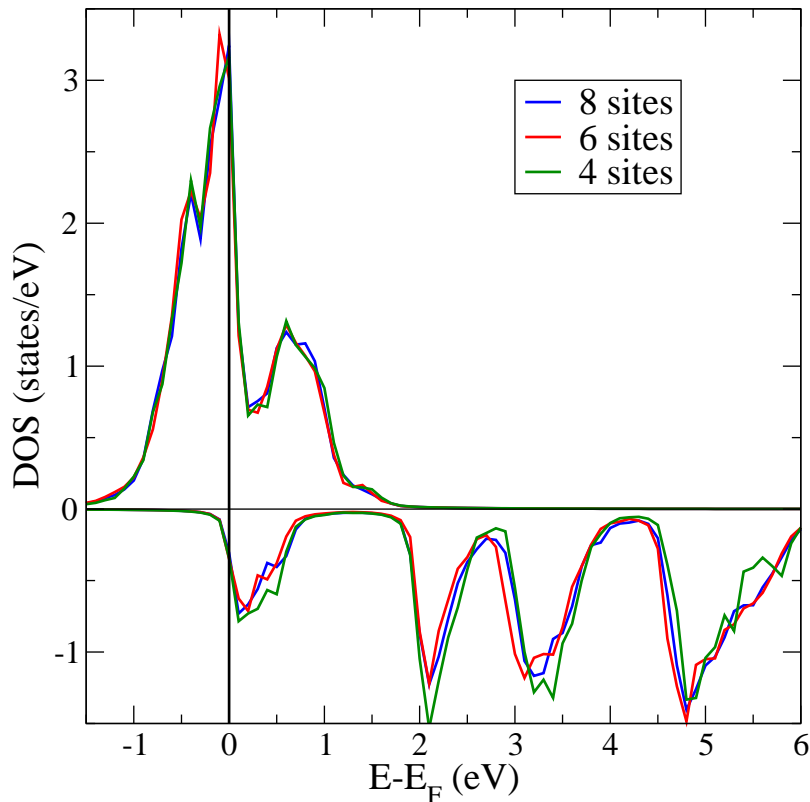


Figure D.2: Finite size effects: the most notable changes that occur by enlarging the reference system can be seen in the minority spin channel; here height and shape of the density of states is affected. In contrast to what one would expect there is more similarity between the results from the four and eight sites cluster than between the results from the six and eight sites cluster.

Appendix E

NiMnSb-results for Mn- d basis

In chapter 3.2 results for NiMnSb are presented using a rather large $Ni-d$ and $Mn-d$ basis. In a different work [2] a model Hamiltonian for NiMnSb is presented using the NMTO method where all orbitals except the $Mn-d$ orbitals are downfolded. It is argued that due to the fact that the partially filled $Mn-d$ orbitals are located energetically closest to Fermi-energy that these would solely dominate the low energy physics of NiMnSb. As a smaller NMTO-basis set would significantly reduce the required numerical effort and in addition would allow to use a larger cluster, it is tempting to follow this reasoning. We employed a LDA+VCA calculation [P2] for this $Mn-d$ basis and find that this smaller basis is not sufficient. Still, to outline why it is necessary to include $Ni-d$ in the basis as well, the results are presented in the following.

Employing a $Mn-d$ only basis set for NiMnSb brings a number of problems: considering only $Mn-d$ orbitals in the basis implicitly assumes that it is not necessary to consider correlations beyond LDA-level for the $Ni-d$ electrons although Ni is also a transition metal. While it is true that the $Ni-d$ states in NiMnSb are almost completely filled and therefore correlations do not play such a significant role as for the $Mn-d$ states, the double counting correction plays an important role as it places the few unoccupied $Ni-d$ states close to Fermi-energy.

In addition, the $Mn-d$ bands obtained from downfolding contain a significant admixture of $Ni-d$ character. Due to this admixture one has to consider additional screening effects which have to be approximated. This additional screening reduces the value of the Coulomb-interaction. It is important to consider this effect as neglecting this additional screening leads to an unrealistically large exchange splitting of the $Mn-d$ states.

E.1 Ab-initio Hamiltonian

For the single particle part of the Hamiltonian, we used the values as calculated in [2]. So for further information like the actual matrix elements or technical details

of the calculation we refer to the original work.

To investigate the correlations in NiMnSb with this *Mn-d* basis we employed a spin rotational invariant multi-orbital Hubbard-model as discussed in chapter 2.3.2. In this case it is not possible to focus onto the *Mn*(t_{2g}) states only as the *Mn-d* states are approximately half-filled.

For the Coulomb-interaction we chose intermediate values which are similar to the values chosen in chapter 3.2: $U = 3.0\text{eV}$ and $J = 0.9\text{eV}$. This in agreement with previous works that used values for U ranging from 2 to 4.8 eV[7, 53, 54, 55].

The present calculations consider only *Mn-d* orbitals in the NMTO-basis set. Due to the strong *Mn-d/Ni-d* hybridization the NMTO-wave function contains a high *Ni-d* contribution. To estimate this additional screening, we are interested in the coefficient α of the *Mn-d* character in the linear combination

$$|\chi_{total}\rangle = \alpha |\chi_{Mn}\rangle + \beta |\chi_{Ni}\rangle + \gamma |\chi_{Sb}\rangle, \quad (\text{E.1})$$

where $|\chi_{total}\rangle$ represents the total wave function obtained from the NMTO. $|\chi_{Mn}\rangle$, $|\chi_{Ni}\rangle$, $|\chi_{Sb}\rangle$ represent the corresponding pure wave functions and the coefficients α, β, γ denote the corresponding amounts of atomic character in the total wave function. In general, these coefficients are \mathbf{k} and energy dependent. In case of well separated or isolated bands, the band structure within a restricted energy window is usually dominated by a single atomic character. In the case of NiMnSb where the *Mn-d* and *Ni-d* are energetically closely located and strongly hybridized the mixing is significant, while the *Sb* admixture is negligible.

By using the so-called "fat bands" graphical presentation we estimate the coefficient α of the *Mn-d* character to about 0.4. In this presentation the graphical thickness of the band at a specific \mathbf{k} -point represents the amount of *Mn-d* character for this particular \mathbf{k} -point; we calculated an average value close to Fermi-energy. While this is only a crude approximation, it is necessary to avoid a too large artificial band splitting. Consequently, the values $U = 3.0\text{eV}$, $J = 0.9\text{eV}$ were reduced by this factor and $U = 0.75$ and $J = 0.23\text{eV}$ were used.

As reference system for the LDA+VCA calculation we employed the two *Mn*-sites shown in Fig. E.1.

We investigated to which extent the limited size of the cluster influences the results, since a significant number of hopping processes are not taken into account in the exact diagonalization. Scaling considerations show, however, that only the fine structure changes, the general shape stays unmodified to a large extent. Since the general structure of the gathered results shows considerably deficiencies, we argue that this is due to the restriction of the NMTO-basis to only *Mn-d* orbitals.

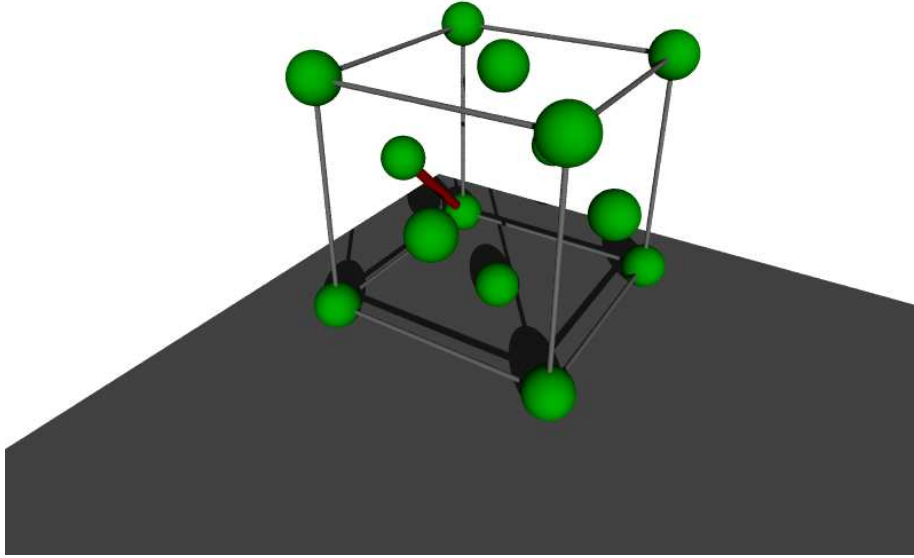


Figure E.1: Reference system used for the LDA+VCA calculation; the red line denotes the used cluster. Note that due to the downfolding procedure only the Mn -sub lattice is considered.

E.2 Results

We performed a calculation that is self consistent in the virtual chemical potential as outlined in chapter 2.4.2 and show the results in Fig. E.2.

In the following we compare the density of states obtained from the LDA+VCA approach with the results from LDA+DMFT [7], shown in Fig. E.3, and in particular to the Mn -only LDA+DMFT density of states shown in Fig. E.4. As outlined in chapter 2.2.1 on the downfolding technique, downfolding onto the $Mn-d$ manifold is only valid in a small region around Fermi-energy; consequently the results from LDA+VCA contain no structure at all outside of $[\pm 2 \text{ eV}]$.

In the majority spin channel the large peak located at about -1.5eV in the LSDA and LDA+DMFT results is shifted closer to Fermi-energy, to about -1eV . In the LDA+VCA results this peak has also considerable more spectral weight in compari-

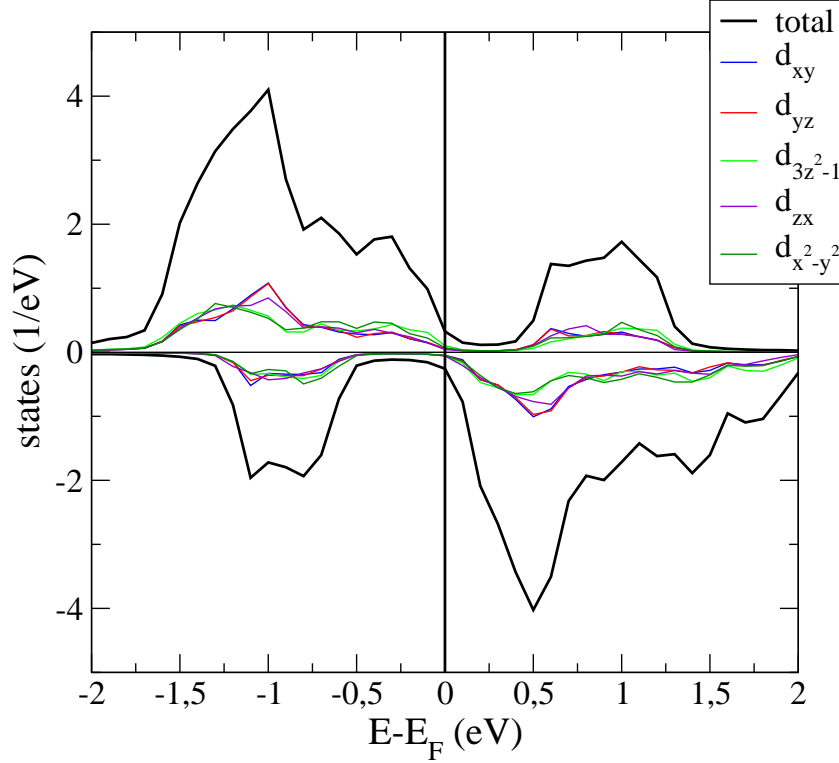


Figure E.2: LDA+VCA-results for NiMnSb using the Mn-*d* NMTO-basis set; a reduced Coulomb-interaction was used (see text): $U=0.75\text{eV}$, $J=0.9\text{eV}$.

son. While the LSDA and LDA+DMFT results show a steady decline from this peak to Fermi-energy, the results from LDA+VCA show smaller peaks below Fermi-energy and almost a gap at Fermi-energy for the majority spin channel. Above Fermi-energy the results from LDA+VCA show a peak centered at 1eV with considerable spectral weight that is not present in the LSDA and LDA+DMFT results.

In the minority spin channel the results from LDA+VCA show a peak located at -1eV that is also seen in the LSDA-results although with less spectral weight. In the results from LDA+DMFT this peak is pushed away from Fermi-energy and has less spectral weight in comparison to results from LSDA. The width of the minority spin gap in the LDA+VCA results is about 0.5eV which is a bit larger than in the results from LSDA and LDA+DMFT. Above Fermi-energy the results from LDA+VCA show the large peak that is located at 1eV in the LSDA and LDA+DMFT results is

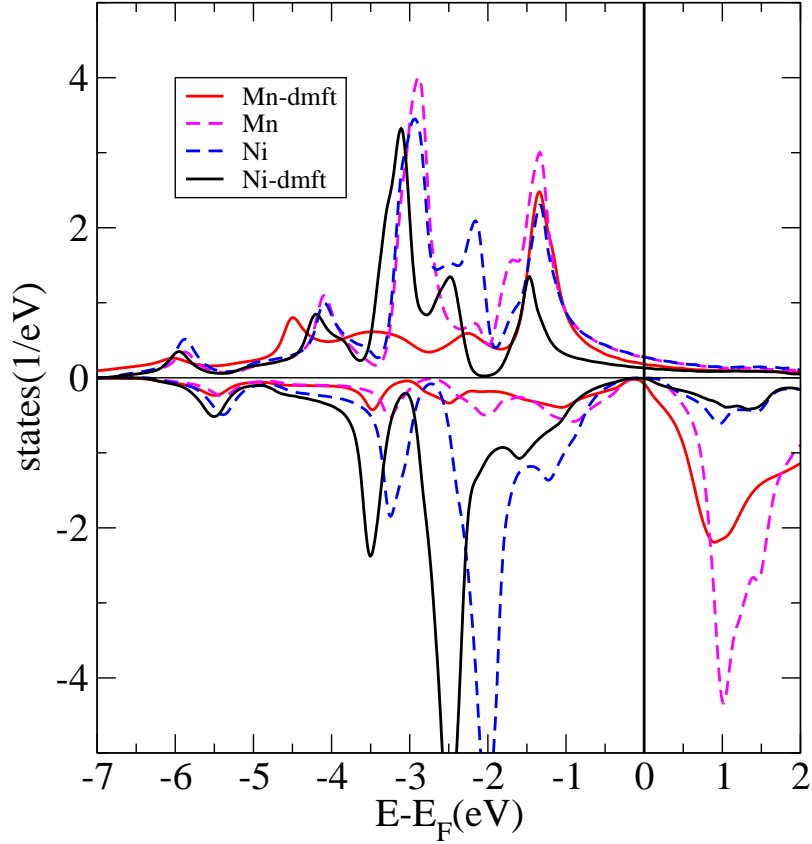


Figure E.3: Density of states for NiMnSb using Dynamical Mean field Theory (LDA+DMFT)[7]; $U= 3.0\text{eV}$, $J= 0.9\text{eV}$ were used for the *Mn-d* states. DOS obtained from LSDA is plotted for comparison.

shifted by about 0.5eV closer to Fermi-energy.

Overall, the results from LDA+VCA for this small basis would suggest that NiMnSb is a poor conductor as there is very little spectral weight at Fermi-energy. As the approximation for the value of the *Mn*-character in linear combination (E.1) also contains a certain error, there is no reason to exclude the possibility that a more sophisticated way to calculate this factor would lead consequently to larger values for the Coulomb-interaction. An increased Coulomb-interaction would enlarge the exchange splitting with the consequence that the Fermi-energy would sit in the gap for both spin-channels, predicting that NiMnSb was an insulator, which is not correct.

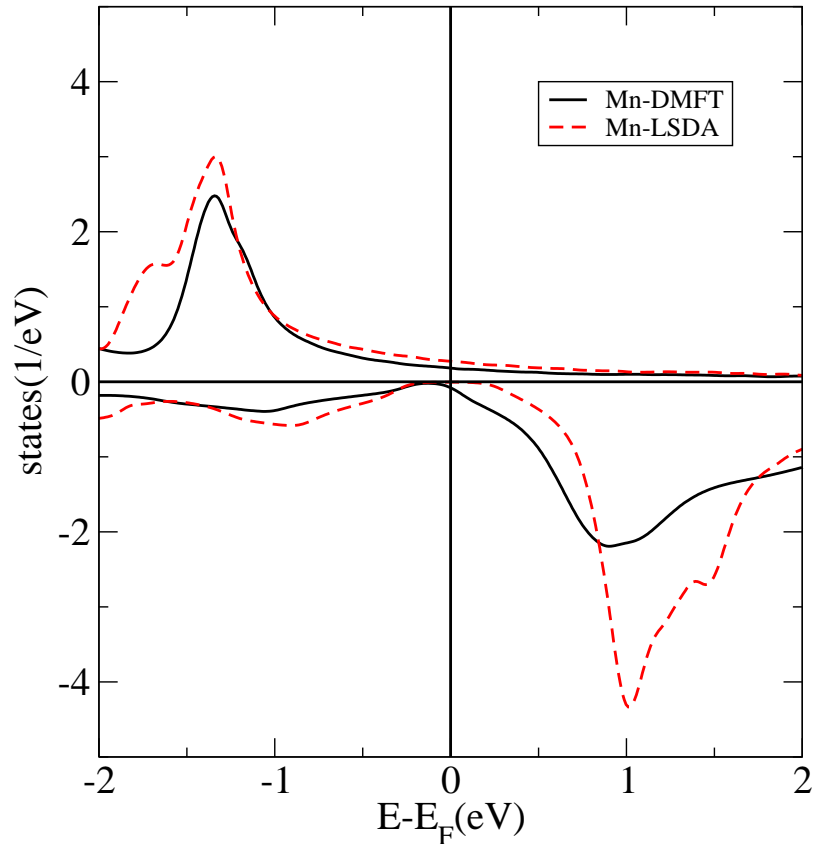


Figure E.4: *Mn* only Density of states obtained from DMFT[7]; $U = 3.0\text{eV}$, $J = 0.9\text{eV}$ were used. DOS obtained from LSDA is plotted for comparison.

E.3 Conclusion

From the results it is evident that the *Mn-d* only basis is not sufficient to describe the low energy physics around Fermi-energy for NiMnSb. In addition, the necessary approximation of the *Mn-d* character in the wave function obtained from NMTO is unsatisfactory and would need improvement. Going to a larger NMTO-basis set including the *Ni-d* states resolves this problem altogether.

As the downfolding procedure reveals that *Ni-d* states lie energetically deeper (-3eV to about -1eV), this is not so much as to have no influence on the structure at Fermi-energy. Especially as changes due to the double counting correction can bring significant changes due to the very different occupations (see also chapter 2.3.3).

Summarizing, the larger basis set is not only needed to describe the energy range close to Fermi-energy properly, but it also allows to describe a larger energy window.

As can be seen in chapter 3.2, the results for NiMnSb with the enlarged basis agree well with results from other theoretical methods as well as with experiment. The results also show that NiMnSb experiences significant non-local correlations between *Ni-d* and *Mn-d* states, which is another a posteriori reason why the results calculated using the *Mn-d* only basis are not satisfactory.

Appendix F

Different double counting schemes for NiMnSb - fully localized limit-DCC

It is instructive to investigate also an alternative form of the double counting correction as proposed by V. I. Anisimov [31, 32]; this variant of the double counting scheme is also discussed in chapter 2.3.3. It is argued that for strongly correlated systems the limit of uniform occupancy is not correct and therefore the around mean field (AMF) scheme does not apply. They give a prescription that becomes correct in the fully localized limit (FLL), where every lattice site is either fully occupied or empty.

Applied to the half-Heusler compound NiMnSb, the onsite-energies of the $Mn-d$ orbitals stay nearly unchanged as Manganese is nearly half-filled and for this particular occupation both double counting schemes, the AMF-DCC and the FLL-DCC, give identical results, see Eq. (2.38). The major correction occurs to the onsite energies of the $Ni-d$ orbitals, as the occupation of the $Ni-d$ states is far away from half-filling being almost completely filled. Therefore, the onsite-energies of the $Ni-d$ orbitals experience large changes and this causes also large changes in the corresponding density of states. We performed a LDA+VCA calculation using the same reference system and the same values for the Coulomb-interaction and Hund's rule coupling as in Chapter 3.2, the results are shown in Fig. F.1.

It is interesting to note that both DCC-schemes show non-quasiparticle states above Fermi-energy and the corresponding majority spin quasiparticle peak.

Other qualitative properties like magnetic moment and polarization stays largely unaffected and are very similar to the results employing AMF-DCC.

Comparing the density of states of the results for the FLL-DCC in Fig. F.1 and the around mean-field DCC in Fig. 3.10, one finds important qualitative differences: overall it appears that the bandwidth of majority spin density of states is reduced by as much as 1eV for the FLL-DCC scheme.

In a more detailed analysis, one finds that the FLL-DCC leads to an overestimation of the exchange splitting of the $Mn-d$ states as the unoccupied $Mn-d$ states in

the minority spin are shifted by about 1eV to higher energies causing a large gap-like region around 1eV. This is in contradiction to previous LSDA and LDA+DMFT results and also not seen in experiment. Therefore, and as the results using the FLL-DCC scheme otherwise agree quite well with the results using the around mean field DCC scheme, we disregard the results from FLL-DCC as it is clear that the FLL-DCC scheme is not suitable for this material.

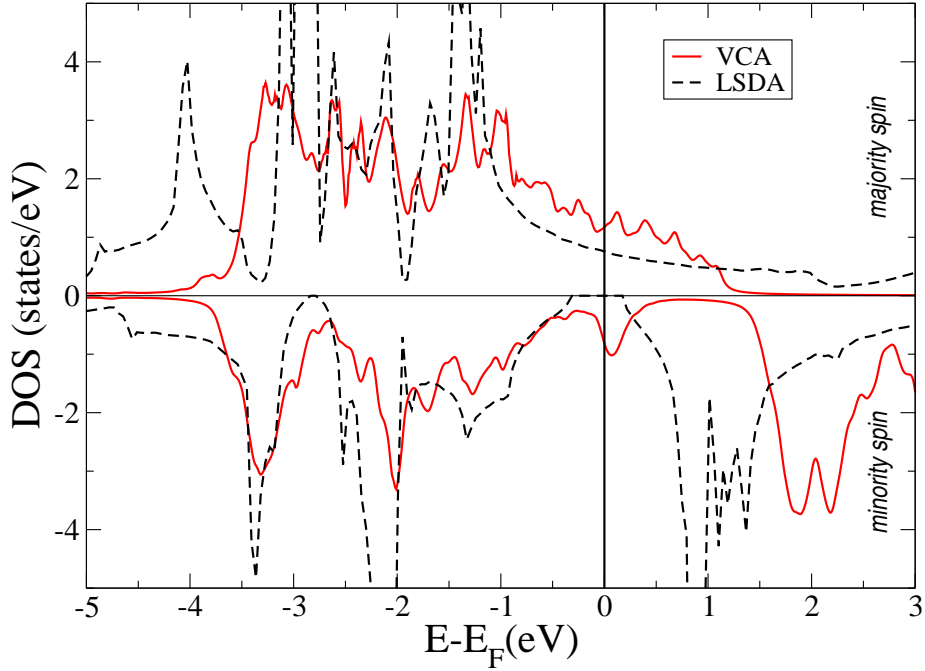


Figure F.1: Density of states for NiMnSb within LDA+VCA (using the FLL-DCC) for a Coulomb-interaction $U = 2$ and Hund's rule coupling $\bar{J} = 0.6$ (shown as red, solid line) in comparison to results obtained from LSDA (black, dashed line).

In a work by A. G. Petukhov *et al.* [32], a linear combination of the two double counting schemes is used. We studied also various combinations of the mean field-DCC and fully localized DCC, however found that the results do not improve notably and therefore do not justify the introduction of an ad-hoc parameter (in the cited work it is possible to derive the coefficients of the linear combination self-consistently).

Bibliography

- [1] K. Held, *Advances in Physics* **56**, 829 (2007).
- [2] A. Yamasaki, L. Chioncel, A. I. Lichtenstein, and O. K. Andersen, *Phys. Rev. B* **74**, 024419 (2006).
- [3] W. Zhu, B. Sinkovic, E. Vescovo, C. Tanaka, and J. S. Moodera, *Phys. Rev. B* **64**, 060403 (2001).
- [4] M. Geshi, M. Shirai, K. Kusakabe, and N. Suzuki, *Computational Materials Science* **36**, 143 (2006), *Proceedings of the Second Conference of the Asian Consortium for Computational Materials Science – ACCMS-2*.
- [5] L. Soriano, M. Abbate, H. Pen, P. Prieto, and J. M. Sanz, *Solid State Communications* **102**, 291 (1997).
- [6] A. T. Paxton, M. van Schilfgaarde, M. MacKenzie, and A. J. Craven, *J. Phys.: Condens. Matter* **12**, 729 (2000).
- [7] L. Chioncel, M. I. Katsnelson, R. A. de Groot, and A. I. Lichtenstein, *Phys. Rev. B* **68**, 144425 (2003).
- [8] S. Datta and B. Das, *Applied Physics Letters* **56**, 665 (1990).
- [9] I. Žutić, J. Fabian, and S. Das Sarma, *Rev. Mod. Phys.* **76**, 323 (2004).
- [10] P. Hohenberg and W. Kohn, *Phys. Rev.* **136B**, 864 (1964).
- [11] W. Kohn and L. Sham, *Phys. Rev.* **140A**, 1133 (1965).
- [12] L. Vitos, *Computational quantum mechanics for materials engineers - The EMTO-method and applications* (Springer-Verlag, 2007).
- [13] C. S. Wang, B. M. Klein, and H. Krakauer, *Phys. Rev. Lett.* **54**, 1852 (1985).
- [14] T. C. Leung, C. T. Chan, and B. N. Harmon, *Phys. Rev. B* **44**, 2923 (1991).
- [15] G. Kotliar *et al.*, *Rev. Mod. Phys.* **78**, 865 (2006).
- [16] L. Chioncel *et al.*, *Phys. Rev. B* **67**, 235106 (2003).

- [17] T. Saha-Dasgupta *et al.*, New Journal of Physics **9**, 380 (2007).
- [18] J. Hubbard, Proc. Roy. Soc. A **276**, 238 (1963).
- [19] J. Hubbard, Proc. Roy. Soc. A **277**, 237 (1964).
- [20] J. Hubbard, Proc. Roy. Soc. A **281**, 401 (1964).
- [21] J. Hubbard, Proc. Roy. Soc. A **285**, 542 (1964).
- [22] M. Imada, A. Fujimori, and Y. Tokura, Rev. Mod. Phys. **70**, 1039 (1998).
- [23] N. W. Ashcroft and N. D. Mermin, *Solid state physics* (Saunders College, 1976).
- [24] G. D. Mahan, *Many-particle physics* (Plenum, 2000).
- [25] O. K. Andersen and T. Saha-Dasgupta, Phys. Rev. B **62**, R16219 (2000).
- [26] E. Zurek, O. Jepsen, and O. K. Andersen, ChemPhysChem **6**, 1934 (2005).
- [27] J. S. Griffith, *The theory of transition metal ions* (Cambridge University Press, 1964).
- [28] V. I. Anisimov, F. Aryasetiawan, and A. I. Lichtenstein, Journal of Physics: Condensed Matter **9**, 767 (1997).
- [29] M. T. Czyżyk and G. A. Sawatzky, Phys. Rev. B **49**, 14211 (1994).
- [30] F. M. F. de Groot, J. C. Fuggle, B. T. Thole, and G. A. Sawatzky, Phys. Rev. B **42**, 5459 (1990).
- [31] V. I. Anisimov, I. V. Solovyev, M. A. Korotin, M. T. Czyżyk, and G. A. Sawatzky, Phys. Rev. B **48**, 16929 (1993).
- [32] A. G. Petukhov, I. I. Mazin, L. Chioncel, and A. I. Lichtenstein, Phys. Rev. B **67**, 153106 (2003).
- [33] C. Gros and R. Valenti, Phys. Rev. B **48**, 418 (1993).
- [34] M. Aichhorn, *Ordering Phenomena in Strongly-Correlated Systems: Cluster Perturbation Theory Approaches* (TU-Graz, 2004).
- [35] M. Potthoff, M. Aichhorn, and C. Dahnken, Phys. Rev. Lett. **91**, 206402 (2003).
- [36] M. Potthoff, Eur. Phys. J. B **36**, 335 (2003).

- [37] M. Aichhorn and E. Arrigoni, *Europhys. Lett.* **72**, 117 (2005).
- [38] M. Aichhorn, E. Arrigoni, M. Potthoff, and W. Hanke, *Phys. Rev. B* **74**, 024508 (2006).
- [39] T. Tsujioka *et al.*, *Phys. Rev. B* **56**, R15509 (1997).
- [40] C. B. Staggarescu *et al.*, *Phys. Rev. B* **61**, R9233 (2000).
- [41] K. Suzuki and P. M. Tedrow, *Phys. Rev. B* **58**, 11597 (1998).
- [42] E. J. Singley, C. P. Weber, D. N. Basov, A. Barry, and J. M. D. Coey, *Phys. Rev. B* **60**, 4126 (1999).
- [43] R. Yamamoto, Y. Moritomo, and A. Nakamura, *Phys. Rev. B* **61**, R5062 (2000).
- [44] E. Z. Kurmaev *et al.*, *Phys. Rev. B* **67**, 155105 (2003).
- [45] D. J. Huang *et al.*, *Phys. Rev. B* **67**, 214419 (2003).
- [46] S. P. Lewis, P. B. Allen, and T. Sasaki, *Phys. Rev. B* **55**, 10253 (1997).
- [47] M. A. Korotin, V. I. Anisimov, D. I. Khomskii, and G. A. Sawatzky, *Phys. Rev. Lett.* **80**, 4305 (1998).
- [48] I. I. Mazin, D. J. Singh, and C. Ambrosch-Draxl, *Phys. Rev. B* **59**, 411 (1999).
- [49] M. van Veenendaal and A. J. Fedro, *Phys. Rev. B* **70**, 012412 (2004).
- [50] K. Schwarz, *Journal of Physics F-Metal Physics* **16**, L211 (1986).
- [51] R. Soulen *et al.*, *Science* **282**, 85 (1998).
- [52] Y. Ji *et al.*, *Phys. Rev. Lett.* **86**, 5585 (2001).
- [53] L. Chioncel, M. I. Katsnelson, G. A. de Wijs, R. A. de Groot, and A. I. Lichtenstein, *Phys. Rev. B* **71**, 085111 (2005).
- [54] L. Chioncel, E. Arrigoni, M. I. Katsnelson, and A. I. Lichtenstein, *Phys. Rev. Lett.* **96**, 137203 (2006).
- [55] L. Chioncel *et al.*, *Phys. Rev. Lett.* **96**, 197203 (2006).
- [56] S. M. Watts, S. Wirth, S. von Molnár, A. Barry, and J. M. D. Coey, *Phys. Rev. B* **61**, 9621 (2000).
- [57] P. Schlottmann, *Phys. Rev. B* **67**, 174419 (2003).

- [58] V. I. Anisimov and O. Gunnarsson, Phys. Rev. B **43**, 7570 (1991).
- [59] M. S. Laad, L. Craco, and E. Müller-Hartmann, Phys. Rev. B **64**, 214421 (2001).
- [60] L. Craco, M. S. Laad, and E. Muller-Hartmann, Phys. Rev. Lett. **90**, 237203 (2003).
- [61] D. M. Edwards and J. A. Hertz, Journal of Physics F-Metal Physics **3**, 2191 (1973).
- [62] V. Y. Irkhin and M. I. Katsnelson, J. Phys.: Condens. Matter **2**, 7151 (1990).
- [63] A. Toropova, G. Kotliar, S. Y. Savrasov, and V. S. Oudovenko, Physical Review B (Condensed Matter and Materials Physics) **71**, 172403 (2005).
- [64] R. A. de Groot, F. M. Mueller, P. G., Engen, and K. H. J. Buschow, Phys. Rev. Lett. **50**, 2024 (1983).
- [65] K. E. H. M. Hanssen and P. E. Mijnaerends, Phys. Rev. B **34**, 5009 (1986).
- [66] K. E. H. M. Hanssen, P. E. Mijnaerends, L. P. L. M. Rabou, and K. H. J. Buschow, Phys. Rev. B **42**, 1533 (1990).
- [67] J. S. Correa, C. Eibl, G. Rangelov, J. Braun, and M. Donath, Phys. Rev. B **73**, 125316 (2006).
- [68] J. Minar, J. Braun, S. Bornemann, and M. Donath, J. Phys. D: Appl. Phys. **42**, 084009 (1999).
- [69] G. A. de Wijs and R. A. de Groot, Phys. Rev. B **64**, 020402 (2001).
- [70] J. Liu *et al.*, J. Appl. Phys. **99**, 036110 (2006).
- [71] M. I. Katsnelson, V. Y. Irkhin, L. Chioncel, A. I. Lichtenstein, and R. A. de Groot, Reviews of Modern Physics **80**, 315 (2008).
- [72] L. Chioncel *et al.*, Phys. Rev. Lett. **100**, 086402 (2008).
- [73] L. Chioncel, E. Arrigoni, M. I. Katsnelson, and A. I. Lichtenstein, Phys. Rev. B **79**, 125123 (2009).
- [74] V. Y. Irkhin and M. I. Katsnelson, Sov. Phys. - Solid State **25**, 1947 (1983).
- [75] A. I. Lichtenstein and M. I. Katsnelson, Phys. Rev. B **57**, 6884 (1998).
- [76] M. I. Katsnelson and A. I. Lichtenstein, J. Phys.: Condens. Matter **11**, 1037 (1999).

- [77] M. I. Katsnelson and A. I. Lichtenstein, *Eur. Phys. J. B* **30**, 9 (2002).
- [78] L. V. Pourovskii, M. I. Katsnelson, and A. I. Lichtenstein, *Phys. Rev. B* **72**, 115106 (2005).
- [79] S. Ögüt and K. M. Rabe, *Phys. Rev. B* **51**, 10443 (1995).
- [80] I. Galanakis, P. H. Dederichs, and N. Papanikolaou, *Phys. Rev. B* **66**, 134428 (2002).
- [81] B. R. K. Nanda and I. Dasgupta, *J. Phys.: Condens. Matter* **15**, 7307 (2003).
- [82] E. Kulatov and I. I. Mazin, *J. Phys.: Condens. Matter* **2**, 343 (1990).
- [83] C. Hordequin, J. Pierre, and R. Currat, *Physica B* **234-236**, 605 (1997).
- [84] A. Kimura *et al.*, *Phys. Rev. B* **56**, 6021 (1997).
- [85] S. K. Clowes *et al.*, *Phys. Rev. B* **69**, 214425 (2004).
- [86] D. M. Edwards, *J. Phys. C* **16**, L327 (1983).
- [87] M. I. Auslender and V. Y. Irkhin, *Z. Phys. B* **56**, 301 (1984).
- [88] V. Y. Irkhin and M. I. Katsnelson, *Phys. Rev. B* **73**, 104429 (2006).
- [89] M. Shirai, *J. Appl. Phys.* **93**, 6844 (2003).
- [90] H. Akinaga, T. Magano, and M. Shirai, *Jpn. J. Appl. Phys.* **39**, L1118 (2000).
- [91] A. Continenza, S. Picozzi, W. T. Geng, and A. J. Freeman, *Phys. Rev. B* **64**, 085204 (2001).
- [92] Y.-J. Zhao, W. T. Geng, A. J. Freeman, and B. Delley, *Phys. Rev. B* **65**, 113202 (2002).
- [93] W.-H. Xie, Y.-Q. Xu, B.-G. Liu, and D. G. Pettifor, *Phys. Rev. Lett.* **91**, 037204 (2003).
- [94] I. Galanakis and P. Mavropoulos, *Phys. Rev. B* **67**, 104417 (2003).
- [95] L. Chioncel *et al.*, *Phys. Rev. B* **75**, 140406 (2007).
- [96] M. Shirai, K. Ikeuchi, H. Taguchi, and H. Akinaga, *J. Supercond.* **16**, 27 (2003).
- [97] Y.-J. Zhao and A. Zunger, *Phys. Rev. B* **71**, 132403 (2005).
- [98] M. Mizuguchi *et al.*, **91**, 7917 (2002).

- [99] K. Nagao, M. Shirai, and Y. Miura, *J. Appl. Phys.* **95**, 6518 (2004).
- [100] H. Akinaga and M. Mizuguchi, *Journal of Physics: Condensed Matter* **16**, S5549 (2004).
- [101] A. I. Lichtenstein, M. I. Katsnelson, and G. Kotliar, *Phys. Rev. Lett.* **87**, 067205 (2001).
- [102] K. Schwarz, A. R. Williams, J. J. Cuomo, J. H. E. Harper, and H. T. G. Hentzell, *Phys. Rev. B* **32**, 8312 (1985).
- [103] V. M. Vinokur *et al.*, *Nature* **452**, 613 (2008).
- [104] L. Porte, L. Roux, and J. Hanus, *Phys. Rev. B* **28**, 3214 (1983).
- [105] L. I. Johansson, P. M. Stefan, M. L. Shek, and A. N. Christensen, *Phys. Rev. B* **22**, 1032 (1980).
- [106] V. A. Gubanov, E. Z. Kurmaev, and G. P. Shveikin, *J. Phys. Chem. Solids* **38**, 201 (1977).
- [107] F. Riehle, T. Wolf, and C. Politis, *Z. Phys. B* **47**, 3 (1982).
- [108] W. K. Schubert, R. N. Shelton, and E. L. Wolf, *Phys. Rev. B* **23**, 5097 (1981).
- [109] W. K. Schubert, R. N. Shelton, and E. L. Wolf, *Phys. Rev. B* **24**, 6278 (1981).
- [110] D. W. Lynch, C. G. Olson, D. J. Peterman, and J. H. Weaver, *Phys. Rev. B* **22**, 3991 (1980).
- [111] J. F. Alward, C. Y. Fong, M. El-Batanouny, and F. Wooten, *Phys. Rev. B* **12**, 1105 (1975).
- [112] A. Neckel, *International Journal of Quantum Chemistry* **13**, 1317 (1983).
- [113] P. Marksteiner, P. Weinberger, A. Neckel, R. Zeller, and P. H. Dederichs, *Phys. Rev. B* **33**, 812 (1986).
- [114] D. A. Papaconstantopoulos, W. E. Pickett, B. M. Klein, and L. L. Boyer, *Phys. Rev. B* **31**, 752 (1985).
- [115] V. P. Zhukov, V. A. Gubanov, O. Jepsen, N. E. Christensen, and O. K. Andersen, *J. Phys. Chem. Solids* **49**, 841 (1988).
- [116] S.-H. Jhi, S. G. Louie, M. L. Cohen, and J. Ihm, *Phys. Rev. Lett.* **86**, 3348 (2001).
- [117] O. K. Andersen and O. Jepsen, *Phys. Rev. Lett.* **53**, 2571 (1984).

- [118] V. I. Anisimov, J. Zaanen, and O. K. Andersen, *Phys. Rev. B* **44**, 943 (1991).
- [119] F. Aryasetiawan, K. Karlsson, O. Jepsen, and U. Schönberger, *Phys. Rev. B* **74**, 125106 (2006).
- [120] E. Pavarini, A. Yamasaki, J. Nuss, and O. K. Andersen, *New J. Phys.* **7**, 188 (2005).
- [121] F. Aryasetiawan *et al.*, *Phys. Rev. B* **70**, 195104 (2004).
- [122] M. Tsujimoto *et al.*, *Journal of Electron Spectroscopy and Related Phenomena* **143**, 161 (2005).
- [123] P. S. Herle, M. S. Hegde, N. Y. Vasathacharyan, and S. Philip, *J. Solid. Stat. Chem.* **134**, 120 (1997).
- [124] P. Herzig, J. Redinger, R. Eibler, and A. Neckel, *J. Solid. Stat. Chem.* **70**, 281 (1987).
- [125] Z. Dridi, B. Bouhafs, P. Ruterana, and H. Aourag, *J. Phys.: Condens. Matter* **14**, 10237 (2002).
- [126] J. Redinger, P. Marksteiner, and P. Weinberger, *Z. Phys. B* **63**, 321 (1986).
- [127] V. P. Zhukov, V. A. Gubanov, O. Jepsen, N. E. Christensen, and O. K. Andersen, *Philos. Mag. B* **58**, 139 (1988).
- [128] C. G. H. Walker, J. A. D. Matthew, C. A. Anderson, and N. M. D. Brown, *Surf. Sci.* **412/413**, 405 (1998).